

THESE DE DOCTORAT DE

L'UNIVERSITE DE RENNES 1
COMUE UNIVERSITE BRETAGNE LOIRE

ECOLE DOCTORALE N°601
*Mathématiques et Sciences et Technologies
de l'Information et de la Communication*
Spécialité : ELECTRONIQUE

Par

Fatima GARCIA CASTRO

Deformation microsensors on flexible substrate for health applications

Thèse présentée et soutenue à RENNES, le 12 décembre 2019
Unité de recherche : Institut d'Electronique et Télécommunications de Rennes (IETR)

Rapporteurs avant soutenance :

Gaël GAUTIER Professeur, GREMAN, Université de Tours
Claudine GEHIN Maître de conférences HDR, INL, INSA de Lyon

Composition du Jury :

Président :

Examineurs : Nathalie COULON	Ingénieur de recherche CNRS, IETR, Université de Rennes1
Henri HAPPY	Professeur, IEMN, Université de Lille
Claude SIMON	Maître de conférences, IETR, Université de Rennes1

Dir. de thèse : France LE BIHAN

Professeur, IETR, Université de Rennes1

Membre invité : Olivier DE SAGAZAN

Ingénieur de recherche, IETR, Université de Rennes1

Acknowledgements

I am using this opportunity to express my gratitude to everyone who supported me throughout this PhD project.

First, I would like to thank my supervisor Professor F. Le Bihan, and my co-supervisors N. Coulon and C. Simon who provided me an opportunity to join their team, and who gave access to the laboratory and research facilities.

I would also like to express my real gratitude to O. De Sagazan, who has always endeavoured to help me, train me and answer my scientific questions. This thesis is result of his generous attitude, continuous support, patience, motivation and immense knowledge.

I also thank my lab partners especially the “Sushi Team” for their support, for making the hours of the day easier and for all the good moments that we have had in the last three years.

Thanks also to my “merienda” colleagues, Rosita and Laura, for the funny moments, for being such a good listener and being there when I needed your help.

Last but not least, I wish to thank to my close friends in Rennes, Alejandra, Jessica, Arnaud, Arturo, Carlos, Fran and especially Alba, Claudia and Gustavo who, without expecting anything in return, have always been by my side in good times and bad times to support me and make me laugh.

Finally, I would like to thank my family: my parents and my brother Jose Angel, for the love and unconditional support they always give me every day.

Table of contents

General introduction	5
 CHAPTER 1. Flexible electronics: applications and technologies of pressure sensors	9
1. Introduction.....	10
2. Pressure sensor: principle and classification	10
2.1 Classification according to the detection range	10
2.2 Parameters for pressure sensor characterization	12
2.3 Transduction mechanisms and applications	13
2.3.1 Piezoresistivity	13
2.3.2 Piezoelectric effect.....	15
2.3.3 Capacitance	16
2.3.4 Other transduction methods	17
3. Techniques to perform flexible devices.....	18
3.1 Top-down fabrication	18
3.2 Bottom-up fabrication	20
4. Substrates	21
5. Semiconductor and dielectric materials.....	25
5.1 Organic semiconductor in flexible electronics	25
5.2 Inorganic semiconductor flexible electronics	26
6. Metal electrodes	28
7. Conclusion	30
8. References.....	31
 CHAPTER 2 - N-type μC-Si investigated as a pressure sensor	38
1. Introduction.....	39
2. Deposition techniques of μ c-Si at low temperature	39
2.1 Description of deposition system with PECVD reactor	40
2.2 Description of deposition system with ICP-CVD reactor	41

3.	Flexible devices with microcrystalline silicon	43
4.	Piezoresistive properties of N type $\mu\text{c-Si}$	45
5.	Mechanical behavior of thin films	47
6.	Fabrication technology on thin film flexible devices	51
6.1	Source of stress in thin film	52
6.1.1	Thermal stress	52
6.1.2	Intrinsic or growth stress	53
6.1.3	Epitaxial stress	53
6.1.4	Mechanical stress	54
6.2	Process and technological problems	55
6.3	Approaches to reduce stress related problems	56
6.4	Solutions for mechanical stresses introduced during fabrication	57
6.4.1	Effect of SiN_x encapsulating layers	57
6.4.2	Effect of reducing the area of $\mu\text{c-Si}$ deposition	60
6.4.3	Dimensional stability of Kapton® and shrinking	61
7.	Conclusion	62
8.	References	63

CHAPTER 3 - Transmission Line Measurements (TLM) and static deformations

1.	Introduction	67
2.	Transmission Line measurement (TLM)	67
2.1	Parameters extraction	68
2.2	The specific contact resistivity	70
3.	Mask design and fabrication process	72
4.	TLM Device Manufacturing Process	72
5.	Raman spectroscopy	74
6.	Results obtained with TLM technology	75
6.1	TLM parameters for N-type $\mu\text{c-Si}$ deposited by PECVD technique	76
6.2	TLM parameters for N-type $\mu\text{c-Si}$ deposited by ICP-CVD technique	80
7.	Study of the sensitivity of $\mu\text{c-Si}$ under different strain	85
7.1	Strain calculation	85

7.2	Strain calculation for our structures	88
8.	Sensitivity for N- type $\mu\text{c-Si}$ deposition by PECVD.....	89
9.	Sensitivity for N-type $\mu\text{c-Si}$ deposition by ICP-CVD.....	90
9.1	Doping gas: AsH_3 or PH_3	91
9.1.1	Deposition with constant RF and LF power:	91
9.1.2	Influence on deposition with Pulse in RF power.....	93
9.1.3	Effect of doping flow rate with pulse in RF power	94
9.2	Investigation PH_3 as doping gas.....	96
9.2.1	Constant RF: 0 W and 40 W	96
9.2.2	Effect of LF or RF power.....	97
9.2.3	Flow rate in PH_3 with RF: 0 W.....	98
10.	Conclusion.....	99
11.	References	102

CHAPTER 4 - Piezoresistive response of N-type $\mu\text{c-Si}$ under dynamic deformations 105

1.	Introduction	106
2.	Characterization system	107
3.	Data acquisition system	110
4.	Deformation measurement: electronic and signal processing	112
5.	Problems and limitation of acquisition system.....	114
5.1	Electrical noise	114
5.2	Increase ADC resolution since 10 to 32 bits.....	116
6.	Sensor design to perform dynamic measures	116
6.1	Design electrodes configuration.....	120
6.2	Geometry selection and dimensions.....	123
7.	Design dedicated to detect weak dynamic signal	128
7.1	Mask shapes design	129
7.2	Loading-offloading cycles test.....	136
7.3	Mechanical behaviour of square structure- life cycle.	138
8.	Matrix characterization	139
8.1	Design and objective	139

8.2	Matrix amplitude response to dynamic pulse	141
8.2	Matrix reaction to a complex waveform such as ECG signal	142
8.3	Matrix reliability	144
9.	Conclusion.....	145
10.	Annex.....	146
a)	Figure 4.30 Rosette shape- waveforms obtain with conditions Table 4.3	146
b)	Figure 4.32 U-shape- waveforms obtain with conditions Table 4.3.....	147
c)	Figure 4.34 Serpentine shape- waveforms obtain with conditions Table 4.3	148
d)	Figure 4.36 Three serpentine shape in parallel- waveforms obtain with conditions Table 4.3	149
e)	Figure 4.38 Five resistances in parallel - waveforms obtain with conditions Table 4.3...	150
f)	Figure 4.39 Square shape resistance - waveforms obtain with conditions Table 4.3	151
g)	Figure 4.45 Mapping waveform of the matrix	153
11.	References	154
General conclusion and perspective.....		155

General introduction

The new requirements of society have stimulated the electronics market, especially that of flexible electronics. This technology changes the way to use electronics, because it offers the possibility of having devices that can adapt to different types of surfaces, to be bent, contorted or stretched while keeping good functioning. This makes them especially useful in different sectors such as automotive, biosensors, healthcare, mobile devices or wearable technology and increases customers' interest.

Despite being widely researched, these devices still have some limitations and their technology needs to be further improved. First of all, polymers are ideal as flexible substrates because of their properties such as lightness, low cost, flexibility, extensibility and conformability to uneven surfaces. But the development of electronic devices or sensors on polymer films requires a compatible manufacturing process that respects the chemical and thermal properties of the substrates while allowing economical manufacturing on large surfaces. The temperature range for its fabrication depends on the nature of the flexible substrate. Moreover, the rigidity of traditional semiconductor materials is a limitation to their fabrication. This fact forces the industry to find alternatives to try to compensate for those weaknesses in their manufacturing process.

New research focuses on different areas to try to improve flexibility and extensibility, such as research and synthesis of new materials such as carbon nanotubes (CNTs) or graphene, which have interesting properties, especially for sensors and flexible devices, or by reducing the thickness of traditional semiconductors, or even by seeking a specific design that promotes their mechanical behavior. Moreover, flexible electronics can be fabricated using two different approaches top-down or bottom-up fabrication.

This thesis work is realized in the Microelectronics and Microsensors Department of the Institute of Electronics and Telecommunications of Rennes (IETR) and its main goal is to investigate the piezoresistive properties of microcrystalline silicon ($\mu\text{c-Si}$) deposited by two different techniques (PECVD and ICP-CVD). This material is then used to fabricate a sensor able to react to dynamic deformations.

The technology used to perform the devices is based on the piezoresistive effect and the sensors are fabricated directly on the flexible substrate. Despite the fact that the substrate chosen is Kapton® and can support a relative high-temperature process, around 400°C, during our

fabrication process we did not use temperatures higher than 180 °C. This corresponds to the annealing step, used to improve the junction between metal-semiconductor and enhance the electrical conductivity. Microcrystalline silicon is deposited at low temperature, 165 °C. The reason we choose this material is that it was widely used and investigated in the laboratory, especially for applications in TFT devices. Moreover, it was also used in some works to perform static deformations on thicker plastic substrates. Hence the innovation of this thesis which uses $\mu\text{c-Si}$ in sensor devices is to detect weak dynamic deformations; and to increase their flexibility, as the thickness of the substrate used being extremely low.

The most relevant theoretical aspects, processes, problems and results obtained throughout this thesis are presented. This manuscript is structured in four chapters.

The first chapter presents a general overview of the state of the art of pressure sensors. A classification of these sensors in the function of the detection range is presented. Characterization parameters and applications are also described. The basic working principle and the most popular transduction mechanisms, which are piezoresistivity, piezoelectric or capacitive effects, are described. This chapter also contains the explanation of the fabrication technology for flexible electronics with both top-down and bottom-up approaches, with a comparison between the two technologies and their main advantages and disadvantages. Finally, this chapter describes the different materials used in flexible electronics fabrication, from the substrate to the electrodes.

The choice of the appropriate substrate is one of the most important factors that will have an impact the degree of flexibility of the structure. It is also one of the main limitations in the fabrication, as it will determine the maximum temperature process. Different flexible substrates such as metal foil, flexible thin glass or plastic substrate are presented and discussed. Then a short description of structural semiconductor material and dielectric materials is done, with a particular emphasis on the synthesis and study of silicon. The last point of this chapter is devoted to the metal electrodes, their shape and dimension, as this can influence the mechanical behavior of the sensor.

The second chapter is dedicated to the investigation of N-type $\mu\text{C-Si}$ in pressure sensors. The deposition techniques used throughout this thesis, namely PECVD (Plasma Enhanced Chemical Vapor Deposition) and ICP-CVD (Inductively-Coupled-Plasma Chemical Vapor Deposition), are

described here. The chapter presents its main characteristics as well as their operating principles, their advantages and disadvantages. Moreover, the previous works realized in the laboratory with $\mu\text{c-Si}$ on flexible substrates and the main piezoresistive properties of this material are reviewed.

During the fabrication of our devices, the thin thickness of the substrate used caused many problems. In an attempt to find a solution and better understand the mechanical behavior of thin films, some concepts are introduced to describe them. Thin-film flexible devices technology fabrication is complicated not only by factors such as temperature limitation of the substrate, but also by other problems such as the sources of stress during film deposition. The mechanical behavior of substrate/film will depend on the Young's modulus and thickness of the substrate. The low thickness of our substrate has created some stress problems that induce cracks and affect the performance of the devices after $\mu\text{c-Si}$ deposition. To reduce them, different approaches were investigated, and used all along the fabrication process developed during this thesis.

In Chapter 3 the method of Transmission Line Measurements (TLM) for $\mu\text{c-Si}$ deposited by PECVD and ICP-CVD techniques is studied. This chapter can be divided in two sections. In the first section, we describe the mask used for TLM devices and the theory of this method with the interesting parameters that can be extracted. In the second section, this mask is used to study the uniformity of the deposition, and the sensitivity of $\mu\text{c-Si}$ to different strain deformations.

Chapter 4 presents the study of the mechanical behavior of $\mu\text{c-Si}$ when it is submitted to dynamic deformations. Here we describe the steps followed to create our own home-made characterization system, and we investigate the effect of the design and geometry on the sensor performance. To do that, two different masks are elaborated and the devices are submitted to different test such as continuous loading - offloading cycles.

At the end of the manuscript, the general conclusion highlights the main results of this thesis and presents some perspectives.

CHAPTER 1. Flexible electronics: applications and technologies of pressure sensors

1. Introduction

Flexible electronics applications appeared around the 1950s. One of the first application concerns the solar cell research. The objective was to work on the thickness of the silicon cell, which was considerably reduced until the point of being flexible. The flexible electronics field was born. Its development and applications have then grown up over until nowadays. This technology changes the way we use electronics through its ability to be bent, stretched or rolled up or be conformably shaped without working failure. For this reason, this flexible technology is a good candidate for several applications in many fields such as automotive, biosensors, healthcare, mobile devices or wearable technology.

In general, flexible materials need to present some advantages, compared to the rigid electronic technology, such as good bendability, twisting and stretchable properties, while keeping their performance and characteristics, as light-weighting and easy portability. However, some limitations exist in the manufacturing processes and materials. Research is dedicated to the synthesis of new materials, or to specific design issues that contributes to their flexibility and stretchability.

This chapter presents first a general overview of the pressure sensors, describing their working principle, parameters and their different applications according to their range of detection. It is then focused on the different techniques used to fabricate such devices.

2. Pressure sensor: principle and classification

A sensor is a device that is able to transform a physical or chemical stimulus into an electrical signal that can be read by an instrument. There are many types of sensors that detect different parameters such as distance, acceleration, displacement, pressure, force, humidity, movement, pH, etc. However, this section focuses on pressure sensor devices. We briefly introduce their classification, the transduction mechanism, the most relevant parameters, and some applications.

2.1 Classification according to the detection range

When a sensor needs to be selected, one of the first considerations to be taken into account is the detection range. This is the working range in which the sensor is able to detect the pressure

and transform it. Based on this requirement, pressure sensors can be classified into different categories, as shown in Figure 1.1.

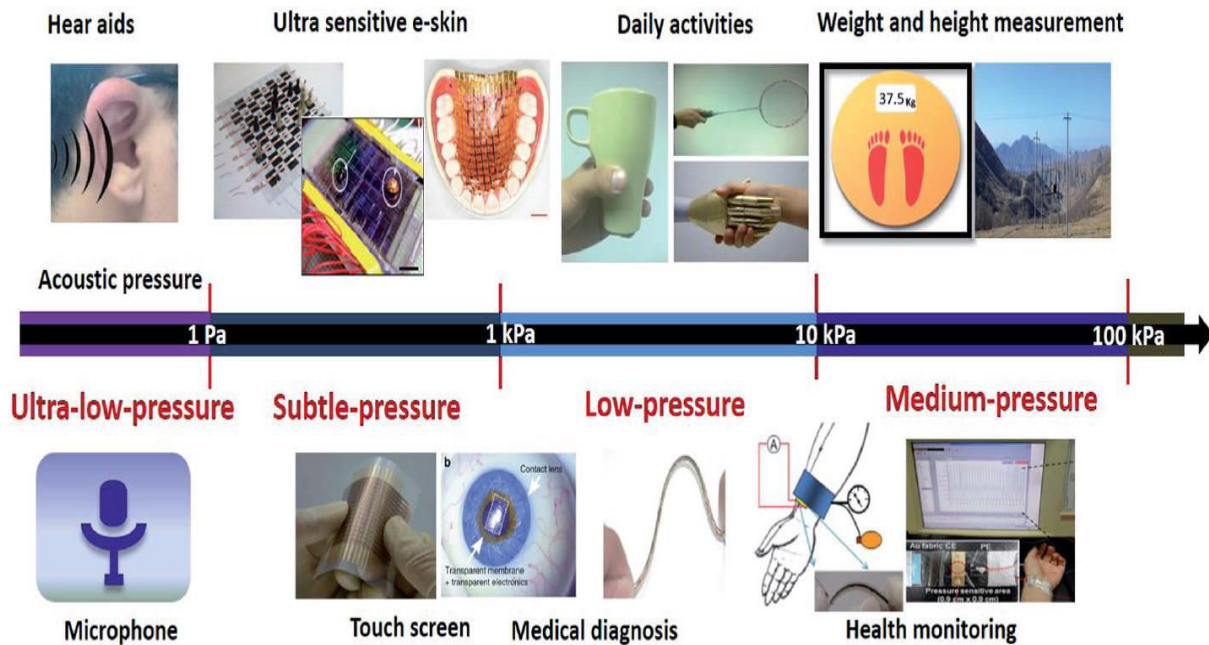


Figure 1.1. Pressure sensor classification according to the detection range and related applications [1].

Ultra-low pressures:

For a pressure range below 1 Pa, typically, the sensors are dedicated to sound pressure applications or other kinds of activities for which signals are weak and difficult to perceive, i.e. as microphones or hearing aids. This sensor is able to detect pressure less than 0.1 Pa [2].

Subtle pressure:

For 1 Pa to 1 kPa, sensors are used to develop high sensitive applications such as e-skin [3] or touchscreen devices for mobiles or tablets [4], [5] and for optical applications [6].

Low-pressure:

The pressure range between 1 to 10 kPa is widely investigated especially for applications used to grasps or touch objects [7], [8]. There is also extensive research for medical diagnosis [9] or wireless or wearable epidermal sensor [10], [11].

Medium-pressure range:

Sensors in the 10 to 100 kPa range focus especially on the development of wearable systems to measure blood pressure, pulse monitor applications [12] or active-matrix based on piezoelectric effect [13].

2.2 Parameters for pressure sensor characterization

Once the detection range of the sensor is selected, some parameters need to be considered to evaluate the performance and the accuracy of a detection device.

Limit of detection (LOD) or threshold pressure:

This parameter corresponds to the lowest pressure that produce a distinguishable change of the signal. This is a relevant parameter to determine the working limits of the sensor and it helps to classify it into the different regimes shown on Figure 1.1.

Linearity:

This parameter expresses if the output signal can be graphically represented as an approximate straight line. This is important to obtain more accurate and reliable sensors. Moreover, signals with good linearity will be easy for post-treatment. Generally, strain sensors based on the piezoresistive effect exhibit good linearity when they are submitted to low strain. However, for high levels of deformation, the response is not always linear due to significant change in morphology during stretching which can generate cracks in the structure [11], [14].

Response time, recovery time and hysteresis:

These characteristics are defined together because there is a relationship between them and both are relevant for dynamic and real-time applications.

Hysteresis can be defined as the ability of the sensor to obtain the same output signal when, under the same conditions, it is submitted to the loading-unloading cycle.

The recovery time is defined as the time that the sensor needs to come back to its electrical characteristics when the load is removed.

The response time shows the time the sensor needs to respond to the next input step. All these characteristics have a relationship with the viscoelastic property of the active material and the contact conditions between the material and the electrodes [15].

Sensitivity or Gauge factor:

During the characterization of our devices, this is one of the parameters that will be mainly explored. It is discussed in more details in Chapter 3. But we can summarize in a few words that the gauge factor is the slope of the relative change of a resistance or a capacitance versus the deformation stress applied.

2.3 Transduction mechanisms and applications

A pressure sensor is based on different physical mechanisms that can convert the physical deformation or stimulus into an electrical signal. The most commonly used effects are piezoresistivity, capacitance changes, and piezoelectricity. Each different mechanism is presented below and its main principle is described.

2.3.1 Piezoresistivity

This method is based on the variation of the electrical resistance of a semiconductor or a metal when a mechanical strain is applied. Sensors based on this phenomenon have been widely studied. They usually have a simple structure and working principle and are suitable to be used in a large range of pressures or deformations.

The effect can be explained with the following equations. First of all, the resistance is expressed by the equation 1.1:

$$R = \rho \frac{L}{S} \quad (1.1)$$

With (ρ) the resistivity of the material, (L) the length and (S) the section of the resistance. As shown in Figure 1.2, when a strain is applied a variation in the structure is produced and consequently, a change in the resistance.

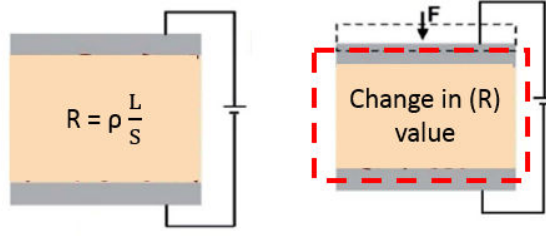


Figure 1.2. Schematic of piezoresistive effect [1].

The gauge factor (GF), defined in equation (1.2), is used to express the sensibility of the material to the deformation ϵ . All the theoretical aspects of this effect will be explained deeper in Chapter 2 and the electrical measurements in Chapter 3. The gauge factor is expressed as follows:

$$GF = \frac{\frac{\Delta R}{R}}{\epsilon} \quad (1.2)$$

The first gauges used to measure the pressure were made of a metal foil on a flexible substrate. The pressure induces strain and a change in the resistance value is observed. This change depends on the metal line geometry. The typical gauge factor obtained for the metal foil vary between 2 and 5 [16]. However, due to this quite low value of the gauge factor, research has begun on materials with higher values. In 1960, the first high performance silicon devices appeared. The devices, fabricated with n-doped silicon, present a GF near 135, and reach 170 if silicon is p type [16]. The theory of how doping silicon affects the gauge factor will be explained in Chapter 2.

Due to their simple structure and low cost, there are several examples in the literature of applications using this principle. One example is presented by R. Ramalingame [17]. A highly flexible matrix based on a carbon nanotube (CNT) polymer composite is processed on a Kapton® substrate and bound to an acquisition system. Haniff [18] proposed a flexible pressure sensor also based on piezoresistive effect made with graphene deposited through hot filament thermal chemical vapour deposition (HFT-CVD) at different temperatures.

In the piezoresistive effect, the change occurs only in the electrical resistance, while the variation of the electrical potential is due to the piezoelectric effect, described below.

2.3.2 Piezoelectric effect

It refers to the electrical change produced in materials, particularly in crystals or ceramics that do not have center of symmetry. When these materials are submitted to mechanical stress, electric polarization occurs on their volume and, as shown in Figure 1.3, electrical charges and a difference of potential appear.

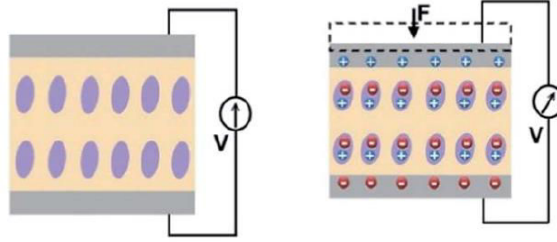


Figure 1.3. Schematic of piezoelectric effect [1].

This kind of sensor is widely used in dynamic applications, especially because it shows good performances as high sensitivity, fast response time, easy electrical signal acquisition, easy material preparation, and low power consumption or even self-power [19], [20]. In the past, traditional piezoelectric materials were ceramics and quartz. But nowadays they have been replaced by new materials, more robust, such as poly-vinylidene fluoride-trifluoroethylene P(VDF-TrFE) or zinc oxide (ZnO). Between all amount polymer and copolymer, the most popular is P(VDF-TrFE) due to simple manufacturing and high piezoelectric coefficient.

Chunyan [21] has developed a tactile sensor using dome and bump shapes of P(VDF-TrFE) films over a polymer substrate by a mold transfer method using standard MEMS techniques. The use of a new fabrication method provides a way to pattern the polymer with different shapes (dome and bump) and dimensions. The sensor developed in this paper can be used in minimally invasive biomedical devices.

C. Chang [22] has also developed devices with this piezoelectric material that provide a high-performance and a fast response for wearable applications. To do that, using the electro spinning method, P(VDF-TrFE) nanofibers are directly written on a grounded substrate as shown in Figure 1.4. Under mechanical stretching, it shows repeatable and consistent electrical outputs with efficient energy conversion.

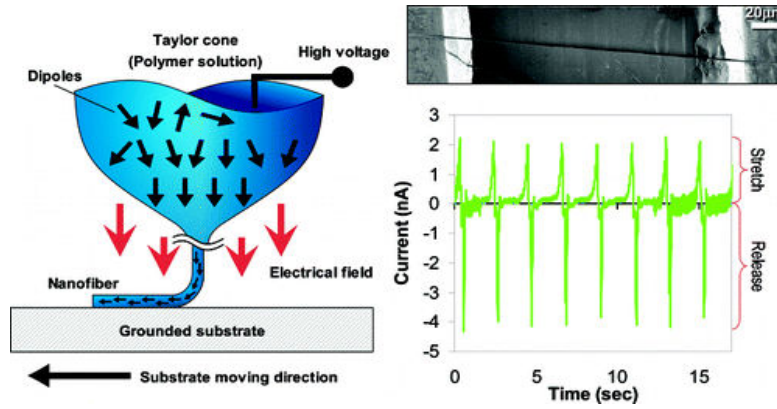


Figure 1.4. P(VDF-TrFE) nanofibers deposited by electroshock and output characteristics under stretch and release [22].

2.3.3 Capacitance

Capacitance devices can be formed by two metallic electrodes around a dielectric material. The capacitance value (C) is given by the equation (1.3) where (ϵ_0) and (ϵ_r) are the vacuum permittivity and the relative static permittivity of the material between the electrodes, A is the surface between the electrodes and (d), the distance between them. The value of the capacitance is inversely proportional to the distance between the electrodes and proportional to the dielectric contact and the area.

$$C = \frac{\epsilon_0 \epsilon_r A}{d} \quad (1.3)$$

As shown in Figure 1.5, when a deformation is applied, the distance between the two electrodes (d) and the area (A) are modified. So the value of the capacitance changes.

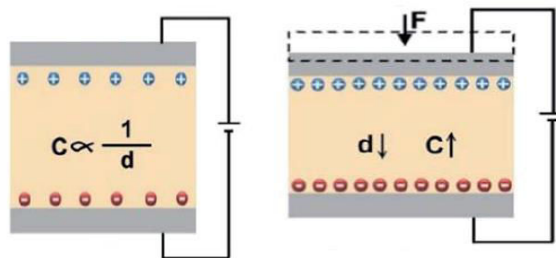


Figure 1.5. Schematic of capacitive effect [1].

There are several fields where this technology is commonly used, for example in the robotic market where, in 1997, a fingerprint array was proposed with sensitive capacitive cells on silicon. However, this sensor presents a low resolution and could only measure the normal force [23]. Later, technological improvements were achieved with capacitive sensors over polymer. These are able to measure normal and shear forces [24]. High sensitive capacitance sensors able to analyze the direction and value of three dimensional (3D) forces are mentioned by Huang [25], Dobrzynska [26] or Surapaneni [27].

2.3.4 Other transduction methods

Other methods exist for pressure sensor applications, but are not so widely used. This is the case of the optical methods, based on the measurement of the light intensity variation. They can be used for touch screen applications like smartphones or tablets. The inductive effect is another transduction method that measures the variation of an inductance between two magnetic fields or resonant sensors generally dedicated to acoustic applications.

Table 1.1 sums up the advantages and disadvantages of the three main transduction methods.

Type	Advantage	Disadvantage
Piezoresistive	Low cost Good sensitivity Low noise Simple electronics	Stiff and frail Nonlinear response Hysteresis Temperature sensitive Signal drift
Capacitive	Sensitive Low cost Availability commercial A/D chips	Cross-talk Hysteresis Complex electronics
Piezoelectric	Dynamic response High bandwidth	Temperature sensitive Not so robust electrical connection

Table 1.1. Comparative of transduction methods for pressure sensor [28].

3. Techniques to perform flexible devices

The continuous evolution and improvement of thin-film materials and devices have impulse the development of flexible electronics. Their fabrication is one of the great challenges of this technology, and their manufacturing processes have been deeply studied [29], [30] leading to a wide variety of applications in different fields such as displays, storage devices, or wearable devices for the medical area.

Despite the growing research on flexible electronics, this technique needs to be improved to present good electrical and mechanical properties. Because the results are lower than those obtained with traditional electronics made of rigid and flat semiconductor wafers.

Currently, the electronic structure of flexible devices is formed by a substrate, a semiconductor material and the electrodes. It should presents good performances after bending, stretching, twisting or deformation into complex shapes. The entire structure should be created with a compromise between the design, the thickness of the materials and their mechanical properties. One of the main drawbacks during flexible devices fabrication is that the required substrates present a temperature limitation that involves the industrial development of new methods of processing. Nowadays, there are mainly two different strategies to fabricate devices on a plastic substrate, as further described.

3.1 Top-down fabrication

Some deposition processes require high temperatures, which are not compatible with some flexible substrates that could be damaged or deformed [31]. This is why some manufacturing companies use the top-down approach to perform flexible devices.

This method has the advantage that the whole structure is done by a standard fabrication process on a rigid substrate (generally glass plate or silicon wafer) which allows the use of conventional photolithographic processes [32], [33] and has no temperature limitation for deposition layers. Once the structure is completed, it is transferred to a flexible plastic substrate through various methods such as the transfer-printing process or the release of the rigid substrate [34]. Thus, with this technique, it is possible to fabricate devices at high temperatures providing high-performance devices on flexible substrates, but the major drawbacks are the high cost, the small surface coverage (only for low dimension structures) and the use of expensive and specific equipment.

These transfer and bonding techniques could be performed by different methods and two examples of these are shown next.

Figure 1.6 [35] shows the different steps of a fabrication process, which consists of spin-coating Cytop (amorphous fluoropolymer) film onto patterned Si wafer to design a mold. Then, a graphene ink is deposited. After annealing, the structure is ready to be transferred onto a flexible polyethylene terephthalate (PET) substrate. To do this, a liquid Optical Adhesive is used between graphene and PET. The backside of the PET substrate is treated by O_2 plasma generating the peeled-off from the Cytop/Si mold by the UV-cured NOA73 adhesive layer.

Figure 1.7 is based on the EPLAR (Electronics on Plastic by Laser Release) technique developed by Philips Research. It consists of spinning and curing a layer of polyimide (PI) on top of a glass substrate using a sacrificial layer in between. At the end of the process, the polyimide layer is separated from the rigid substrate by removing the sacrificial layer by pulses of an excimer laser in the backside of the sample, causing its delaminating [36].

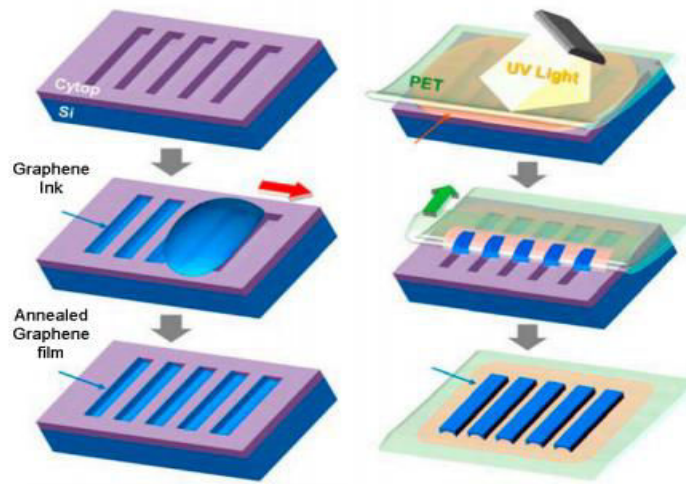


Figure 1.6. Example of top-down techniques [35].

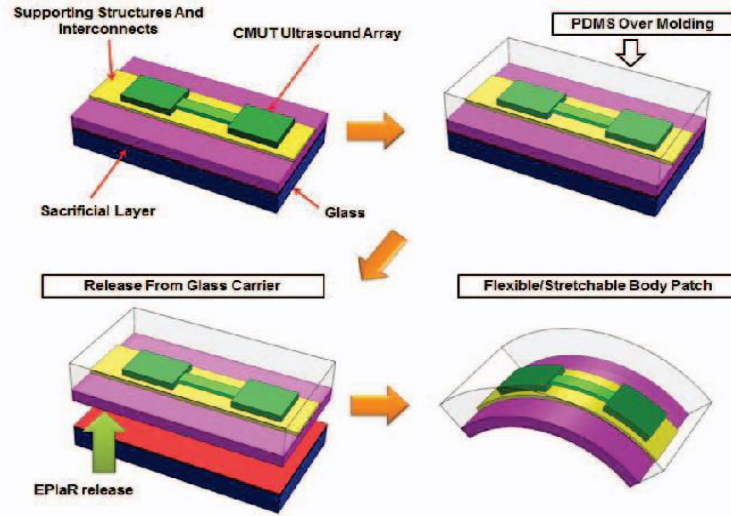


Figure 1.7. EPLAR technique illustration [36].

This technique allows adding the substrate at the end of the fabrication process (Figure 1.6), or uses a substrate that can support high-temperature range stick onto a rigid substrate until the end of the process (Figure 1.7).

Hence, this technique offers the possibility to use bio-organic substrates, making it a great option to fabricate devices that are compatible with biomedical applications. An example of this was published by KJ. Yu [37] where he explains that when the final structure is transferred to a bio-resorbable poly-(lactic-co-glycolic) acid, the technology becomes compatible with applications on the skin.

3.2 Bottom-up fabrication

This technique is the most common because direct fabrication on flexible substrates reduces the fabrication cost. However, the main disadvantage is that, depending on the substrate selected, this limits the maximum temperature used during the manufacturing process.

During the deposition steps, the temperature decrease affects the electrical and mechanical performances of the devices. For this reason, in order to achieve a good quality sensor, research focuses on bottom-up techniques and deals with new materials that have relatively good behavior at low temperature of deposition such as carbon or graphene, or on the development of new growth methods. Figure 1.8 shows an example of a bottom-up fabrication technique [38]. It illustrates the fabrication process of a tactile sensor using PDMS as a substrate. To do this, it is

first necessary to pattern some microstructures on silicon which will be used as a mold to fabricate PDMS. A rGO (reduced graphene oxide) film is then deposited on this PDMS mold and coated with ITO/PET.

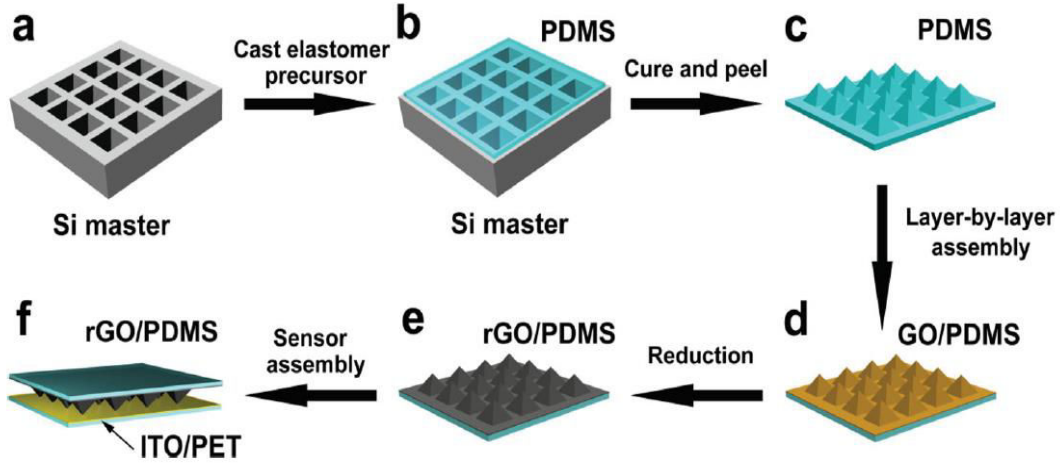


Figure 1.8. Schematic illustration of the tactile sensor device fabrication by using bottom-up approach [38].

In our case, we decided to fabricate our devices on a bottom-up technique basis, because it is the historical technique of the IETR [39], and the required equipment are available in the laboratory. It was also a good option due to the approach to the manufacturing large-area surfaces and the low cost.

In the following sections, we will present the different kinds of materials that can be used in flexible electronic devices depending on the application. It is important to select the adequate material, to explain the properties that the substrate, the semiconductor materials and the electrodes must have.

4. Substrates

The main limitations of traditional rigid electronics are intrinsic rigidity, fragility, and inability to interface with curvilinear morphological surfaces. Flexible electronic substrates offer a solution to these limitations, but their handling is more delicate, given their sensitivity to cracking and delamination due to the limited failure stress during bending deformation. These problems are discussed in detail in Chapter 2.

Depending on the nature of the application, different kinds of substrates can be used in flexible device applications. Figure 1.9 shows the degree of flexibility or mechanical properties that can be classified into the following categories: *i)* the devices that can be deformed in tension or compression, and have the ability to come back to its initial state; *ii)* the materials permanently deformed, these are not able to return to its original state, which makes their deformation and elasticity permanent; *iii)* the materials that present the ability to be deformed in the vertical plane and return to its original state.

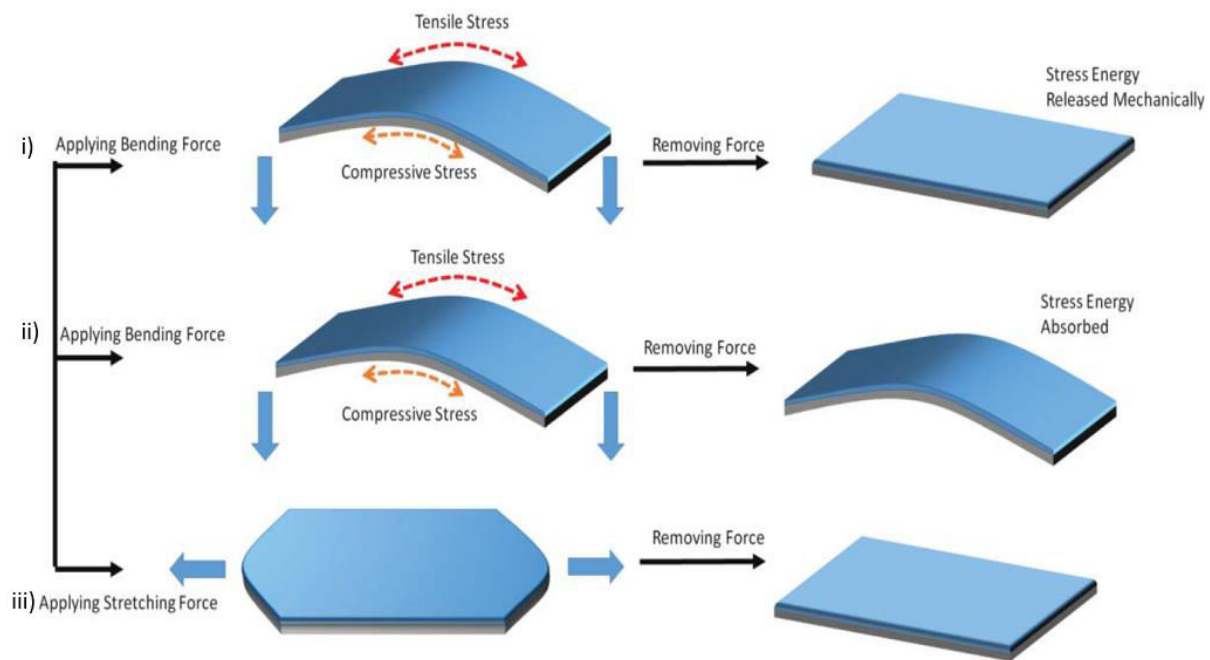


Figure 1.9. Flexibility degree of substrates.

The choice of the appropriate substrate will define the behavior of the compound structure. For this reason, in addition to the degree of flexibility, there are other requirements and properties that are important to consider when selecting this layer; some of them will be explained below.

Optical properties: According to the application, this optical parameter could be extremely relevant. For example, LCDs must have low birefringence and some displays require an optically clear substrate.

Roughness: For thin film devices, electrical properties have a direct link with the surface roughness. For this reason, for a short length, this parameter should be avoided, but for long length, a low value might be acceptable.

Thermal and thermo mechanical properties: The substrate should be compatible with the temperature during the fabrication process. The main important parameters are:

- The compatibility between the maximum temperature of the fabrication process (T_{\max}) and the transition temperature (T_g) of the substrate. A mismatch between these two parameters could create some cracks in the device's films.
- The coefficient of thermal expansion, CTE, is defined as the dimensional deformation of the substrate during the temperature process. This is defined in the equation 1.4 where ε represents the deformation of the material and ΔT represents the variation between the initial temperature of the substrate and the process at high (or low) temperature. Depending on this, the substrate undergoes compression ($\Delta T < 0$) or expansion ($\Delta T > 0$).

$$\varepsilon = \Delta(\text{CTE})(\text{substrate-film}) \cdot \Delta T(\text{deposition-ambient}) \quad (1.4)$$

The variation of the CTE produces thermal mismatch between substrate/film and therefore some cracks; this will be discussed in more detail in Chapter 2.

Chemical properties: The substrate should be compatible with chemistry products used during the fabrication process, such as acetone or acids or other corrosive chemicals [40].

Mechanical properties: This is given mainly for the degree of flexibility and should present a compromise between elastic modulus or Young's modulus of each material, the structure and thickness of the compound of each layer and the design.

Generally, there are three types of substrate material, presented below, for flexible applications.

Metal foil of stainless steel:

It is one of the most used due to its resistance to chemical processes, its high-temperature range, up to 1000 °C, its dimensional stability and its long durability. However, it presents a high surface roughness (approximately 100 nm) compared with glass or some plastic substrates (less than 1nm). For this reason, in order to have good electrical behavior, the surface of these steel foil substrates should be pre-treated with a polished or planarized film.

Thin flexible glass:

Glass becomes flexible when its thickness is less than 100 μm but the biggest drawback is the fragility and the handling.

Plastic substrates:

These types of substrates offer great flexibility, low cost and the possibility of being on a roll. However, its dimensional stability is lower than the glass one. For that reason, to find more stable dimensions, they should be submitted to a large annealing. Flexible plastic substrates include semicrystalline polymers and amorphous polymers.

For our application, metal foil and glass were not a good option due to the high rigidity and low degree of flexibility. For that reason we opt for a plastic substrate. The most used plastic substrates for developing flexible electronic components are polyesters such as PEN (polyethylene naphthalene), PET (polyethylene terephthalate) and PI (polyimide) due to relatively high elastic moduli and their good resistance to chemicals. The substrates of PEN and PET are characterized by a high level of transparency, more than 80%, and a low roughness surface [41]. However, the maximum temperature process is up to around 155 $^{\circ}\text{C}$ for PEN [42] and around 250 $^{\circ}\text{C}$ for PET [43].

For plastic substrates, it is important to control the maximum temperature process and not to exceed the glass transition temperature, which would involve substrate deformation. An example of that is shown in Figure 1.10 [31]. PET has been submitted to different thermal treatments to the point of complete destruction.

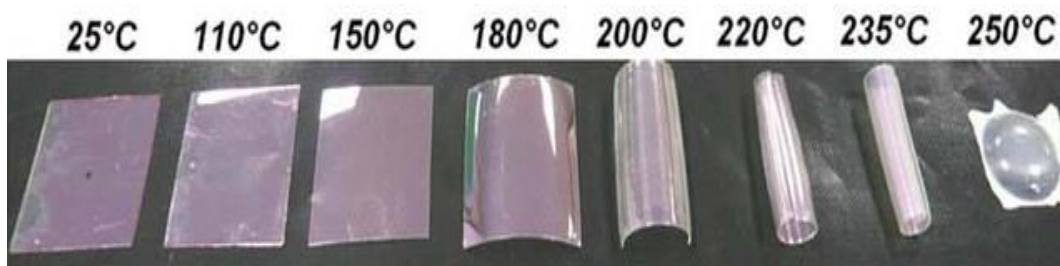


Figure 1.10. PET/ITO substrates deformation after thermal treatment [31].

Max. Dep. Temp. (°C)	Material	Properties
400 °C [44]	Polyimide (Kapton®)	Orange color, high thermal expansion coefficient, good chemical resistance, expensive, high moisture absorption
343 °C [45]	Polyetheretherktone (PEEK)	Amber, good chemical resistance, expensive, low moisture absorption
343 °C [46]	Polyethersulphone (PES)	Clear, good dimensional stability, poor solvent resistance, expensive, moderate moisture absorption
354 °C [47]	Polyetherimide (PEI)	Strong, brittle, hazy color, expensive
155 °C [42]	Polyethylene Naphthalate (PEN)	Clear, moderate CTE, good chemical resistance, inexpensive, moderate moisture absorption
250 °C [43]	Polyethylene terephthalate (PET)	Clear, moderate CTE, good chemical resistance, inexpensive, moderate moisture absorption

Table 1.2. Properties of main plastic substrates.

5. Semiconductor and dielectric materials

One of the greatest challenges in flexible electronics is to obtain high performance semiconductor and dielectric materials.

We present below the two types of organic and inorganic semiconductors.

5.1 Organic semiconductor in flexible electronics

Organic semiconductors are attractive because they can be processed at low or at room temperature and they have good mechanical flexibility. However, these materials have some disadvantages such as poor crystallinity, low mobility, and possible degradation in the air which requires encapsulation with a thin inorganic film [48].

Generally, the price of these materials and their fabrication process is higher compared to inorganic semiconductors. Moreover, some organic semiconductors such as pentacene require a special preparation procedure due to their high sensitivity to contamination [49]. The most popular processes to fabricate organics electronics are the followings:

Spin coating: consists in spreading the semiconductor material by centrifugal force on the substrate when this rotates at high speed. With this technique, it is complicated to control the thickness and the uniformity of the material.

Thermal evaporation: the organic semiconductor is evaporated under vacuum. Generally, a shadow mask is used to define the structure, as this avoids the photolithography step, knowing that many organic semiconductors are sensitive to solvents [50].

Inkjet printing: consists of printing the organic solution. This could be done by different techniques such as serigraphy, flexography or roll to roll technique [51].

Organic materials have some disadvantages when compared to inorganic semiconductors, such as free carrier mobility which is several orders of magnitude lower [40].

For industry, the need of low-cost manufacturing processes for large-scale flexible electronics and the low deposit uniformity for large substrate surfaces make inorganic technology the most popular technology on the electronics market.

Nevertheless, organic semiconductors have significant advantages, they have good intrinsic flexibility, making them a good choice to fabricate flexible electronic devices. Moreover, this technology has a promising future especially in the fields of healthcare, biosensors or wearable applications that need to be compatible with the body.

5.2 Inorganic semiconductor flexible electronics

Traditional electronic products are developed with this kind of semiconductor because of their excellent physical and chemical properties such as high electrical and thermal conductivity. Silicon is one of the most widely used products in the semiconductor industry. Some generalities of silicon and its use in flexible electronics technology will be presented.

Advances in flexible electronics technology have required the study of other inorganic nanomaterial such as Graphene Oxide (GO) [52], [53] or GaAs [54] with the goal to reduce the rigidity and fragility of inorganic materials. Another alternative is to increase their flexibility, for example by reducing their thickness.

Silicon technology is one of the most developed technologies on the market. In the laboratory, we chose silicon as the main material for the implementation of our sensors. Silicon can exist in many allotropic forms (Fig. 1.11). Its conductivity depends on the elaboration parameters such as gas dilution, pressure, deposition temperature, layer thickness, doping levels and doping materials... All these conditions will also determine the quality of the material, the resistance of contact between the different layers and therefore the performance of devices.

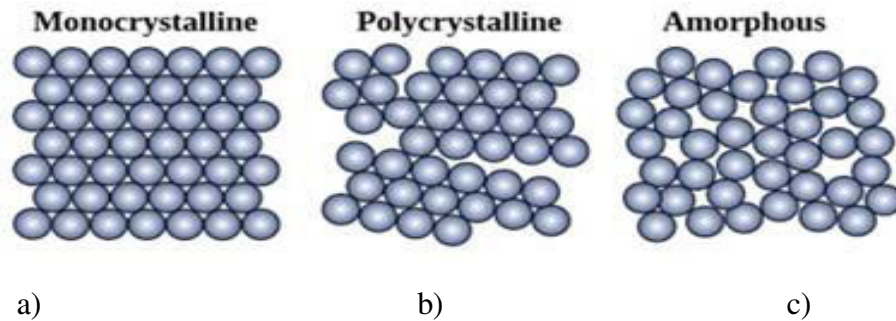


Figure 1.11. Allotropic states of silicon. a) monocrystalline, b) polycrystalline, c) amorphous.

Single crystalline silicon (sc-Si) also called monocrystalline silicon:

It presents a "diamond" crystalline lattice as shown in Figure 1.11 (a). The temperature required for the growth is higher than 900 °C, which is very high for flexible substrates; only a few substrates can support this range such as flexible stainless steel foil. Moreover, because of this uniform structure, the behavior of the crystal is a bad option for using it in the high deformation measurement. However, silicon in this state is widely used in the industry in the form of wafers whose dimensions can vary.

Amorphous Silicon (a-Si):

The atomic structure of amorphous silicon (Fig. 1.11 c) is characterized by the fact that it does not present a crystalline structure or order, making it a good candidate for flexible electronic [55]. Generally, it is deposited at a temperature lower than 250 °C [56] making it compatible with a large number of flexible substrates such as PET or Kapton®. Thanks to its lattice, it presents good flexibility but a lot of electrical instability and poor performance.

Polycrystalline, microcrystalline and nanocrystalline silicon:

It is a particular form of silicon. This is an intermediate state between amorphous and monocrystalline silicon. Figure 1.11 (b) presents well-ordered zones of crystalline grains and

non-crystallized (amorphous) zones. Depending on the grain size, it can be known as microcrystalline silicon ($\mu\text{c-Si}$) if the grain size is between 1 nm and 1 μm or nanocrystalline (nc-Si) when the grain size is less than 10 nm. Figure 1.12 shows the classification of silicon according to the grain size and the temperature deposition range.

Compared to amorphous silicon, it offers a better stability [57], and a higher mobility [58]. It is widely used in thin film transistor fabrication [59] [60]. There are different techniques to deposit this material, such as sputtering or different chemical vapor deposition (CVD) techniques. The deposition techniques used in the IETR will be widely described in Chapter 2.

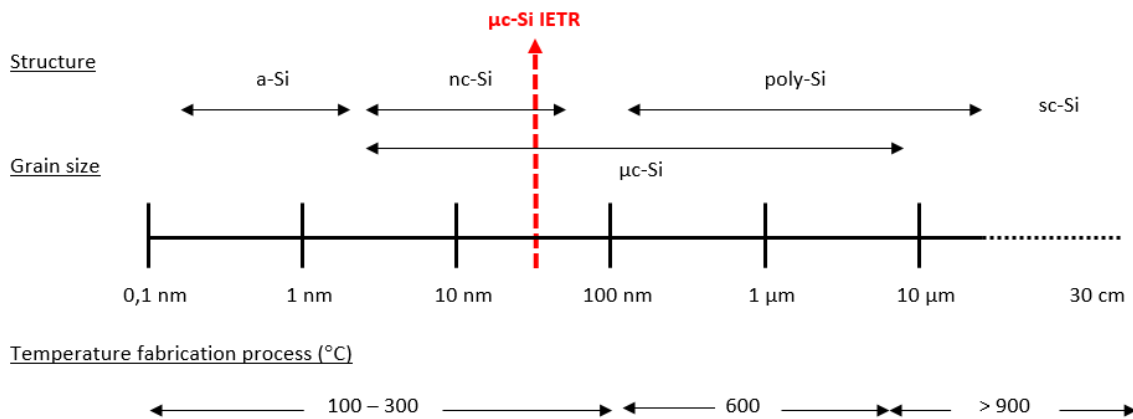


Figure 1.12. Classification of silicon as a function of the grain size and the temperature deposition range [61].

6. Metal electrodes

When flexible devices are submitted to bending or stretching deformation, all the layers of the sensor undergo this effect, so for flexible sensing devices, mechanical flexibility and stability of the electrodes must be taken into account.

Thick metals cannot be used for these applications, however ultra-thin metals can support bending conditions without easily breaking. This is due to the bending strain which decreases proportionally with thickness. In addition to thickness reduction, to reduce fractures, it is necessary to have a good design such as wavy structures, serpentine patterns, coiled springs [62] [63].

Conventional fabrication of metal electrodes in the laboratory consists of evaporation. The deposition is the same as used on hard substrates such as silicon wafers, but this can damage the soft substrate due to the use of strong solvents, high temperatures or high pressures [64]. There are other alternatives such as solution-based wet chemical methods, including printing and plating techniques which allow rapid, low temperature and cost effective fabrication.

There are some considerations for a good flexible electrode, such as its high electrical conductivity, its good adhesion and its great robustness against mechanical deformations. The most commonly used metal for electrode fabrication include gold (Au), silver (Ag), copper (Cu) and nickel (Ni), but for flexible applications some materials such as graphene, carbon nanotubes (CNTs) or metal nanowire (NWs) are widely used because of their high conductivity and flexibility.

However, taking into account the cost/conductivity ratio [65], silver is a good option for our devices. The performance of the electrodes can be evaluated by measuring the electrical conductivity through the contact resistivity between the metal and the semiconductor. This is deeply explained in Chapter 3, with some measurements in our devices via the TLM device. In addition to the electrical characterization, it is necessary to quantify the mechanical flexibility and robustness by performing the “bending test” as mentioned in the literature [66] [67]. As shown in Figure 1.13, the electrode is repeatedly bent into a curvature shape and the change of the bulk resistance is measured during the cycles.

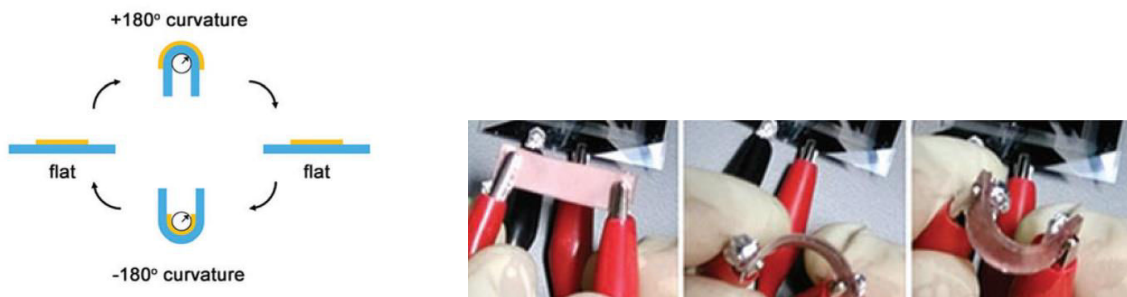


Figure 1.13. Bending test on metallic electrodes.

7. Conclusion

This chapter allows us to present a general overview of pressure sensors. Characterization parameters, working principle and main applications in the electronic market were described. Moreover, the different methods used to fabricate flexible electronics, top-down or bottom-up were discussed.

In order to optimize the mechanical performance of flexible electronics, all the layers of the global structure should be chosen in function of the application of the device. Hence, a comparison was done between the different materials that form the sensor's structure such as the substrate choice, because this will determine the degree of flexibility of the structure, the semiconductor and dielectric materials, and the effect of metal electrodes in the electrical and mechanical performance. The synthesis and study of the properties of silicon, material used in our devices are also presented.

All these general information will help us to better understand the considerations that should be taken into account to fabricate flexible devices as presented in the next chapter.

8. References

- [1] Y. Zang, F. Zhang, C. Di, and D. Zhu, ‘Advances of flexible pressure sensors toward artificial intelligence and health care applications’, *Mater. Horiz.*, vol. 2, no. 2, pp. 140–156, 2015.
- [2] L. Persano, C. Dagdeviren, Y. Su, Y. Zhang, S. Girardo, D. Pisignano, Y. Huang and J. A. Rogers ‘High performance piezoelectric devices based on aligned arrays of nanofibers of poly(vinylidene fluoride-co-trifluoroethylene)’, | *Nature Communications*, vol. 4, pp. 1633-1643, 2013 <https://www.nature.com/articles/ncomms2639>.
- [3] N. Lu, C. Lu, S. Yang and John Rogers, ‘Highly Sensitive Skin-Mountable Strain Gauges Based Entirely on Elastomers’, *Advanced Functional Materials*, vol. 22, pp. 4044-4050, 2012, <https://onlinelibrary.wiley.com/doi/abs/10.1002/adfm.201200498>.
- [4] C. Pang, G-Y. Lee, T-I. Kim, S.M. Kim, H.N. Kim, S-H. Ahn and K-Y. Suh, ‘A flexible and highly sensitive strain-gauge sensor using reversible interlocking of nanofibres’, *Nature Materials*, vol. 11, pp. 795-801, 2012, <https://www.nature.com/articles/nmat3380>.
- [5] M. Kaltenbrunner, T. Sekitani, J. Reeder, T. Yokota, K. Kuribara, T. Tokuhara, M. Drack, R. Schwödjaer, I. Graz, S. Bauer-Gogonea, S. Bauer and T. Someya, *Nature*, ‘An ultra-lightweight design for imperceptible plastic electronics’, *Nature*, vol. 499, no. 7459, pp. 458–463, 2013.
- [6] M. Ramuz, B. C-K. Tee, J. B.-H. To and Z. Bao, ‘Transparent, Optical, Pressure-Sensitive Artificial Skin for Large-Area Stretchable Electronics’ *Advanced Materials*, vol. 24, no 24, pp. 3223-3227, 2012, <https://onlinelibrary.wiley.com/doi/abs/10.1002/adma.201200523>.
- [7] T. Sekitani and T. Someya, ‘Stretchable, Large-area Organic Electronics’, *Advanced Functional Materials*, vol. 22, no. 20, pp. 2228–2246, 2010.
- [8] G.A. Salvatore, N. Münzenrieder, T. Kinkelde, L. Petti, C. Zysset, I. Strebel, L. Büthe and G. Tröster, ‘Wafer-scale design of lightweight and transparent electronics that wraps around hairs’ *Nature Communications*, vol.5, pp 2982-2990, 2014, <https://www.nature.com/articles/ncomms3982>.
- [9] X. Wu, Y. Han, X. Zhang, Z. Zhou and C. Lu, ‘Large-Area Compliant, Low-Cost, and Versatile Pressure-Sensing Platform Based on Microcrack-Designed Carbon

- Black@Polyurethane Sponge for Human–Machine Interfacing’, *Advanced Functional Materials*, vol. 26, no 34, pp. 6246–6256, 2016,
<https://onlinelibrary.wiley.com/doi/abs/10.1002/adfm.201601995>.
- [10] X. Huang, Y. Liu, H. Cheng, W.-J. Shin, J.A. Fan, Z. Liu, C.J. Lu, G.W. Kong, K. Chen, D.Patnaik, S.H. Lee, S.Hage-Ali, Y. Huang and J.A. Rogers, ‘Materials and Designs for Wireless Epidermal Sensors of Hydration and Strain’, *Advanced Functional Materials*, vol. 24, no. 25, pp. 3846–3854, 2014.
- [11] S. Gong, D.T.H. Lai, B. Su, K.J. Si, Z. Ma, L.W. yap, P. Guo and W. Cheng, ‘Highly Stretchy Black Gold E-Skin Nanopatches as Highly Sensitive Wearable Biomedical Sensors’, *Advanced Functional Materials*, vol. 1, no. 4, pp. 1400063, 2015.
- [12] C.L. Choong, M.B. Shim, B.S. Lee, S. Jeon, D.S. Ko, T.H. Kang, J. Bae, S.H. Lee, K.E. Byun, J. Im, Y. Jin Jeong, C.E. Park, J.J. Park and U.I. Chung, ‘Highly Stretchable Resistive Pressure Sensors Using a Conductive Elastomeric Composite on a Micropyramid Array’, *Advanced Functional Materials*, vol. 26, no. 21, pp. 3451–3458, 2014.
- [13] I. Graz, M. Krause, S. Bauer-Gogonea, S. Bauer, S.P. Lacour, B. Ploss, M. Zirki, B. Stadlober and S. Wagner, ‘Flexible active-matrix cells with selectively poled bifunctional polymer-ceramic nanocomposite for pressure and temperature sensing skin’, *J. Appl. Phys. Lett.*, vol. 106, no. 3, pp. 034503, 2009.
- [14] S. Wu, R.B. Ladani, J. Zhang, K. Ghorbani, X. Zhang, A.P. Mouritz, A.J. Kinloch and C.H. Wang, ‘Strain Sensors with Adjustable Sensitivity by Tailoring the Microstructure of Graphene Aerogel/PDMS Nanocomposites’, *ACS Appl. Mater. Interfaces*, vol. 8, no. 37, pp. 24853–24861, 2016.
- [15] L. Pan, A. Chortos, G. Yu, Y. Wang, S. Isaacson, R. Allen, Y. Shi, R. Dauskardt, Z. Bao, ‘An ultra-sensitive resistive pressure sensor based on hollow-sphere microstructure induced elasticity in conducting polymer film’, *Nature Communications*, vol. 5, pp. 3002–3010, 2014.
- [16] S. Middelhoek and S. A. Audet, ‘Silicon Sensors’, published by Academic Press, Ltd, London, vol. 2, pp. 376, 1989, <https://infoscience.epfl.ch/record/24206>.
- [17] R. Ramalingame, Z. Hu, C. Gerlach, D. Rajendran, T. Zubkova, R. Baumann, O. Kanoun., ‘Flexible piezoresistive sensor matrix based on a carbon nanotube PDMS composite for dynamic pressure distribution measurement’, *Nature, Scientific Reports*, vol. 8, no. 1, pp. 1–7, 2019.

- [18] M. A. S. Mohammad Haniff, S.M. Hafiz, K.A.A. Wahid, Z. Endut, H.W. Lee, D.C.S. Bien, I.A. Azid, M.Z. Abdullah, N.M. Huang and S.A. Rahman, 'Piezoresistive effects in controllable defective HFTCVD graphene-based flexible pressure sensor', *Nature, Scientific Reports*, vol. 5, pp. 14751-1461, 2015.
- [19] S. Xu, Y. Qin, C. Xu, Y. Wei, R. Yang and Z.L. Wang, 'Self-powered nanowire devices', *Nature Nanotechnology*, vol. 5, pp. 366-373, 2010, <https://www.nature.com/articles/nnano.2010>.
- [20] G. Zhu, Q. Yang, T. Zhang, Q. Jing, J. Chen, Y.S. Zhou, P. Bai and Z.L. Wang, 'Self-Powered, Ultrasensitive, Flexible Tactile Sensors Based on Contact Electrification', *Nano Lett.*, vol. 14, no. 6, pp. 3208–3213, 2014.
- [21] C. Li, S. Lee, A. Gorton, M. J. Schulz, and C. H. Ahn, 'Dome or bump-shaped PVDF-TrFE films developed with a new mold-transfer method for flexible tactile sensors', in *2007 IEEE 20th International Conference on Micro Electro Mechanical Systems (MEMS)*, pp. 337–340, 2007.
- [22] C. Chang, V. H. Tran, J. Wang, Y.-K. Fuh, and L. Lin, 'Direct-Write Piezoelectric Polymeric Nanogenerator with High Energy Conversion Efficiency', *Nano Lett.*, vol. 10, no. 2, pp. 726–731, 2010.
- [23] P. Rey, P. Charvet, M. T. Delaye, and S. A. Hassan, 'A high density capacitive pressure sensor array for fingerprint sensor application', in *Proceedings of International Solid State Sensors and Actuators Conference (Transducers '97)*, vol. 2, pp. 1453–1456, 1997.
- [24] H. Lee, J. Chung, S. Chang, and E. Yoon, 'Normal and Shear Force Measurement Using a Flexible Polymer Tactile Sensor With Embedded Multiple Capacitors', *J. Microelectromechanical Syst.*, vol. 17, no. 4, pp. 934–942, 2008.
- [25] Y. Huang, H. Yuan, W. Kan, X. Guo, C. Liu, and P. Liu, 'A flexible three-axial capacitive tactile sensor with multilayered dielectric for artificial skin applications', *Microsyst. Technol.*, vol. 23, no. 6, pp. 1847–1852, 2017.
- [26] J. A. Dobrzynska and M. A. M. Gijs, 'Polymer-based flexible capacitive sensor for three-axial force measurements', *J. Micromechanics Microengineering*, vol. 23, no. 1, pp. 1-11, 2012.

- [27] R. Surapaneni, Q. Guo, Y. Xie, D. J. Young, and C. H. Mastrangelo, 'A three-axis high-resolution capacitive tactile imager system based on floating comb electrodes', *J. Micromechanics Microengineering*, vol. 23, no. 7, pp. 075004-075016, 2013.
- [28] A. M. Almassri, W.Z.Wan Hasan, S.A. Ahmad, A.J. Ishak, A.M. Ghazali, D.N. Talib and C. Wada, 'Pressure Sensor: State of the Art, Design, and Application for Robotic Hand', *Journal of Sensors*, Vol. 201512, pp. 1-12, 2014,
<https://www.hindawi.com/journals/js/2015/846487/abs/>.
- [29] L. Yang, I. Akhatov, M. Mahinfalah, and B. Z. Jang, 'Nano-fabrication: A review', *J. Chin. Inst. Eng.*, vol. 30, pp. 441–446, 2007.
- [30] S.R. Quake and A. Scherer, 'From Micro- to Nanofabrication with Soft Materials', *Science*, vol. 290, no 5496, pp. 1536-1540, 2000,
<https://science.sciencemag.org/content/290/5496/1536>.
- [31] V. Zardetto, T. M. Brown, A. Reale, and A. D. Carlo, 'Substrates for flexible electronics: A practical investigation on the electrical, film flexibility, optical, temperature, and solvent resistance properties', *J. Polym. Sci. Part B Polym. Phys.*, vol. 49, no. 9, pp. 638–648, 2011.
- [32] H.J. Levinson, 'Lithography Process Control', *Spie Press Book*, 1999.
<https://spie.org/publications/book/322162?SSO=1>.
- [33] J. Melngailis, A. A. Mondelli, I. L. Berry, and R. Mohondro, 'A review of ion projection lithography', *J. Vac. Sci. Technol. B Microelectron. Nanometer Struct. Process. Meas. Phenom.*, vol. 16, no. 3, pp. 927–957, 1998.
- [34] C. H. Lee, D. R. Kim, and X. Zheng, 'Transfer Printing Methods for Flexible Thin Film Solar Cells: Basic Concepts and Working Principles', *ACS Nano*, vol. 8, no. 9, pp. 8746–8756, 2014.
- [35] D. Song, A. Mahajan, E. B. Secor, M. C. Hersam, L. F. Francis, and C. D. Frisbie, 'High-Resolution Transfer Printing of Graphene Lines for Fully Printed, Flexible Electronics', *ACS Nano*, vol. 11, no. 7, pp. 7431–7439, 2017.
- [36] S. Joshi, S. Yazadi, V. Henneken, R. Dekker, and R. Sanders, 'Conformable body patches for ultrasound applications', in *IEEE 17th Electronics Packaging and Technology Conference (EPTC)*, Singapore, 2015, pp. 1–4, 2015.
- [37] K.J. Yu, D. Kuzum, S.W. Hwang, B.H. Kim, H. Juul, N.H. Kim, S.M. Won, K. Chiang, M. Trumpis, A.G. Richardson, H. Cheng, H. Fang, M. Thomson, H. Bink, D. Talos, K.J. Seo,

- H.N. Lee, S.K. Kang, J.H. Kim, J.Y. Lee, Y. Huang, F.E. Jensen, M.A. Dichter, T.H. Lucas, J. Viventi, B. Litt and J.A. Rogers, ‘Bioresorbable silicon electronics for transient spatiotemporal mapping of electrical activity from the cerebral cortex’, *Nature and Materials.*, vol. 15, no. 7, pp. 782–791, 2016.
- [38] B. Zhu, Z. Niu, H. Wang, W.R. Leon, H. Wang, Y. Li, L. Zheng, J. Wei, F. Huo and X. Chen, ‘Microstructured Graphene Arrays for Highly Sensitive Flexible Tactile Sensors’, *Small*, vol. 10, no 18, pp. 3625-3631, 2014.
- [39] S. Janfaoui, ‘Électronique CMOS en silicium microcristallin sur substrat flexible transparent’, thesis, Rennes 1, 2012.
- [40] S.R. Forrest, ‘The path to ubiquitous and low-cost organic electronic appliances on plastic’, *Nature* vol. 428, pp. 911-918, 2004, <https://www.nature.com/articles/nature02498>.
- [41] ‘Overview of materials for PEN-PET’
<http://www.matweb.com/search/DataSheet.aspx?MatGUID=920e5994b53e4e8fa2157a6136cb8d0c>.
- [42] ‘Goodfellow Polyethylene Naphthalate (PEN) Film’
<http://www.matweb.com/search/datasheet.aspx?MatGUID=60dc5dfcf5ba48f9bb4fe2fc7d7dd4bf>.
- [43] ‘Overview of materials for Polyethylene Terephthalate (PET), Unreinforced’.
<http://www.matweb.com/search/datasheet.aspx?MatGUID=a696bdcdf6f41dd98f8eec3599ea20&ckck=1>.
- [44] ‘DEC-Kapton-HN-datasheet.pdf’. <https://www.dupont.com/content/dam/dupont/products-and-services/membranes-and-films/polyimide-films/documents/DEC-Kapton-HN-datasheet.pdf>
- [45] ‘Polyetheretherktone (PEEK)-datasheet.pdf’.
https://www.victrex.com/~media/datasheets/victrex_tds_450g.pdf
- [46] ‘Polyethersulfone (PES) Product Data Sheet - RTP Company’.
<http://web.rtpcompany.com/info/data/1400/RTP1400.htm>.
- [47] ‘Polyetherimide (PEI) Product Data Sheet - RTP Company’.
<http://web.rtpcompany.com/info/data/2100/RTP2107.htm>.

- [48] J. S. Lewis and M. S. Weaver, 'Thin-film permeation-barrier technology for flexible organic light-emitting devices', *IEEE J. Sel. Top. Quantum Electron.*, vol. 10, no. 1, pp. 45–57, 2004.
- [49] T. Kelley, 'High-performance Pentacene Transistors - Organic Electronics', Book Editor Dr. H. Klauk 2006, <https://onlinelibrary.wiley.com/doi/abs/10.1002/3527608753.ch2>.
- [50] T. Someya, T. Sekitani, S. Iba, Y. Kato, H. Kawaguchi, and T. Sakurai, 'A large-area, flexible pressure sensor matrix with organic field-effect transistors for artificial skin applications', *Proc. Natl. Acad. Sci.*, vol. 101, no. 27, pp. 9966–9970, 2004.
- [51] B. E. Kahn, 'Organic Electronics Technology', " Organic Electronics Association 1st Edition (Frankfurt Am Main: VDMA Verlag, pp.16, 2006.
- [52] Y. Yang, X. Yang, X. Zou, S. Wu, D. Wan, A. Cao, L. Liao, Q. Yuan and X. Duan, 'Ultrafine Graphene Nanomesh with Large On/Off Ratio for High-Performance Flexible Biosensors', *Advance Functional Materials*, vol. 27, no. 19, p. 1604096 (10pp.), 2017.
- [53] S. Bae, H. Kim, Y. Lee, X. Xu, J.S. Park, Y. Zheng, J. Balakrishnan, T. Lei, H. Ri Kim, Y. Il Song, Y.J. Kim, K. S. Kim, B. Özyilmaz, J.H. Ahn, B. Hee Hong and S. Iijima, 'Roll-to-roll production of 30-inch graphene films for transparent electrodes', *Nature Nanotechnology*, vol.5, pp. 574-578, 2010, <https://www.nature.com/articles/nnano.2010.132?draft=journal>.
- [54] Y. Sun and J. A. Rogers, 'Fabricating Semiconductor Nano/Microwires and Transfer Printing Ordered Arrays of Them onto Plastic Substrates', *Nano Lett.*, vol. 4, no. 10, pp. 1953–1959, 2004.
- [55] H. Gleskova, S. Wagner, W. Soboyejo, and Z. Suo, 'Electrical response of amorphous silicon thin-film transistors under mechanical strain', *J. Appl. Phys.*, vol. 92, no. 10, pp. 6224–6229, 2002.
- [56] R.C. Chittick, J.H. Alexander and .F. Sterling, 'The Preparation and Properties of Amorphous Silicon', *J. Electrochem. Soc.*, vol. 116, no 1, pp. 77-81, 1969, <http://jes.ecsdl.org/content/116/1/77.short>
- [57] K. Belarbi, K. Kandoussi, N. Coulon, C. Simon, R. Cherfi, A. Fedala and T. Mohammed-Brahim, 'Stability of Microcrystalline Silicon TFTs', *ECS Trans.*, vol. 16, no. 9, pp. 121–129, 2008.

- [58] C.-H. Lee, A. Sazonov, and A. Nathan, ‘High-mobility nanocrystalline silicon thin-film transistors fabricated by plasma-enhanced chemical vapor deposition’, *Appl. Phys. Lett.*, vol. 86, no. 22, p. 222106 (3pp.), 2005.
- [59] P.-C. Kuo, A. Jamshidi-Roudbari, and M. Hatalis, ‘Effect of mechanical strain on mobility of polycrystalline silicon thin-film transistors fabricated on stainless steel foil’, *Appl. Phys. Lett.* 91, no 24, p. 3507 (4pp.), 2007, <https://doi.org/10.1063/1.2824812>
- [60] J. H. Cheon, J. H. Bae, and J. Jang, ‘Mechanical stability of poly-Si TFT on metal foil’, *Solid-State Electron.*, vol. 52, no. 3, pp. 473–477, 2008.
- [61] Y. Krevran ‘Cartographie d’un champ de pression induit par l’occlusion dentaire’. Thesis Rennes 1, 2016.
- [62] D.-H. Kim, R. Ghaffari, N. Lu, and J. A. Rogers, ‘Flexible and stretchable electronics for biointegrated devices’, *Annu. Rev. Biomed. Eng.*, vol. 14, pp. 113–128, 2012.
- [63] D.-H. Kim, J. Xiao, J. Song, Y. Huang, and J. A. Rogers, ‘Stretchable, curvilinear electronics based on inorganic materials’, *Adv. Mater. Deerfield Beach Fla*, vol. 22, no. 19, pp. 2108–2124, 2010.
- [64] R. V. Martinez, ‘Flexible Electronics: Fabrication and Ubiquitous Integration’, *Micromachines*, vol. 9, no 11, p. 605 (1 pp.), 2018.
- [65] D. Wang, Y. Zhang, X. Lu, Z. Ma, C. Xie, and Z. Zheng, ‘Chemical formation of soft metal electrodes for flexible and wearable electronics’, *Chem. Soc. Rev.*, vol. 47, no. 12, pp. 4611–4641, 2018.
- [66] C.-H. Liu and X. Yu, ‘Silver nanowire-based transparent, flexible, and conductive thin film’, *Nanoscale Res. Lett.*, vol. 6, no. 1, p. 75 (9 pp.), 2011.
- [67] Y. Yu, J. Zeng, C. Chen, Z. Xie, R. Guo, Z. Liu, X. Zhou and Z. Zheng, ‘Three-dimensional compressible and stretchable conductive composites’, *Adv. Mater.*, vol. 26, no. 5, pp. 810–815, 2014.

CHAPTER 2 - N-type μ C-Si investigated as a pressure sensor

1. Introduction

Nowadays, there are many flexible technologies used to perform physiological measurements. The aim of this section is to give an overview of flexible electronic devices; how to work with thin-film layers or how to select them depending on the application.

First, an introduction of the techniques used in the IETR laboratory to deposit microcrystalline silicon ($\mu\text{c-Si}$) at low temperature is presented. The piezoresistive properties of these materials are explained.

In addition, some points about the highlight of the fabrication process of our devices and the problems found during the development are discussed.

2. Deposition techniques of $\mu\text{c-Si}$ at low temperature

Generally, the mechanical properties of any flexible thin-film material will strongly depend on the temperature used for its deposition.

In IETR laboratory, the most widely used deposition method for microcrystalline silicon at low temperature is plasma-enhanced chemical vapor deposition (PECVD). While there are other methods available in the laboratory for depositing silicon, such as sputtering or low-pressure chemical vapor deposition (LPCVD), these techniques, with the temperature limitation for deposition, don't achieve the same quality than PECVD.

Indeed, microcrystalline silicon deposited at low temperature, 165 °C, has been optimized in the laboratory in 2007 [1] making it compatible with flexible substrates such as PEN or Kapton®.

However, the acquisition by the laboratory of a new machine based on the technique of inductively-coupled-plasma chemical vapor deposition (ICP-CVD), requires us to investigate whether this method allows us to obtain microcrystalline silicon with better characteristics.

Although both techniques belong to the same principle of chemical vapor deposition (CVD) that it is based on deposit of thin films from vapor phase by the decomposition of chemicals on the substrate surface, there are some differences between them. For that reason, their working principle and a comparison between these two techniques are presented below.

2.1 Description of deposition system with PECVD reactor

Plasma enhanced chemical vapor deposition (PECVD) is a process used to deposit thin films from a gas vapor state to a solid state on a substrate. When a radio frequency (RF) power is generated between two electrodes, the plasma is created, involving the chemical reactions of the gases. The plasma produces energetic electrons, ions and free radicals, which assist the chemical reactions. The machine is formed by 3 parts: deposition reactor, pumping system and gases management system.

- The deposition reactor has two parallel electrodes, the anode that supports the substrate and is connected to the ground and the cathode that it is connected to a RF source. Between the cathode and the RF source, there is a tuning box that allows the compensation of the reflected power. By adjusting it, it is possible to adjust the RF power applied. The substrate can be heated up to 350 °C, depending on the film requirements. RF generator creates an alternative field at 13.56 MHz, this power can be regulated from microwaves to higher MHz [2], [3]. The distance between the electrodes is adjustable and this parameter can be very relevant to obtain a good quality film.
- Pumping system is constituted by a primary pump that provides a vacuum level about 10^{-2} mbar and a secondary pump that adjust the vacuum level until 10^{-6} mbar.
- Gases management system: the gases used during the deposition are controlled by flow meters that are located behind the reactor. The main gas used are Silane (SiH_4), Hydrogen (H_2) and Argon (Ar). Other gases that can be added in order to obtain doped layers: phosphine (PH_3) or arsine (AsH_3) for n-doped layers or diborane (B_2H_6) for p-doped layers.

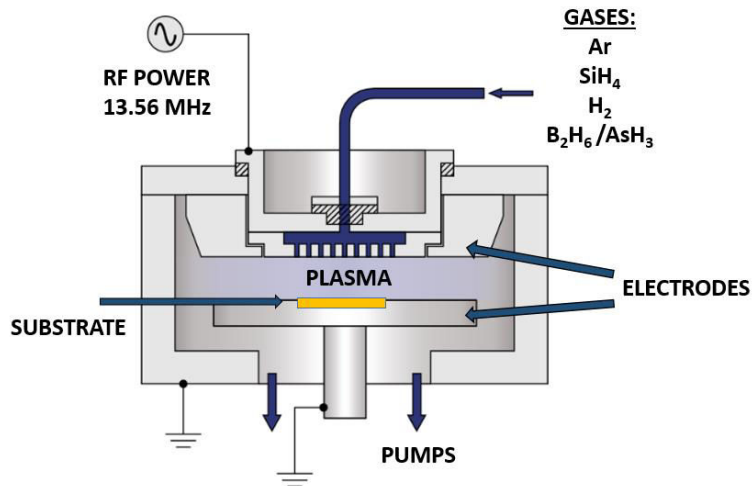


Figure 2.1. Schematic PECVD reactor.

2.2 Description of deposition system with ICP-CVD reactor

High Density Plasma Chemical Vapor Deposition (HDPCVD) is a special form of CVD technique that employs an Inductively Coupled Plasma (ICP) source to generate a higher density plasma with lower deposition pressures and temperatures than PECVD system.

Using higher plasma density, it could be possible to obtain some advantages as for example, high-quality films using lower deposition temperatures than PECVD (typically 80 °C to 150 °C) or a better uniformity.

Generally, the inert gases go through the ICP source, and the reactive gases are introduced through a gas ring that is close to the lower electrode. Depending on the film required property, the lower electrode can be powered (~ 10 W) or left floating (~ 0 W).

Most ICP-CVD systems process through a turbo molecular pump which limits the gas flowed into the chamber, and leads to lower deposition rates.

As in PECVD machine, a parallel electrodes reactor are used. The sample is placed on a grounded bottom electrode and RF bias voltage is applied to the upper electrode. This forms the plasma. For ICP-CVD machine the bottom electrode can be heated in a range 100-400 °C.

To deposit at low temperatures high-density films, even with temperatures lower than 100 °C, a high- density-plasma (HDP) source is used, in which the electrons of the plasma are excited in a direction parallel to the chamber boundaries. The HDP source corresponds to the inductively

coupled plasma (ICP) chamber. On this module, the plasma is driven by a magnetic potential set up by a coil wound outside chamber walls, as shown on Figure 2.2. The electron current direction is opposite to that of the coil currents which are, by design, parallel to the chamber surfaces.

The inductively coupled coil is linked to a 13.56 MHz RF generator. This generator is not the same as the one used to power the lower electrode. This lower electrode, as in PECVD, is powered separately by another 13.56 MHz generator, which enables independent control of the energy of the ions of the plasma. The dissociation of the plasma and the density of the incident ions in the chamber is controlled by ICP coil power.

As previously commented, ICP-CVD is a new deposition technique in the laboratory. By this way, it appeared the necessary to investigate which are the optimum conditions to perform the N-type $\mu\text{-Si}$ deposition at low-temperature. With this machine, we will try to achieve film densities higher or similar to PECVD but with better step coverage and at lower process temperatures. Also, it can offer the possibility to control the stress induced in the films due to the low ion energies.

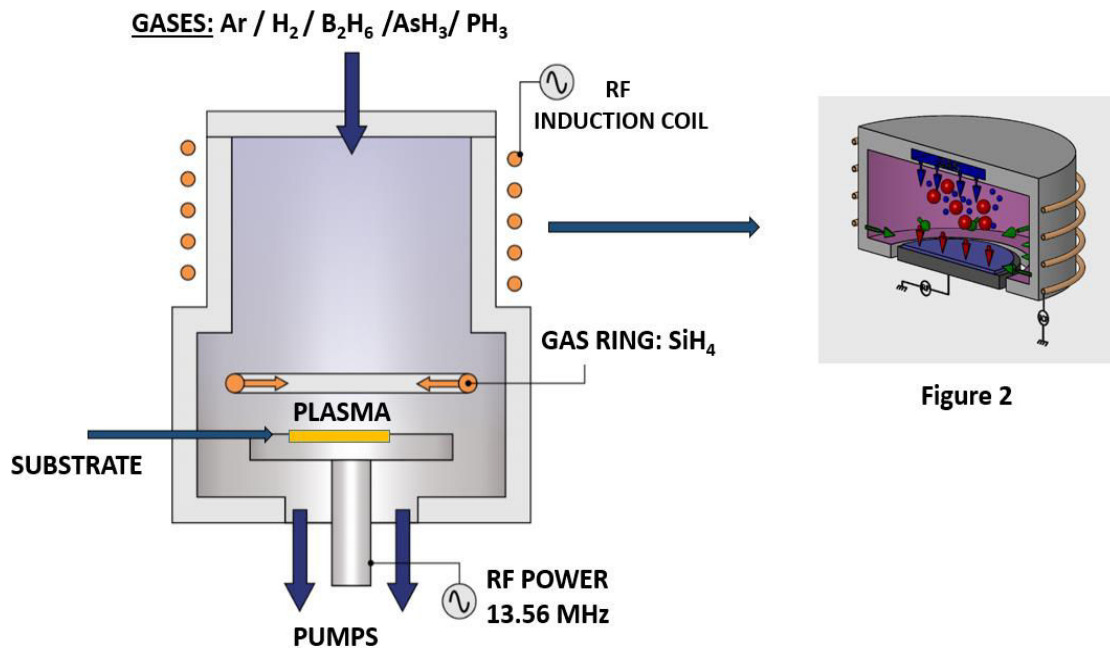


Figure 2.2. Schematics of high-density-plasma (HDP) chamber [4] and ICP-CVD reactor.

To summarize, Table 2.1 presents the main advantages of ICP-CVD technique over PECVD and some disadvantages.

ICP-CVD	
Advantages over PECVD	Main disadvantage
High density plasma Low deposition pressures Lower range of temperatures process Lower induced stress Good step coverage	High cost of equipment New technique in the laboratory - necessity to investigate optimum deposition conditions

Table 2.1. Advantages and disadvantages of ICP-CVD technique compared to PECVD.

3. Flexible devices with microcrystalline silicon

Microcrystalline silicon deposited by PECVD technique was widely investigated in the IETR. To achieve a good quality on these materials, there are several parameters that were deeply studied such as the temperature or the pressure used during the deposition process, the percentage of SiH_4 , H_2 or Ar in the gases dilution or the selected power. This semiconductor material was optimized during K. Kandoussi's thesis[1], fixing then the parameters that were used in the following research.

There are different devices fabricated with this material, however here we will introduced briefly those that were fabricated onto flexible substrate.

The first example of $\mu\text{c-Si}$ on a flexible substrate was realized during S. Janfaoui's thesis [5]. He has developed $\mu\text{c-Si}$ top-gate thin film transistor (TFT) on $5 \times 5 \text{ cm}^2$ sheets of PEN (Polyethylene naphthalene). In this work, the thickness of the sheets of PEN is $125 \mu\text{m}$ and it is encapsulated on both sides with 250 nm of Silicon Nitride. Over it, a layer composed of 100 nm thick undoped $\mu\text{c-Si}$ and 70 nm thick N doped $\mu\text{c-Si}$ is deposited. Here, the devices are characterized under static deformation with different curvature radii. They are bent under tensile and compressive stress. The main goal was to study the electrical and mechanical behaviors of these TFTs under mechanical stress. Figure 2.3 shows the architecture of the TFT used during this thesis.

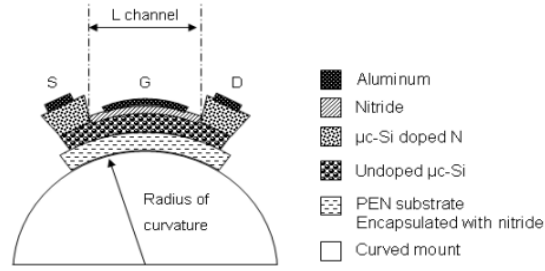


Figure 2.3. Schematic TFT developed in S. Janfaoui's thesis [5].

The following example of $\mu\text{c-Si}$ used with a flexible substrate at IETR, is extracted from Y. Kervran's thesis [6]. The design of the devices consists in Transmission Line Measure method (TLM) and a strain gauge matrix on a Kapton® substrate with different thicknesses of $125\ \mu\text{m}$ and $50\ \mu\text{m}$. The goal of this thesis was to investigate if $\mu\text{c-Si}$ has the ability to be used as a pressure sensor. The characterization test consists in submitting the devices to different curvature radii and to verify its sensitivity to the deformations. Figure 2.4 shows an example of the strain sensor used.

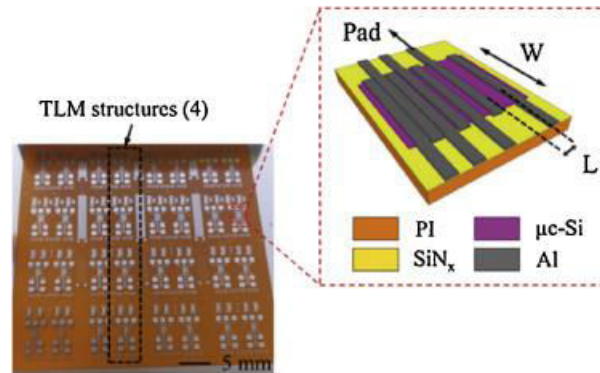


Figure 2.4. Schematic TLM structure developed during Y. Kervran's thesis [6].

Hence, taking into account these previous results of the laboratory where $\mu\text{c-Si}$ was used on a flexible substrate; our project is to submit our samples to a dynamic and continuous deformation, as this will allow us to verify the reliability of $\mu\text{c-Si}$ as a pressure sensor. Moreover, it will give us more information about the material's behavior especially during dynamic strain. It was then necessary to create a dynamic acquisition system and try to find a structure that responds fast and exhibits a linear response to strain deformations. For this, different possibilities have been studied, such as reducing the thickness of the substrate to $25\ \mu\text{m}$ or creating new designs to facilitate the recovery of the structure. All of this will be explained throughout this thesis.

4. Piezoresistive properties of N type $\mu\text{c-Si}$

To properly understand the piezoresistive properties of $\mu\text{c-Si}$, some concepts need to be introduced. Our sensors are based on piezoresistive effect and, as it was explained in Chapter 1, when a material is deformed by an applied mechanical stress, an electrical change is produced and the resistance value varies. As shown in formula (2.1), a change in the resistance value (R) can be produced by the change of the resistivity or by the geometry.

$$R = \rho \frac{L}{S} \quad (2.1)$$

Where (ρ) is the resistivity, (L) corresponds to the length and (S) is the surface area of the sensing material, $\mu\text{c-Si}$ in our case.

To quantify the sensitivity of the material to the applied mechanical stresses, the gauge factor (GF) is defined. As shown by the formula (2.2), it is formed by two components: the geometrical distribution ($1+2\nu$) and the variation of the resistivity in function of the strain ($(\Delta\rho/\rho)/\epsilon$), where ν is the Poisson's ratio, ρ the resistivity and ϵ the axial strain applied.

$$GF = \frac{\Delta R/R}{\epsilon} = (1 + 2\nu) + \frac{(\frac{\Delta\rho}{\rho})}{\epsilon} \quad (2.2)$$

For the metal strain gauge, the resistivity of the metal lines does not vary with the strain, therefore the equation (2.3) can be written as:

$$GF = \frac{\Delta R/R}{\epsilon} = (1 + 2\nu) \quad (2.3)$$

Normally, the Poisson's ratio value is between $0.3 < \nu < 0.5$, so that their GF is in the range $1.6 < GF < 2$ [7].

However, for semiconductor materials like silicon, both terms of the Formula (2.2) should be considered, which means that the values obtained for the gauge factors can be several orders of

magnitude higher than the metallic ones. Hence, it is important to understand well the second term of the equation, and especially how the resistivity is changing.

When a material is not stressed, it exhibits a constant resistivity, but when the structure is deformed by an external force, the lattice changes produce a change in the resistivity.

In the case of single crystalline silicon, it presents a diamond cubic lattice form described in Chapter 1. Generally, silicon is doped with impurities in order to increase its conductivity. Depending on the dopant used, this can be an electron donor or an electron acceptor.

When a semiconductor material is doped, it means that the band-gap is controlled by adding small impurities to the material. These impurities can change the electrical conductivity of the lattice and therefore vary the performance of the semiconductor. Depending on the majority carriers ratio, it exists two different kinds of extrinsic semiconductors, p-type (holes are the majority) and n-type (electrons are the majority).

Depending on the direction of the applied stress (tensile or compressive), the lattice structure is affected, generating a change in the carrier mobility (electrons and holes) through the lattice.

Hence, the mobility of the carriers affects the resistivity of the material, as expressed for example with n-type material in equation 2.4:

$$\rho = \frac{1}{n\mu q} \quad (2.4)$$

Where (μ) is the carrier mobility, (q) is the absolute value of the electronic charge, and (n) is the concentration of free carriers.

In cases of n-type materials, where most charge carriers are electrons, when a tensile strain is applied, the interatomic spacing of the lattice will increase and that generates an increase of the mobility and thus a decrease of the resistivity. When a compressive strain is applied, the interatomic spacing decreases, reducing the mobility and increasing the resistivity [8].

Hence, the sensitivity of silicon to the strain depends on its crystalline orientation with respect to the applied field and also on its type of dopant.

In our case, the material used is N- type and the gases used for doping are arsine and phosphine, because the (GF) factor is directly linked to the doping concentration [9].

5. Mechanical behavior of thin films

In order to obtain sensors with good reliability, it is important that the total structure has the ability to come back fast to the initial state. The mechanical behavior of the compound structure in thin film flexible electronics depends on several properties such as the Elastic or Young's Modulus, the hardness or the adhesion of the layers and the thickness of each part [10].

Nowadays, one of the main disadvantages of film thickness reduction in the fabrication process and handling come from the fragility of thin layers. However, during recent years, many remarkable advances in the technology of thin-film deposition and etching process technology have been achieved, such as new high-performance inorganic materials that can be combined with methods of printing and transfer of the structures, thereby improving the quality of the films as well as their adhesion to the substrate [11].

The understanding of the behavior of thin materials is necessary and the definition of parameters that help their classification is mandatory. Briefly, some basic concepts and definitions that need to be consider during the film selection to fabricate flexible devices are introduced.

- Young's Modulus: It measures the elastic properties of a solid material that is submitted to tension or compression in one direction. It is defined in formula 2.5 as the relationship between stress (force per unit area, σ , see equation 2.6) and strain (deformation in a solid due to the stress, ϵ , formula 2.7) of a material in the linear elasticity regime.

$$\text{Young Modulus (Y)} = \frac{\text{Stress}}{\text{Strain}} = \frac{\sigma}{\epsilon} \quad (2.5)$$

$$\text{Stress } (\sigma) = \frac{\text{Force(F)}}{\text{Area (A)}} \quad (2.6)$$

$$\text{Strain } (\epsilon) = \frac{\Delta L (\text{change in large})}{L (\text{original large})} \quad (2.7)$$

The Young's modulus should be constant for a given material. This parameter has a direct link with the elasticity and is also called Elastic Modulus (y). When a material presents high elastic modulus, it is classified as stiff material and if the elastic modulus is low, it is classified as compliant.

- Hooke's Law: it expresses mathematically the relationship between the stress and the strain, as illustrated Figure 2.5. It demonstrates that, when an elastic material stays inside the elastic stress region, the stress should be linearly proportional to the strain. Also, in this region, the loading is reversible. However, one time that the elastic limit has been overcome and the stress vs. strain curve starts to deviate from the linear region, the deformation of the material will be irreversible.

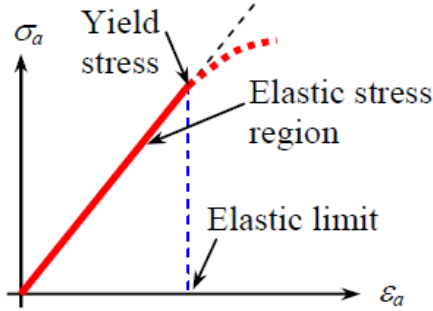


Figure 2.5. Stress (σ) vs. strain (ϵ) relation.

The mechanical behavior of thin films (f) on thin substrates (s) depends on the geometry, the Young's modulus (Y) and the thickness (d) of each part. In function of the two last parameters the behavior of substrate/film structure could be classified in:

- $Y_f \cdot d_f \ll Y_s \cdot d_s$. When the thickness and the Young's modulus of the deposited film are very low compared with the substrate ones, the substrate dominates and the film complies with it. The effect of the stress in the substrate is small and the film/substrate couple suffers from slight curves, even when the film is highly stressed.
- $Y_f \cdot d_f \gg Y_s \cdot d_s$. When the thickness and the Young's modulus of the substrate are very low compare to the film ones, the film dominates and the substrate complies with it.

In our case, the film dominates and the stress in the film creates a deformation on the film/substrate structure. The structure is bent with a radius of curvature R. This level of the curvature depends on the nature of the substrate, and especially on its thickness.

Film stress is usually calculated with Stoney's equation, which relates the Young's modulus of the substrate, the thickness of the film and of the substrate, and the radius of curvatures of pre- and post-process.

Stoney's relation.

The Stoney's relation is generally used to calculate the residual stress value for the linear, elastic region of the stress-strain curve. In the literature, there are different versions of this equation depending on the substrate type [12]. However, to apply this formula, all the versions should respect these two hypotheses:

- (a) Film stress can be evaluated with the final measure of the curvature of the substrate (or change of curvature, if this was not initially flat).
- (b) Results do not depend on the properties of the film, thus the measurement of the substrate curvature gives the current stress in the film.

Stoney's Formula is presented for the case where the substrate is stiff and the case where the substrate is compliant to the film.

- When the substrate is stiff and the film conforms to it ($Y_f \cdot d_f \ll Y_s \cdot d_s$). In this case, the stress in the substrate is smaller than in the film, so the substrate dominates, making that the stress arise in the film (σ_f) by formula 2.8 (a).

$$\sigma_f = \varepsilon_M Y_f^* \quad (2.8 \text{ a}) \quad R_o = \frac{Y_s^*}{6 \sigma_f} \frac{d_s^2}{d_f} \quad (2.8 \text{ b})$$

Where (ε_M) is the mismatch strain, and $Y_f^* = Y_f / (1 - \nu_f)$ where (Y_f^*) is the biaxial Young's modulus of the film, and (Y_f) is Young's modulus and (ν_f) is Poisson's ratio of the film. The stress in the substrate is smaller than the stress in the film making that substrate bends into a curvature radius (R_o) is given by formula 2.8 (b) where (d_f) corresponds to the film thickness, (d_s) is the substrate thickness, and Y_s^* is the biaxial Young's modulus of the substrate.

- When the substrate complies the film ($Y_f \cdot d_f \gg Y_s \cdot d_s$). In this case, the substrate bends into a roll. The substrate is considerably deformed and the curvature radius (R_o) can become very small. In our case, during the deposition process, the substrate is held with a rigid frame, so the substrate is flat and the stress in the film (σ_f) is given by formula 2.9 (a) where $Y_f^* = Y_f / (1 - \nu_f)$, is the biaxial Young's modulus of the film.

On this case, the stress in the film also depends on the thickness and Young's modulus of the substrate. The stress in the substrate is given by formula 2.9 (b), and as result, the

substrate will bend into a roll with a radius of curvature defined by the formula 2.9 (c), here \bar{Y} corresponds to the plane strain Young's modulus, $\bar{Y} = (1 + \nu^2)$

$$\sigma_f = \frac{\varepsilon_M Y_f^s}{1 + (Y_f^s d_f)/(Y_s^s d_s)} \quad (2.9 \text{ a})$$

$$\sigma_s = - \frac{\sigma_f d_f}{d_s} \quad (2.9 \text{ b})$$

$$R_o = \frac{(\bar{Y}_s d_s^2 - \bar{Y}_f d_f^2)^2 + 4 \bar{Y}_f \bar{Y}_s d_f d_s (d_f + d_{hs})^2}{6 \varepsilon_M (1 + \nu) \bar{Y}_f \bar{Y}_s d_f d_s (d_f + d_s)} \quad (2.9 \text{ c})$$

On Figure 2.6, can be observed, the normalized radius of curvature as a function of the film/substrate thickness ratio (d_f/d_s) [13]. The dashed lines represent the Stoney's formula 2.8 (b) for a stiff wafer ($Y_f d_f \ll Y_s d_s$) and the continuous or full lines are the response of a steel or Kapton® substrate when applying this formula 2.9 (c).

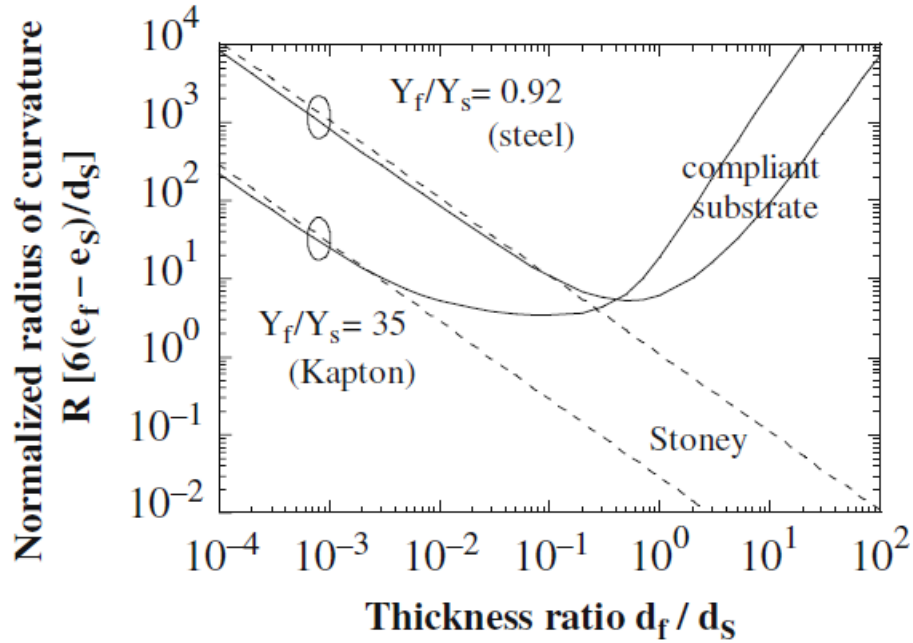


Figure 2.6. Normalized radius of curvature when the substrate compliant to the film [13].

6. Fabrication technology on thin film flexible devices

Traditionally, electronic devices are fabricated onto rigid substrates. However, the recent needs for devices that can be bent, rolled or stretched give rise to the flexible electronic. The reduction of the thickness in the different films generates some mechanical and electrical problems. In the following, the main manufacturing difficulties to perform thin film devices on flexible substrate will be introduced.

One of this problem comes from the thermal contraction of the substrate and the built-in stress of the films during and after the deposition step. This fact generates a curve and a change in the in-plane dimensions of the device.

Another common issue is the mismatch between the substrate and the deposited layers. This stress induces some problems like cracks or delamination in the layers. Usually, the stress on thin-film substrate appears during the depositions step, and is due to the difference between the thermal expansion/contraction coefficients or other reasons as the uptake and release of temperature or the humidity in the substrate.

To try to avoid the effects produced by the stress, flexible electronics devices need to be handled on a rigid carrier during the manufacturing process. After depositing the layers that will form the structure of the device, the flexible substrate needs to be flattened and temporarily bounded to a wafer or a glass until the end of the process. Hence, we try to minimize the cracks produced on the films and the mismatch during the alignment step due to stress-induced curvature [14].

The misalignment and the curvature increase when the substrate is thinner. These effects will increased by using a 25 μm thick Kapton® compared to a 50 μm thick ones. Different techniques such as an adhesive can be used to paste temporally the substrate. In all cases, the chosen method should be resistant to the chemicals used during all the process, should support temperature and be easy to remove at the end of the process, moreover as this last step could create some damages in the structure too. In order to minimize the effect of the cracks and the built-in stress introduced during film growth, various studies have been done and are described further. But first, the different kind of stress produced on thin-films and their classification in function of the origin are presented, in order to better understand how to minimize them.

6.1 Source of stress in thin film

A film's stress affects the performance, reliability and durability of the devices. This stress depends on the deposition conditions and the physical properties of the film and the substrate. Stress sources can be induced by differential thermal expansion or contraction of the films, depending also on the deposition method, by the release of humidity, or is influenced by the interface between film and substrate, etc. The origins of the stress could be of three types: intrinsic, thermal or epitaxial [15]. Often, intrinsic or thermal terms refer to residual stress. Moreover it exists the mechanical stresses that may appear in the layer and are due to bending or stretching of the structure. The following section focuses on the description of these concepts.

6.1.1 Thermal stress

Thermal stress is caused by differences in thermal expansion between the films and the substrate. It is usually caused by cooling from the deposition temperature to room temperature. The mismatch in the thermal expansion coefficients (CTE) of the substrate and the film can produce the film/substrate bending. This difference causes a contraction or expansion of the dominant material that extends to the rest of the structure. Figure 2.7 (a) shows the effect of the residual stress in the film due to compressive bending. Figure 2.7 (b) corresponds to the case where the CTE of the substrate is lower than the CTE of the film, producing a bending due to residual tensile stresses in the structure (compressive stress in the film). When we process with thick and stiff substrates, the effect of the thermal stress is hard to see with the naked eye, such as on a silicon wafer.

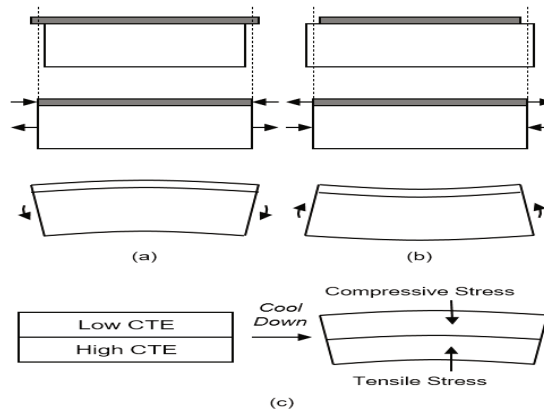


Figure 2.7: Film/substrate bending due to (a) compressive and (b) tensile residual stresses in the film and (c) due to mismatch of the coefficients of thermal expansion [16].

6.1.2 Intrinsic or growth stress

It is defined as the stresses distribution that is present in the film during the deposition / growth step when films are deposited under non-equilibrium plasma conditions. This stress does not come from the lattice or thermal mismatch strains, it arises during the deposition process because the films are not deposited under equilibrium conditions. It strongly depends on the deposition process conditions, the impurities, the materials involved, the grain boundaries or of the energy ions.

Figure 2.8 shows the effect of the energy ions on the film. When the plasma has low energy ions, the substrate suffers tensile stress. For the contrary, if the ions have high energy during the deposition the substrate suffers compressive stress. ICP-CVD machine could offer the possibility to control or decrease the stress induced in the films, due to the low energies ion.

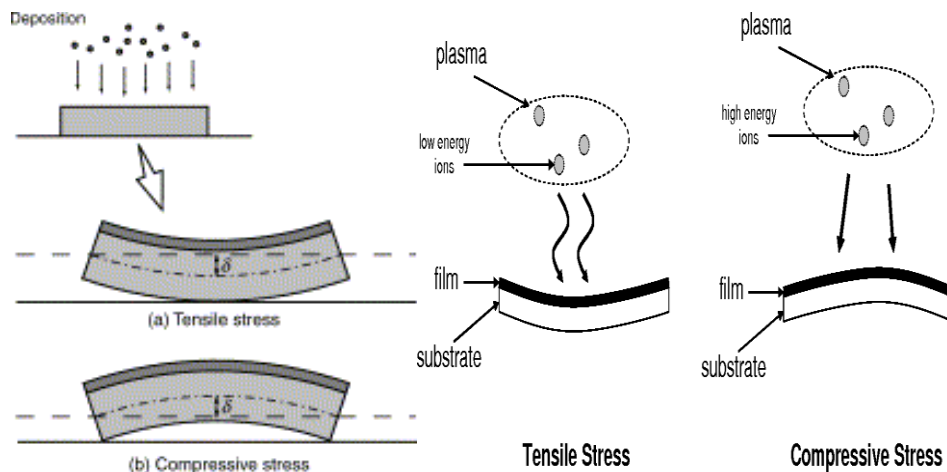


Figure 2.8. Effect of intrinsic stress on delamination [17], [18].

6.1.3 Epitaxial stress

Epitaxial misfit stresses arise when there are no coherent interfaces between films and substrates, i.e., when a mismatch exists in the crystal lattices in film and substrates. The strain misfit is calculated as:

$$\varepsilon = \frac{a_{\text{film}} - a_{\text{substrate}}}{a_{\text{substrate}}} \quad (2.10)$$

Where a_{film} and $a_{\text{substrate}}$ are the lattice parameters correspond to the film and the substrate. This effect is represented in Figure 2.9.

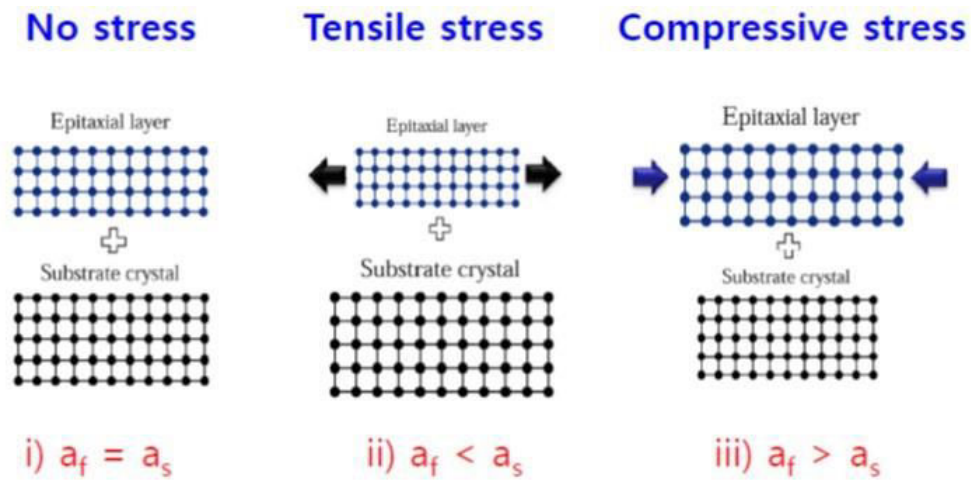


Figure 2.9. Effect of epitaxial stress [19].

6.1.4 Mechanical stress

Others external stresses may occur in the films due to mishandling. When the structure is extremely bent or stretched, it can create some damages, like debonding form by peeling or buckling. Figure 2.10 shows an example of this effect.

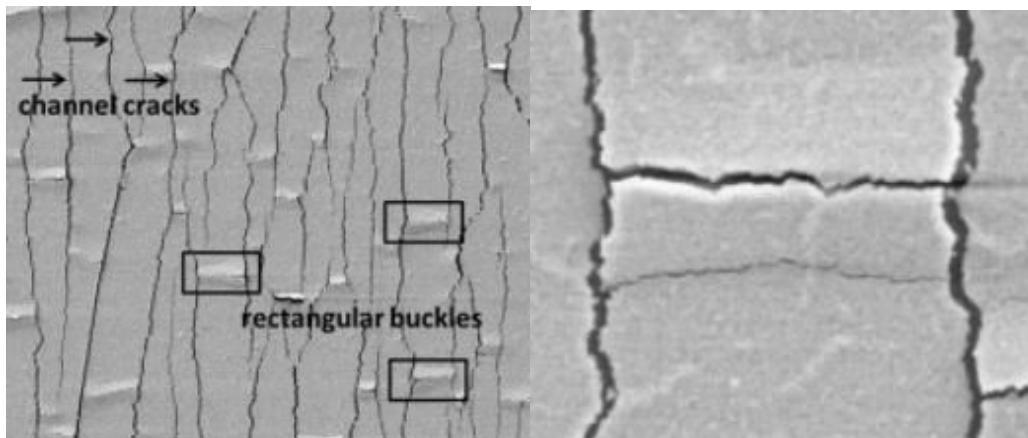


Figure 2.10. Effect due to mechanical stress [20].

6.2 Process and technological problems

In our case, during the manufacturing process, the main difficulties were associated with the low thickness of the substrate. The handling steps during etching, cleaning or deposition create some stress issues. As explained in the previous section, it is not surprising that after proceeding to a chemical vapor deposition (CVD) a deformation appears in the substrate. This residual stress results from the difference between the CTE of the film and the substrate (thermal stress) and from ion bombardment during plasma deposition (intrinsic stress) which damages the structure and induces misalignment in the following masking levels.

The first experiments had been first carried out on Kapton® substrate of 50 μm thick. The thickness of this substrate was not very low, for that reason, the problems due to the induced stress does not have a major effect on the global structure.

However, for the major experiments, the thickness of Kapton® is only 25 μm . Here, as show Figures 2.11 and 2.12 after $\mu\text{C-Si}$ deposition (100 nm), the global structure exhibited a roll-on deformation, causing cracks on the sensing material.

In the following sections, the fabrication process for our sensors is presented with the different approaches used to reduce stress-related problems.



Figure 2.11. Effect over Kapton® 25 μm after deposited the $\mu\text{C-Si}$ (100 nm).

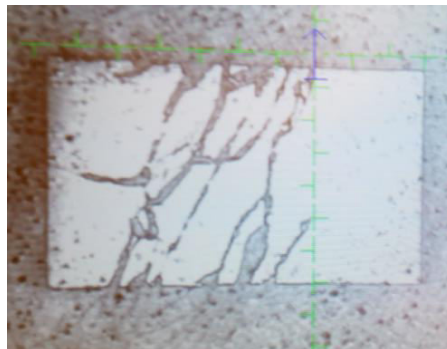


Figure 2.12. Cracks found in the $\mu\text{C-Si}$ after roll-on effect.

6.3 Approaches to reduce stress related problems

Generally, the equipment available in the laboratory is focused towards the fabrication process on rigid substrates such as glass or silicon wafers. However, some of them are also compatible with plastic substrates. In order to improve the performances and reliability of devices, it is necessary to develop an adapted fabrication process. This part presents the different problems found during the manufacturing steps, especially during deposition and lithography steps.

Moreover, it is dedicated to the treatment of stress problems and their consequences through three proposals: SiNx encapsulation, shadow mask and stability treatment of Kapton®.

The available photolithography machine holds the samples under vacuum in the backside. This equipment is perfect for rigid substrates. However, if the substrates have thickness lower than 50 μm , it needs to be temporarily fixed on a rigid one (silicon wafer or glass) to avoid deformations due to the vacuum. Sticking the samples also helps during all the fabrication process and reduces the possibility to damage the structures during handling. For all these reasons, in order to adapt our process, different ways to stick the substrate on a rigid support are investigated.

As a first option, the substrate is stuck on glass or wafer support with Kapton® adhesive, placed in the four corners of the sample. This option has the advantage to be easy and fast. However, the main problem found with this technique is the infiltration of water, solvents or acids during the fabrication process, as shown in Figure 2.13. Those liquids accumulate between the sample and the support. To avoid their absorption in the Kapton®, it is necessary to remove the tape and to dry it, fact that complicates the process and can induce some cracks in the layers.

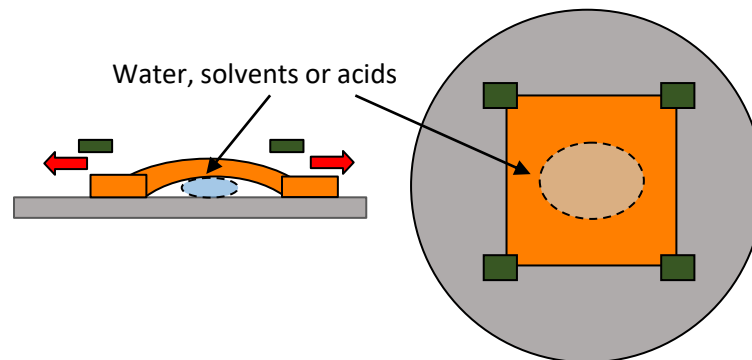


Figure 2.13. Issues of temporary bonding on silicon wafer.

The other solution, which has been selected, is to deposit by spin coating a thin layer of PDMS over a silicon wafer as shown Figure 2.14. PDMS layer allows to temporally stick the Kapton® substrate, which will be removed from the wafer only at the end of the process. To avoid the bubbles between Kapton® and PDMS, the sample is put under vacuum during 30 minutes.

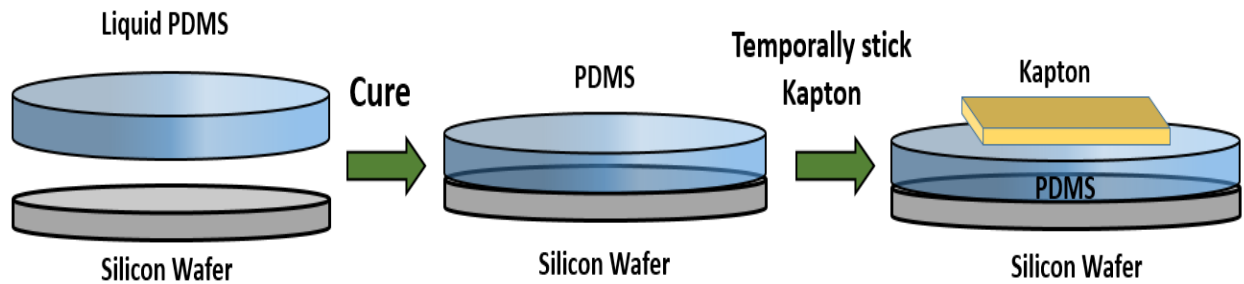


Figure 2.14. Support for temporary bonding using a thin film of PDMS.

6.4 Solutions for mechanical stresses introduced during fabrication

As it was commented before, strains/stresses in the film/substrate structure can create some cracks or delamination in the film and curling or buckling problems in the substrate, thus changing the in-plane dimensions of the structure. All these factors affect devices performance and create some alignment problems between the different layers that constitute the device. The thinner the thickness of the substrate is, the greater the curvature and the misalignment are [21]. For that reason, a proposal has been studied to try to compensate all these effects.

6.4.1 Effect of SiN_x encapsulating layers

Following literature recommendations [14], a silicon nitride layer can be used to try to compensate the tensile built-in stress between Kapton® substrate and $\mu\text{c-Si}$ after deposition. Silicon nitride can be used for several goals, as to protect the substrate against chemical processes or to provide adhesion of the other layers. But it can also be used to balance the stress-induced curvature [14]. Figure 2.15 shows a clear example of how is it possible to balance the ion induced stress on Kapton® by adjusting the RF deposition power on PECVD machine from 5 to 25 W. The deposition temperature used for this experiment was 150 °C [14].

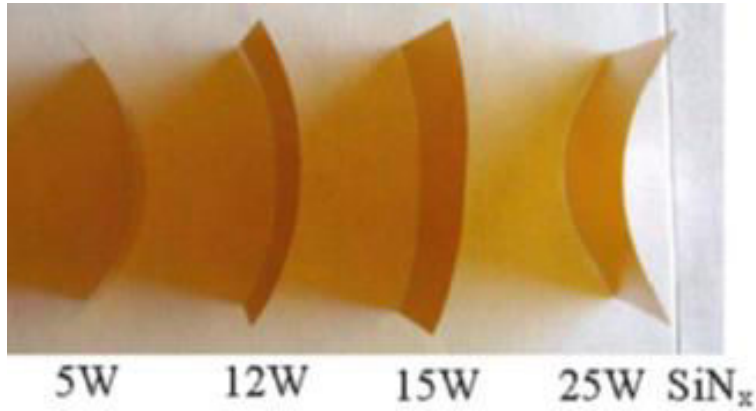


Figure 2.15. Curvature induced by stress in films of (b) SiNx [14].

In our case, the parameters selected to use silicon nitride as encapsulation layer were the same ones used for previous thesis in IETR laboratory [22][23] and are presented in Table 2.2.

Parameters	Power (W)	Pressure (mbar)	Distance electrodes (cm)	Temperature (T °C)	SiH ₄ (sccm)	N ₂ (sccm)	H ₂ (sccm)
SiNx	50	0.3	4.5	150	1	100	5

Table 2.2. Conditions used for SiNx layer.

In order to balance the induced stress after $\mu\text{c-Si}$ deposition and see if silicon nitride layer has some effect on the devices performance, three different structures are compared (Figure 2.16):

- $\mu\text{c-Si}$ was deposited directly on the Kapton® substrate.
- Encapsulation of Kapton® on one side of the substrate with SiNx (50 nm).
- Encapsulation of Kapton® substrate on both sides using SiNx (50 nm).

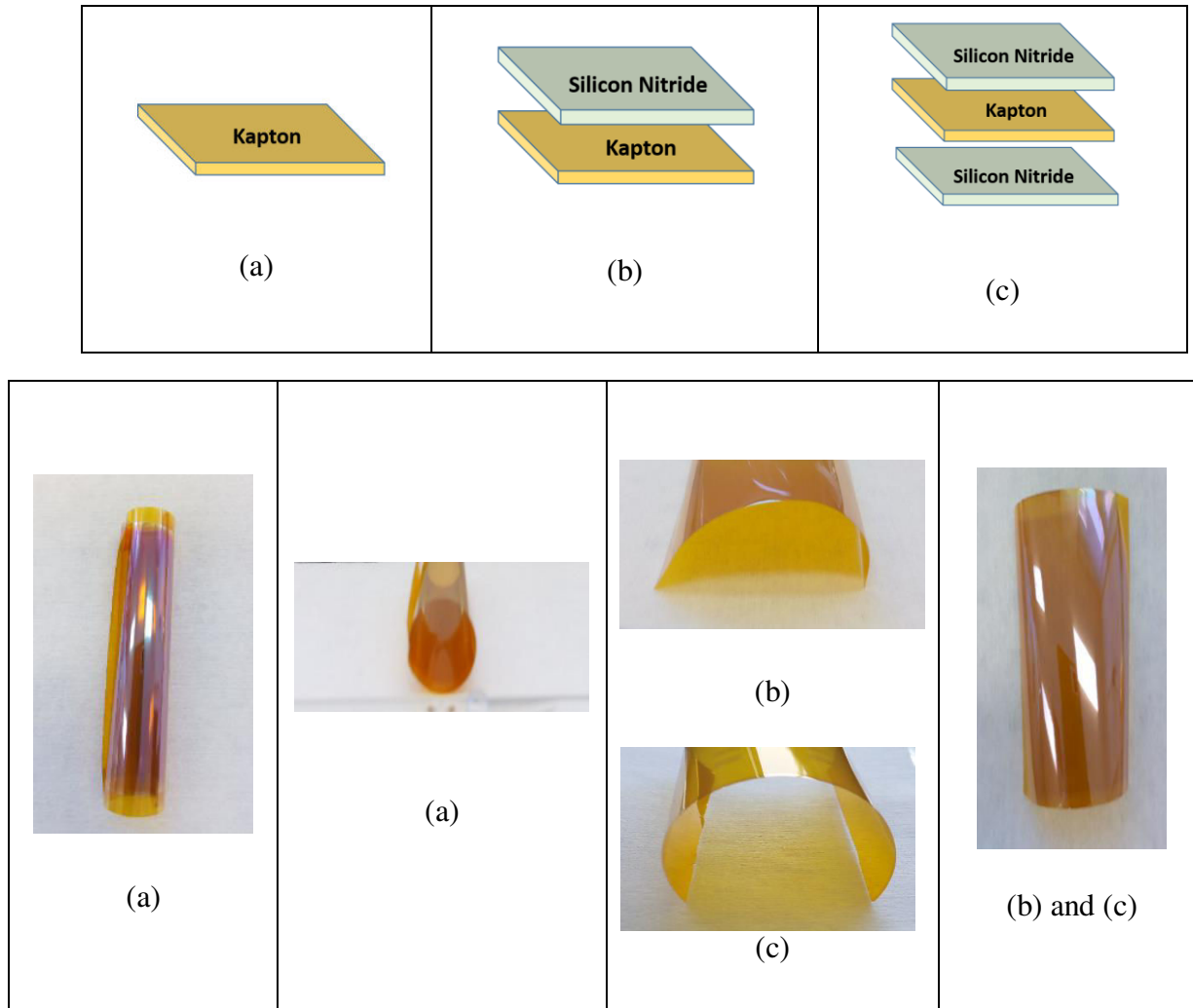


Figure 2.16. Structure for 25 μm of Kapton® after $\mu\text{c-Si}$ deposition a) without any encapsulation layer b) and c) with SiN_x layer encapsulation.

Figure 2.16 shows the visual effect of Kapton® substrate when $\mu\text{c-Si}$ is directly deposited on it (a) and when encapsulation of the Kapton® is performed before deposition of $\mu\text{c-Si}$ (b) and (c). It can be observed that with an encapsulation of SiN_x , the curvature due to the induced stress is considerably reduced. However, when Kapton® is encapsulated on one side (b) and on both side (c), the induced-stress curvature seems to be the same.

Therefore, it can be concluded that using SiN_x as an encapsulation layer allows to control the induced-stress after $\mu\text{c-Si}$ deposition, and should reduce the cracks and the misalignment problems.

The next step is to verify if this encapsulation has some effect on the electrical performance of the sensor. To do this, when the fabrication process is finished, the sensors are measured before and after being submitted to different deformations. Figure 2.17 shows the three different structures and the shift produced in the resistance before and after deformation. The calculation of the shift value is shown on equation 2.11, where (R_f) is the final resistance value after been submitted to different strain deformations and (R_0) corresponds to the initial value, in flat position:

$$\text{Shift} = \frac{\Delta R}{R_0} (\%) = \frac{R_f - R_0}{R_0} (\%) \quad (2.11)$$

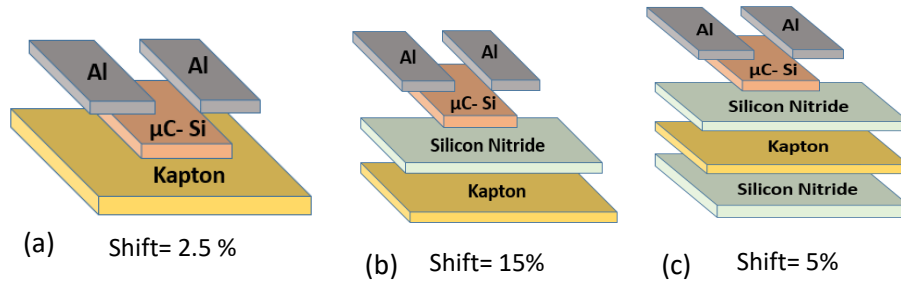


Figure 2.17. Structures and values of resistances shiftiness before and after bending.

The shiftiness produced on the samples with silicon nitride layer is higher, (b) and (c). This fact can be explained by the very high Elastic Modulus of Silicon Nitride, which is around 183 GPa. This hardness induces some cracks during deformation, these cracks are expanded to the rest of the structure making that the value of the resistance changes after deformations.

SiNx layer cannot then be a good option to balance the induced stress after $\mu\text{C-Si}$ deposition, because SiNx layer produces a strong shift of the resistance value after deformations and worse the reliability of the devices.

6.4.2 Effect of reducing the area of $\mu\text{C-Si}$ deposition

One other method developed to reduce the induced stress was to reduce the deposition area of $\mu\text{C-Si}$. To do that, a shadow mask has been designed with ANSYS software. During the design, attention was paid to the phenomenon of the step coverage in CVD deposition, [24], [25], so the

dimensions of the squares of these mask are bigger than the area of $\mu\text{C-Si}$ that will be used for the devices.

Figure 2.18 shows the dimensions of the squares are $3 \times 4 \text{ cm}^2$. The maximum area of $\mu\text{C-Si}$ used for transmission line measurement (TLM) mask is $1 \times 1 \text{ cm}^2$ and the minimum value is $1 \times 0.0125 \text{ cm}^2$. (Those masks will be further fully described).

Figure 2.18 (b) shows the theoretical effect of the step coverage of CVD films [26] and Figure 2.18 (c) shows an example of this effect in one of our sample using the designed shadow mask.

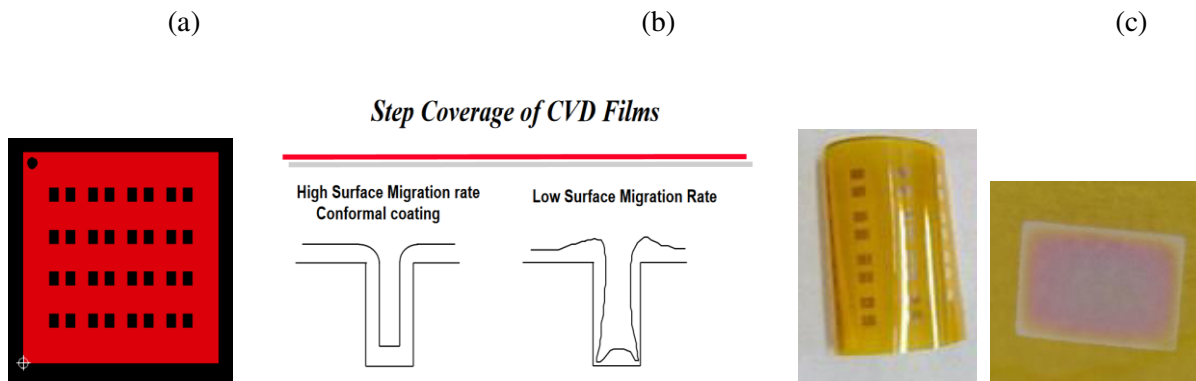


Figure 2.18. (a) Shadow mask design to reduce the area of $\mu\text{C-Si}$ deposition for TLM mask (b) Effect step coverage of CVD films. (c) Sample using the shadow mask for $\mu\text{C-Si}$ deposition and the effect of the step coverage.

6.4.3 Dimensional stability of Kapton® and shrinking

Despite the use of all the techniques commented previously, the induced curvature has been reduced but it still remains a little bit.

In the $25 \mu\text{m}$ Dupont Kapton® polyimide datasheet [27], it is written that the substrate suffers for a shrinking during and after the first exposure to high temperature. This effect is permanent and, once the substrate has been exposed, Kapton® follows the normal values of the linear expansion thermal coefficient.

For this reason, to set the substrate to its stable form, a pre-bake process is realized after the cleaning procedure. The substrate is baked in the hot plate during 30 min at 150°C . This bake is also important to remove solvents residuals. After the prebake process, the substrate is ready for fabrication steps.

Figure 2.19 (a) shows the induced curvature of Kapton® substrate using a shadow mask during $\mu\text{c-Si}$ deposition and Figure 2.19 (b) shows the effect on the sample when the pre-bake process is done before $\mu\text{c-Si}$.

Hence, by combining this pre-bake and the shadow mask, the residual stress is strongly reduced. This dimensional stability of the substrate is important to avoid alignment problems or delamination of the layers, thus improving the electrical and mechanical performance of the devices.



Figure 2.19. Effect curvature induced (a) after $\mu\text{c-Si}$ using a shadow mask (b) pre-bake substrate before $\mu\text{c-Si}$ using a shadow mask.

7. Conclusion

In this chapter, it was introduced the working principle of the different deposition techniques available in the laboratory to deposit $\mu\text{c-Si}$, ICP-CVD and PECVD.

In addition, the main problems that arise to work with thin flexible substrate. To minimize the problems associated with the low thickness of the structure it was studied several proposals. However, the best results were obtained when the sample is temporally bonding to a silicon wafer covered by a thin layer of PDMS during the fabrication process, reducing the alignment problems and handling.

Moreover, to try to maintain the dimensional stability of Kapton® we baked it at 150 °C for 30 minutes before the $\mu\text{c-Si}$ deposition. Silicon nitride layer used during the first devices to balance the stress is removed because arises some instability and stress problems when the structure is bend. To minimize the stress that comes from $\mu\text{c-Si}$, this is deposited using a shadow mask.

8. References

- [1] K. Kandoussi, 'Procédé de fabrication à $T < 200^{\circ}\text{C}$ de transistors en couches minces de silicium microcristallin déposé par PECVD en mélange $\text{SiH}_4\text{-H}_2\text{-Ar}$,' thesis, Rennes 1, 2007.
- [2] A. Shah, E. Vallat-Sauvain, P. Torres, J. Meier, U. Kroll, C. Hof, C. Droz, M. Goerlitzer, N. Wyrsh, M. Vanecek, 'Intrinsic microcrystalline silicon ($\mu\text{c-Si:H}$) deposited by VHF-GD (very high frequency-glow discharge): a new material for photovoltaics and optoelectronics,' Mater. Sci. Eng. B, vol. 69–70, pp. 219–226, 2000.
- [3] W. J. Soppe, C. Devilee, M. Geusebroek, J. Löffler, and H.-J. Muffler, 'The effect of argon dilution on deposition of microcrystalline silicon by microwave plasma enhanced chemical vapor deposition,' Thin Solid Films, vol. 515, no. 19, pp. 7490–7494, 2007.
- [4] Datasheet 'Inductively Coupled Plasma - Chemical Vapor Deposition (ICP-CVD),' Corial, 20-Dec-2016.
- [5] S. Janfaoui, 'Électronique CMOS en silicium microcristallin sur substrat flexible transparent,' thesis, Rennes 1, 2012.
- [6] Y. Kervran, 'Cartographie d'un champ de pression induit par l'occlusion dentaire,' thesis, Rennes 1, 2016.
- [7] S. Middelhoek and S. A. Audet, 'Silicon Sensors', published by Academic Press, Ltd, London, vol. 2, pp. 376, 1989, <https://infoscience.epfl.ch/record/24206>.
- [8] C. Herring and E. Vogt, 'Transport and Deformation-Potential Theory for Many-Valley Semiconductors with Anisotropic Scattering,' Phys. Rev., vol. 101, no. 3, pp. 944–961, 1956.
- [9] C. Liu, Foundations of MEMS. Upper Saddle River, N.J: Prentice Hall, vol. 2, pp. 231-238, 2012.
- [10] M. Gunda, P. Kumar, and M. Katiyar, 'Review of Mechanical Characterization Techniques for Thin Films Used in Flexible Electronics,' Crit. Rev. Solid State Mater. Sci., vol. 42, pp. 1–24, 2016.
- [11] R. Reuss, G. Raupp, and B. Gnade, 'Special issue on advanced flexible electronics for sensing applications [Scanning the Issue],' Proc. IEEE, vol. 103, pp. 491–496, 2015.
- [12] A. Mézin, 'Coating internal stress measurement through the curvature method: A geometry-based criterion delimiting the relevance of Stoney's formula,' Surf. Coat. Technol. - Surf. Coat. Tech., vol. 200, pp. 5259–5267, 2006.

- [13] H. Gleskova, I.-C. Cheng, S. Wagner, and Z. Suo, 'Mechanical Theory of the Film-on-Substrate-Foil Structure: Curvature and Overlay Alignment in Amorphous Silicon Thin-Film Devices Fabricated on Free-Standing Foil Substrates,' in *Flexible Electronics: Materials and Applications*, W. S. Wong and A. Salleo, Eds. Boston, MA: Springer US, pp. 29–51 2009,
- [14] I.-C. Cheng, A. Kattamis, K. Long, J. C. Sturm, and S. Wagner, 'Stress control for overlay registration in a-Si:H TFTs on flexible organic-polymer-foil substrates,' *J. Soc. Inf. Disp.*, vol. 13, no. 7, pp. 563–568, 2005.
- [15] Thin Film Mechanics, J. Vlassak, DEAS Harvard University, 2004, presentation.pdf.
- [16] K.-B. Kim, Y. Oh, and Y.-H. Song, 'Simulation of residual stress and its impact on a poly-silicon channel for three-dimensional, stacked, vertical-NAND flash memories,' *J. Korean Phys. Soc.*, vol. 70, pp. 1041–1048, 2017.
- [17] T. Kitamura, H. Hirakata, and T. Itsuji, 'Effect of residual stress on delamination from interface edge between nano-films,' *Eng. Fract. Mech.*, vol. 70, no. 15, pp. 2089–2101, 2003.
- [18] S. Pillay, 'Development of a Dense Diffusion Barrier Layer for Thin Film Solar Cells,' vol 7409, pp. 237-244, 2009.
- [19] 'Epitaxy (epitaxial growth,)', <https://depletionregion.tistory.com/116>.
- [20] F. Toth, F. G. Rammerstorfer, M. J. Cordill, and F. D. Fischer, 'Detailed modelling of delamination buckling of thin films under global tension,' *Acta Mater.*, vol. 61, no. 7, pp. 2425–2433, 2013.
- [21] W.-Y. Chang, T.-H. Fang, and Y.-C. Lin, 'Physical characteristics of polyimide films for flexible sensors,' *Appl. Phys. A*, vol. 92, no. 3, pp. 693-701, 2008.
- [22] K. Belarbi, K. Kandoussi, N. Coulon, C. Simon, R. Cherfi, A. Fedala, T. Mohammed-Brahim 'Stability of Microcrystalline Silicon TFTs,' *ECS Trans.*, vol. 16, no. 9, pp. 121–129, 2008.
- [23] K. Kandoussi, A. Gaillard, C. Simon, N. Coulon, T. Pier, and T. Mohammed-Brahim, Improved microcrystalline silicon TFTs,' *J. Non-Cryst. Solids*, vol. 352, no. 9, pp. 1728–1731, 2006.
- [24] P. Moni, A. Al-Obeidi, and K. Gleason, 'Vapor deposition routes to conformal polymer thin films' *Beilstein J. Nanotechnol.*, vol. 8, p. 723 (12pp.), 2017.
- [25] 'Thin Polymer Films with High Step Coverage in Microtrenches by Initiated CVD - Baxamusa - 2008 - Chemical Vapor Deposition - Wiley Online Library.'

- [26] 'Step Coverage of CVD Films - Thin Film Materials Processing - Lecture Slides - Docsity.' <https://www.docsity.com/en/step-coverage-of-cvd-films-thin-film-materials-processing-lecture-slides/285243/>.
- [27] Datasheet 'KAPTON substrate .pdf.'
<https://www.dupont.com/content/dam/dupont/products-and-services/membranes-and-films/polyimide-films/documents/DEC-Kapton-HN-datasheet.pdf>

CHAPTER 3 - Transmission Line Measurements (TLM) and static deformations

1. Introduction

The aim of this chapter is to investigate the piezoresistive properties of microcrystalline silicon and its sensitivity to different mechanical deformations.

First, we will introduce the method used to characterize this material. It is based on the principle of Transmission Line Measurements (TLM). In this section, the parameters extracted with this method will be theoretically explained with special attention to the specific contact resistivity. This parameter has become very important in recent times due to the sharp reduction in the size of devices, where the value of parasitic resistances must be significantly low.

Following, the mask used and the fabrication process of these devices will also be described.

The deposition of $\mu\text{c-Si}$ was carried out using two different techniques: PECVD (Plasma-enhanced chemical vapour deposition) and ICP-CVD (Inductively Coupled Plasma Chemical Vapour Deposition). According to both techniques, the results obtained were divided in two parts. The first consists in studying the classic parameters of the TLM structure such as the specific contact resistivity (ρ_c), the sheet resistance (R_{SH}) or a mapping of uniformity of the resistivity. The second part presents the sensitivity of the microcrystalline silicon as a deformation sensor, when this material is subjected to different bending radii.

2. Transmission Line measurement (TLM)

The Transmission Line Measurement or TLM method is one of the most common approaches to calculate the specific contact resistance, the transfer length and the sheet resistance (R_{SH}) of the semiconductor.

This method was introduced by Shockley in 1964 [1] and, as shown in Figure 3.1, consists of measuring parallel resistances separated by contacts with variable spacing or length (d_1 , d_2 , d_3 , d_4). The values of the resistances obtained are plotted in a linear regression, from which all the parameters mentioned above can be extracted.

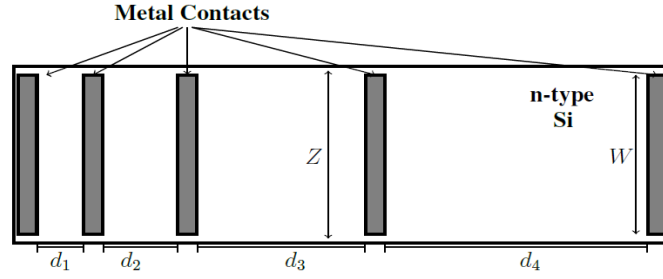


Figure 3.1. Top view of Transmission Line structure [2].

2.1 Parameters extraction

Figure 3.2 shows a scheme of a resistance measurement and a horizontal view of the TLM structure.

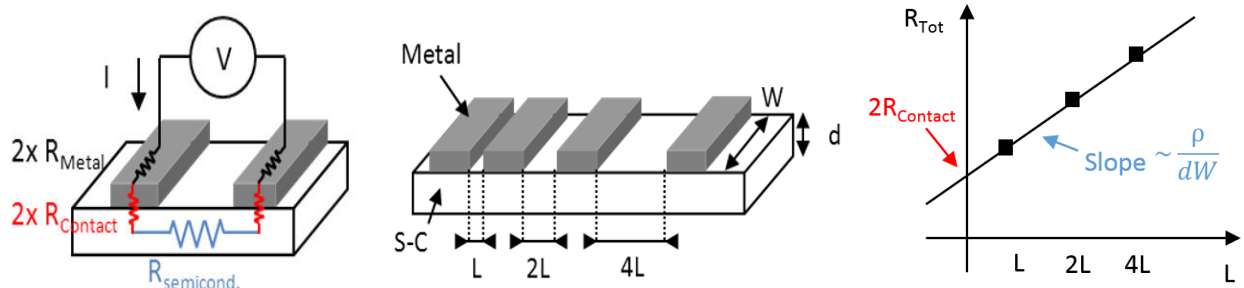


Figure 3.2. Transmission Line Measurement Geometry (TLM) [3].

I-V measurements were realized between each adjacent contact, and they are plotted as a function of the total resistance (R_{Tot}) and the contact spacing (L). It allows to extract some parameters such as the semiconductor resistance ($R_{Semicond.}$) or the contact resistance (R_c). The total resistance can then be expressed by the formula (3.1):

$$R_{Tot} = R_{Semicond.} + 2R_{Contact} + 2R_{Metal} \longrightarrow R_{Tot} = \frac{\rho}{dW} L + 2R_{Contact} \quad (3.1)$$

Where $R_{Semicond.}$ corresponds to the semiconductor resistance and it is obtained from the slope of the linear regression of the curve in Figure 3.2. R_{Metal} , is the metal resistance and generally can be considered as negligible. $R_{Contact}$, is the contact resistance in the metal-semiconductor junction. This parameter can be extracted for the intersection between the coordinate axis (Figure 3.2). It has a direct impact in the device's performance, and for this reason, must have a small value.

From the contact resistance, the contact resistivity can be extracted, however this parameter depends on the contact area size. For that reason, to make a comparison independent of its size, in

the literature [2], the contact resistance is employed and can be obtained directly through TLM model.

Firstly, to better understand what happens in the junction between the metal-semiconductor and how this affects the devices performance, it is necessary to understand how the current flows through the interfaces.

The contact between metal and semiconductor can be classified mainly in ohmic contact or Schottky barrier contact.

- Schottky contacts (also called barrier or rectifiers) have important applications such as Schottky diodes or MESFET transistors. The main characteristic of the rectifier contacts is that they allow working at high speeds, and therefore, they are widely used in high frequency applications such as switches. They are so used as power rectifier diodes since they easily dissipate heat through the metallic contact.
- The ohmic contacts refer to the contact in which there is no rectifying effect. Basically, an ohmic contact is a low resistance joint that provides conduction in both directions between the metal and the semiconductor. Ideally, the current through the ohmic contact is a linear function of the applied potential. The quality of an ohmic contact is evaluated by determining specific contact resistance that will be defined later.

Theoretically, to achieve an ohmic contact between a metal and N-type semiconductor, the condition to be fulfilled is that the working function of the metal is less than the semiconductor (or higher if it is a P-type semiconductor). Unfortunately, there are very few combinations able to achieve this requirement. Therefore, the most common alternative is to use heavily doped semiconductor. However, depending on the semiconductor doping level, there are three main conduction mechanisms between metal and semiconductor, shown in Figure 3.3. The thermionic emission presents a low doping impurities concentration and its I-V curve behaves such a Schottky barrier (a); the thermionic-field emission has a medium doping level of impurities (b) and the field emission, here the junction metal semiconductor is heavily doped obtaining an ohmic contact as shows the graphic (c).

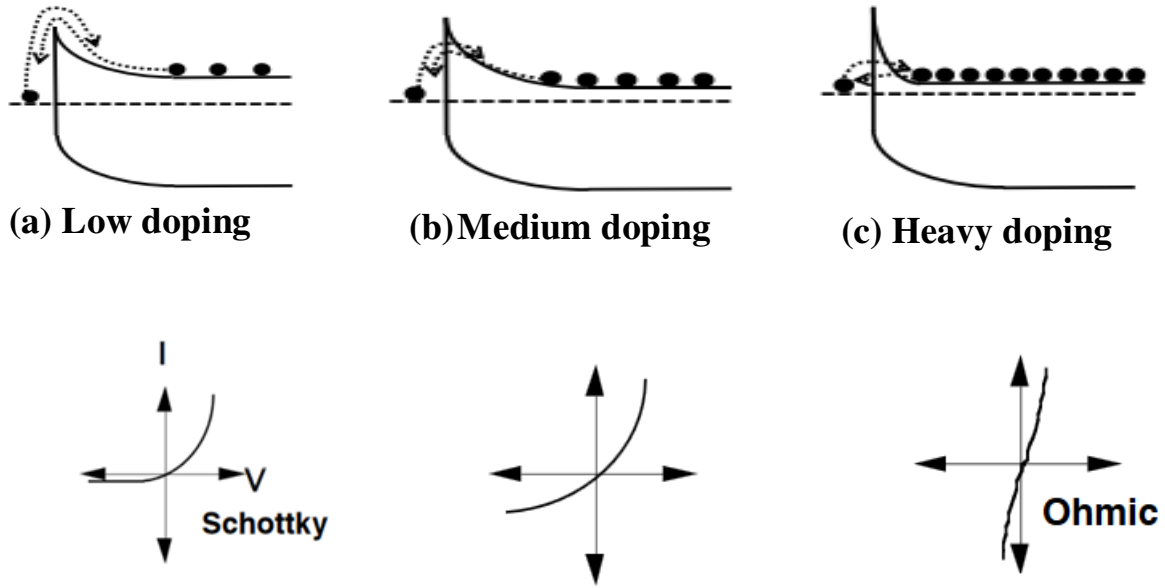


Figure 3.3: Conduction mechanisms for metal/n-type semiconductor contacts as a function of the barrier height and width. (a) Thermionic emission; (b) thermionic-field emission; (c) field emission [2].

2.2 The specific contact resistivity

The specific contact resistivity is used to determine the quality of the metal-semiconductor junction and is a useful parameter to qualify an ohmic contact.

As explained before, an ohmic contact allows that the charge flow easily in both directions between the metal and the semiconductor [4]. In this case, the value of the contact resistance should be negligible and the I-V curve obtained should be linear or quasi-linear.

There are other methods to measure the specific contact resistivity (ρ_c) such as Cross Bridge Kevin Resistance (CBKR) [5]. However, our work focuses on the transmission line measurement method (TLM).

This method allows to calculate the specific contact resistivity (ρ_c) by means of the transfer length (L_T), which is defined as the length at which more than 60% of the current flows through the contacts.

Figure 3.4 shows what occurs really in the electrodes. Here the current density over its conduction area is not uniform and it enters the contact from the top, the bottom and the front.

However, to simplify the calculus and because almost all of the current enters through a path under the contact, we only consider that the current density enters from the bottom.

According to the level of the specific contact resistivity, two different cases can be described. For very small values of ρ_c , shown Figure 3.5 (a), only the edge of the contact area is used in the conduction t, and for high values of ρ_c , as shown Figure 3.5 (b), a large area of the contact is used for the conduction.

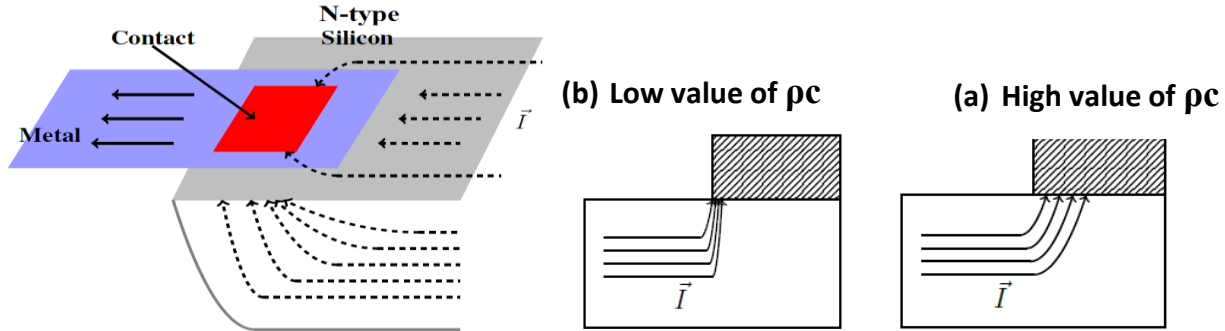


Figure 3.4. Current flows [2]

Figure 3.5. Current lines in function of the ρ_c electrodes [2]

Formula 3.2 (a) or (b) is used to calculate the value of the specific contact resistance (ρ_c), where (R_{SH}) is the sheet resistance of the underlying layer, (R_C) corresponds to the contact resistance and (W) is the width. The value of the transfer length, (L_T) can be extracted from the graph in Figure 3.6. It corresponds to the half value of the x-axis interception between the total resistance (R_T) and the spacing distances (d).

$$L_T = \sqrt{\frac{\rho_c}{R_{SH}}} \quad (3.2 \text{ a})$$

$$L_T = \frac{\rho_c}{R_C \times W} \quad (3.2 \text{ b})$$

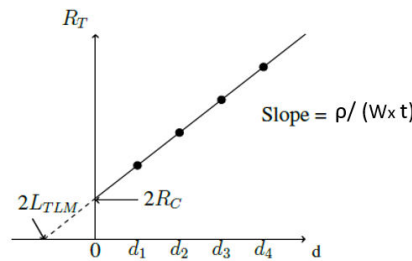


Figure 3.6. Graphic used to extract TLM parameters [2].

Moreover in our case, TLM devices are used to evaluate the uniformity of the resistivity at different points of the sample. In the second part of this chapter, this structure is used to evaluate the sensibility of $\mu\text{c-Si}$ to different deformations.

3. Mask design and fabrication process

The designed mask used to perform TLM devices is shown in Figure 3.7. Its surface area is $5 \times 5 \text{ cm}^2$, there are four columns with four different width values ($W = 125, 1000, 500, 250 \mu\text{m}$).

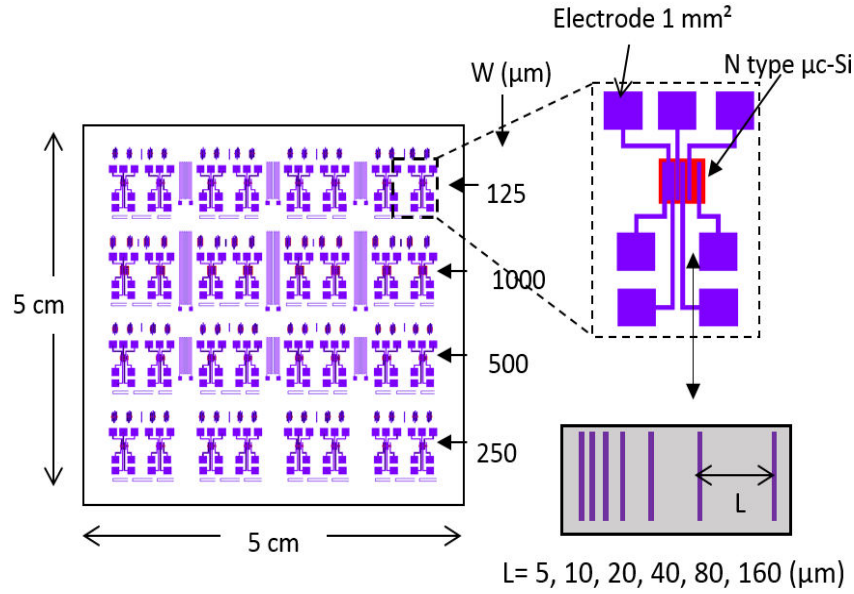


Figure 3.7. TLM design used in our devices [3].

Each line presents the same dimensions and each TLM structure is formed by 6 resistances with different lengths ($L = 5, 10, 20, 40, 80, 160 \mu\text{m}$). The design contains 24 resistances with different dimensions. Next, it is presented the steps followed during the fabrication process for TLM devices.

4. TLM Device Manufacturing Process

Here is described the fabrication process of TLM devices. The first step is to cut the Kapton® substrate foil in a $6 \times 6 \text{ cm}^2$ square. The substrate's trimmed area is 1 cm^2 bigger than the mask size ($5 \times 5 \text{ cm}^2$) to help us in the manipulation process. The next steps in the fabrication process are described below and are represented on Figure 3.8.

1) Substrate cleaning and post treatment, Figure 3.8 (a):

Kapton® substrate is cleaned with acetone and alcohol to remove small particles pollution, this process is repeated as often as necessary. Once the substrate is dry, it is necessary to bake it in the hot plate during 30 min at 150 °C. As explained in Chapter 2, this step is necessary due to Kapton® shrink after the first deposition at high temperature.

2) Silicon nitride (50 nm) as an encapsulation layer Figure 3.8 (b):

This layer was only used in the first devices manufactured, as written in Chapter 2. Indeed, its effect on the mechanical behaviour of the structure leads to the creation of cracks. However, the influence of the nitride layer on the electrical behaviour of the device will be analysed in this chapter. Its removal will help to improve the performance and flexibility of our sensors.

3) $\mu\text{c-Si}$ (100 nm) as sensing material Figure 3.8 (c1):

This material is deposited by two different techniques, PECVD and ICP-CVD. The $\mu\text{c-Si}$ areas of the devices are defined by photolithography and etching.

Photolithography: this step consists in spin coating a thin layer of photoresist S1818 over $\mu\text{c-Si}$ layer. After that, it is baked at 100 °C to dry the photoresist. A mask is used to flash the sample that will define the device's pattern. The photoresist is then developed to verify if the shape is well defined.

Etching: in the case of $\mu\text{c-Si}$, etching is made by using a Reactive Ion Etching (RIE) reactor. The gas used to realize the etching is SF_6 , Figure 3.8 (c2).

4) Electrodes, Figure 3.8 (d1):

Aluminium is the material selected to fabricate the electrodes. It is deposited through evaporation by Joule effect and the thickness of the layer is 150 nm. The photolithography step is then realized.

For aluminium, a wet etching consisting in immersing the sample into solution of phosphoric acid (H_3PO_4) at a temperature of 50 °C, Figure 3.8(d2) is achieved.

5) Annealing:

This is realized during 2 hour under nitrogen at 180 °C. The annealing step is necessary to improve the junction between the metal and the semiconductor enhancing the bonding between the two materials.

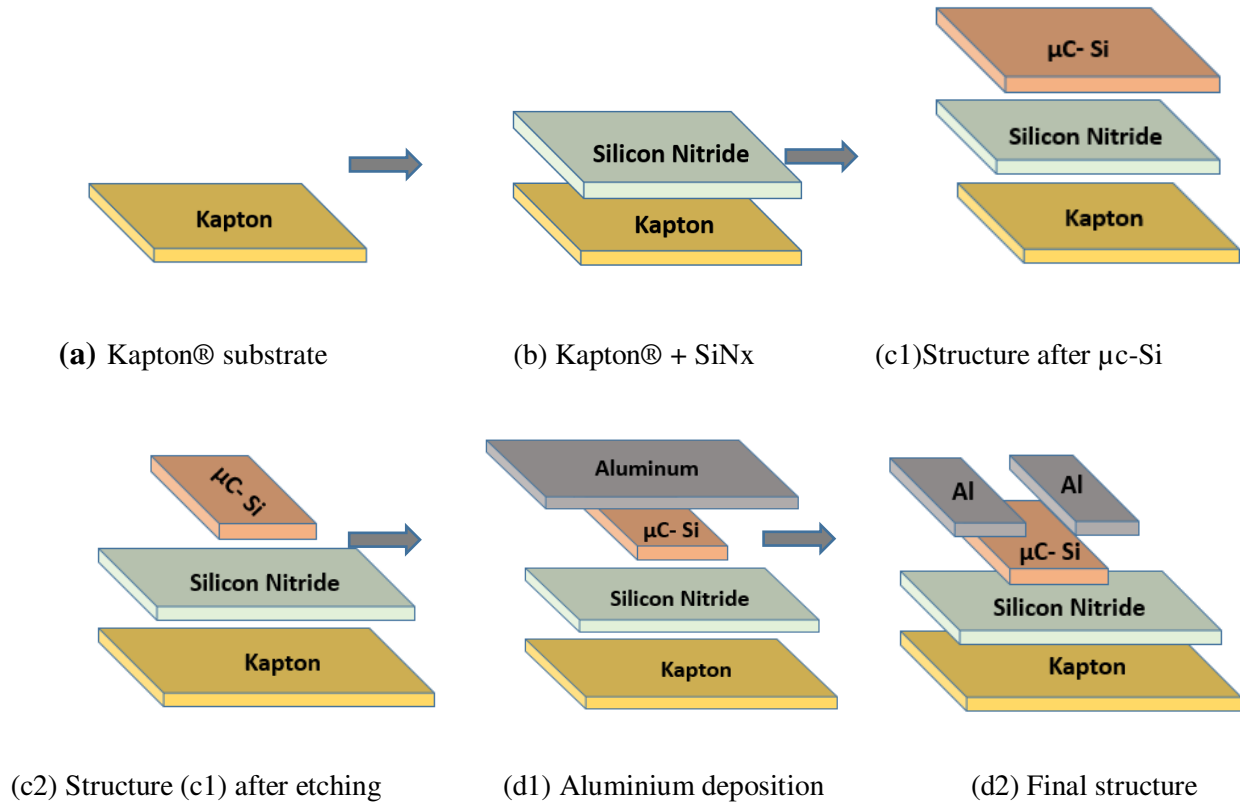


Figure 3.8. Fabrication process in TLM devices.

5. Raman spectroscopy

In order to compare the quality of microcrystalline silicon deposited by two different methods (PECVD, ICP-CVD), Raman spectroscopy can be performed to analyse this material and determine its crystallinity [6].

As described in Chapter 1, microcrystalline silicon is a mixture of crystalline zones separated by grain boundaries (amorphous zone). By using Raman spectrometry, it is possible to know the crystallization level also called crystalline fraction ($f_{C\%}$)

The spectrum allows us to obtain more information about the chemical bonds between radicals.

The spectrum is formed by the convolution of 3 Gaussian contributions as shown in Figure 3.9:

- Amorphous phase of silicon (C_{am}): integral of Raman intensity centered at 480 cm^{-1} .

- It exists an intermediate phase (C_{int}) that corresponds to a defective crystalline phase with a center at about 510 cm^{-1} . It highlights the presence of joints of crystalline grains and crystallites of dimensions less than ten nanometers [7].
- Crystalline phase of silicon (C_{mono}): A narrow Gaussian centered at about 520 cm^{-1} , corresponding to the crystalline phase of the material. The position and width of the Gaussian depends on the grain size and stress in the material. [8] [9] [10].

Once this deconvolution has been achieved, the calculation of the area under each curve allows to calculate the crystalline fraction using the formula 3.3.

$$(fc \%) = \frac{C_{mono} + C_{int}}{C_{mono} + C_{int} + C_{am}} \quad (3.3)$$

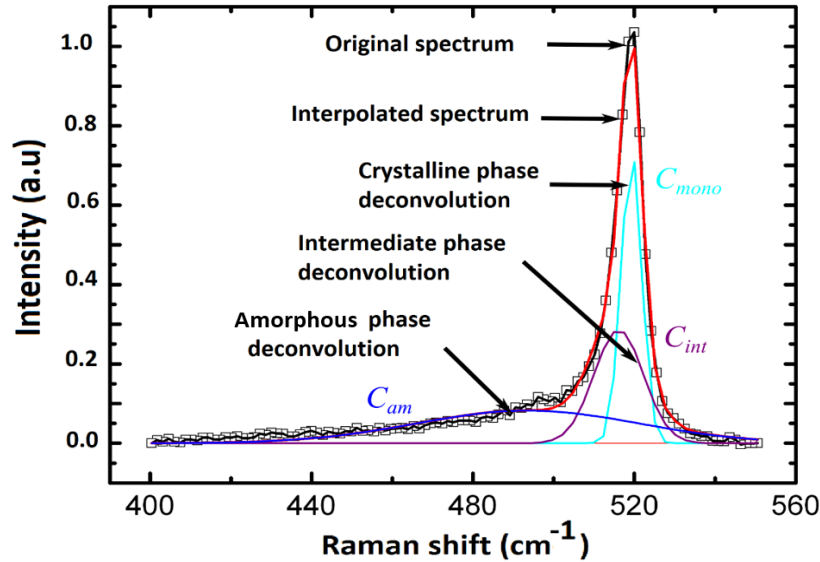


Figure 3.9. Raman spectrum deconvolution for three curves [11].

6. Results obtained with TLM technology

TLM structures are used for different objectives, so the results will be separated in two sections.

Firstly, the results obtained with both deposition techniques (PECVD, ICP-CVD) will be shown. The parameters extracted such as the specific contact resistivity (ρ_c), the sheet resistance (R_{SH}) and a mapping of resistivity uniformity are presented. The calculations are based on the theory shown in section 2 of this chapter.

Secondly, these structures are used to calculate the sensitivity of N-type microcrystalline versus different deformations. TLM design is not usually dedicated to this goal, but we will use them to study the piezoresistive properties of the sensing material.

6.1 TLM parameters for N-type $\mu\text{c-Si}$ deposited by PECVD technique

This is the historical technique used in the laboratory to deposit N-type microcrystalline silicon at low temperature. The deposition parameters of this technique has been improved during K. Kandousi's thesis [12] and are shown in Table 3.1.

Temperature	Power	Pressure	Gases	
T=165 °C	15 W	0.9 mbar	Ar = 75 sccm	SiH ₄ = 1.5 sccm
			H ₂ = 75 sccm	AsH ₃ = 10 sccm

Table 3.1. N-type doped $\mu\text{c-Si}$ conditions for the deposition in PECVD machine.

In order to learn how to work with 25 μm thick flexible substrate and to compare the results with previously ones obtained in the IETR [3], with substrates thickness of 50 μm , three different structures were tested.

- I. Kapton® (50 μm) + SiNx (50 nm) + N-type $\mu\text{c-Si}$ (100 nm)
- II. Kapton® (25 μm) + SiNx (50 nm) + N-type $\mu\text{c-Si}$ (100 nm)
- III. Kapton® (25 μm) + N-type $\mu\text{c-Si}$ (100 nm)

The thickness of the structure is reduced gradually; first the thickness of the substrate from 50 μm (I) to 25 μm (II) and then silicon nitride layer is eliminated (II to III). Reducing the thickness the flexibility should be improved and this is important to the targeted application of this thesis.

Table 3.2 shows the values obtained with TLM structures for ρ_c and R_{SH} , L_T , R_c . The dimensions selected for width (W) are shown in Table 3.2 and the lengths are variable ($L = 5, 10, 20, 40, 80, 160 \mu\text{m}$). For the structure with a higher thickness substrate (50 μm) of Kapton® (I), it was used $W = 500 \mu\text{m}$ because it was the only structure still available on this substrate's thickness. The width (W) selected for the rest of the structures correspond to $W = 1000 \mu\text{m}$.

	(I) W= 500 μm	(II) W= 1000 μm	(III) W= 1000 μm
	Kapton® (50 μm)+SiNx (50 nm)+ $\mu\text{C-Si}$ (100 nm)	Kapton® (25 μm)+SiNx (50 nm)+ $\mu\text{C-Si}$ (100 nm)	Kapton® (25 μm)+ $\mu\text{C-Si}$ (100 nm)
R_{SH} (Ω)	13 k Ω	13 k Ω	16 k Ω
R_c (Ω)	94 Ω	59 Ω	32 Ω
L_T (μm)	3.6 μm	4.5 μm	2 μm
ρ_c (Ωcm^2)	1.7×10^{-3}	2.6×10^{-3}	6.4×10^{-4}

Table 3.2. Values obtained on TLM devices deposited by PECVD technique.

By observing the values of Table 3.2, we realized that when the thickness of the structure is reduced, the values of the contact resistance (R_c) is also reduced. To explain this fact, we decided to compare first the influence of the Kapton® thickness (50 μm versus 25 μm), and then the effect of the silicon nitride layer.

1) Kapton® substrate thickness effect:

We can compare the structures I) and II) where the only difference is the thickness of the substrate. Our first option was to investigate if the topography of the substrate has some influence on the conductivity.

Other researchers have investigated the effect of substrate material during PECVD deposition and the possible alteration during the film growth due to micro topographical features [13].

W.Y. Chang [14] has investigated the physical characteristics of polyimide films for flexible sensor by using AFM measurement in the x-y plane on a surface of $5 \times 5 \mu\text{m}^2$. He demonstrates that the average surface roughness (R_a), shown on Table 3.3 for both thickness are very similar. Therefore it is discarded that the roughness of Kapton's surface has some influence on this. Moreover, in the literature, we can find other studies that follow our theory comparing the roughness of different substrates before and after deposition. For example, Amirzada concludes that the nature of the substrate does not affect the final value of the surface roughness [15].

Thickness (μm)	Ra (nm)
25	10.3
50	13.8

Table 3.3. Topography study of Kapton® film.

2) Removal of the silicon nitride layer:

The Young's modulus value for silicon nitride layer is around 183 GPa [16]. For μc-Si, it is about 80 GPa [17]. This value makes that the hardness of SiN_x is bigger than μc-Si. Cracks appear more often in this case, and that can increase the value of the contact resistance (R_c), as shown in Table 3.3. Removing the nitride layer results in a decrease in contact resistance (R_c) and transfer length (T_L). Moreover, by removing the nitride layer, the hardness of the structure thickness is reduced and some problems between the layers such as delamination or stress cracks in the thin film are also reduced. These problems affect the conduction between metal-semiconductor and can degrade contact junction.

Moreover, to analyse the uniformity of the deposition, a mapping of the resistivity in different points of the sample was achieved. To perform this, 8 resistances with L= 40 μm and W= 1000 μm have been measured on each layer. The resistivity have been extracted from the following formula 3.4:

$$R = \frac{\rho}{W_x t} L \Rightarrow \rho = \frac{R_x W_x t}{L} \quad (\Omega \text{cm}) \quad (3.4)$$

Table 3.4 shows the results and Figure 3.11 the values obtained for the resistivity and its corresponding standard deviation.

	Mapping resistivity		
	Kapton® (50 μm)+SiN _x (50 nm)+μC-Si (100 nm)	Kapton® (25 μm)+SiN _x (50 nm)+μC-Si (100 nm)	Kapton® (25 μm)+ μC-Si (100 nm)
ρ (Ωcm)	0.132 ± 0.0021	0.137 ± 0.0112	0.139 ± 0.029

Table 3.4. Mapping of resistivity and it standard deviation using PECVD deposition

Analyzing the values in Figure 3.10, it can be noticed that general resistivity is the same only uniformity decreases as a function of the thickness of the overall structure. Indeed, during the $\mu\text{C-Si}$ deposition process, substrates with lower thickness show a higher induced curvature after the deposition process. This curve generates cracks in different zones, which modify the resistivity value and increase the non-uniformity of the sample, generating larger values in the standard deviation. In fact manipulation of a thin substrate with a more or less stressed deposit $\mu\text{-Si}$ above is much trickier which could explain the higher density of defect.

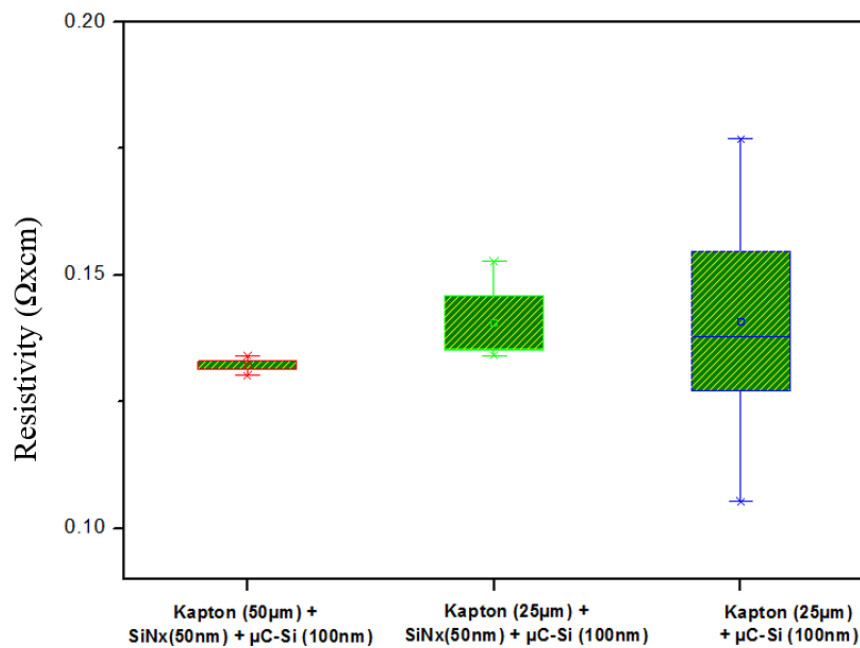


Figure 3.10. Representation of the resistivity mapping and its standard deviation on PECVD deposition.

Therefore to sum up this part where it was studied mainly the interest of SiN_x layer and the effect of Kapton® thickness, it can be concluded that R_{SH} value is independent of the use of Silicon Nitride layer and the thickness of the substrate. However, it affects other parameters measured such as the value of the contact resistance (R_c) or the uniformity of the resistivity. The lower result obtained for the contact resistance (R_c) corresponds to the structure without SiN_x layer, this can be due to Silicon nitride layer has higher hardness than $\mu\text{C-Si}$ for that reason it is used to control its induced stress however, this hardness could produce some issues such as delamination

or stress cracks that affect the conduction junction between metal-semiconductor and increment the contact resistance value.

The standard deviation in the uniformity of the deposition increase when the thickness of the structure is reduced, it can come from the difficulty of handling during the fabrication process.

6.2 TLM parameters for N-type $\mu\text{c-Si}$ deposited by ICP-CVD technique

As it was explained in Chapter 2, ICP-CVD is a plasma technic where the plasma is induced by an antenna which allows to deposit without RF and bias voltage also at a lower pressure and higher density of plasma due to the high power of the energy of the ICP plasma. Such as it is a new technique in the laboratory, it is necessary to study which parameters are the most appropriate to develop our sensors. To do that, the different key parameters that we decided to change are:

- The nature of dopant (AsH_3 or PH_3) and its concentration (20 sccm/10 sccm/5 sccm)
- The adjunction of small RF bias by pulsing (400 ms every 4 s) or RF bias without pulsing
- ICP power corresponds to (LF power); it was tested applying it in a continues mode at 600 W or by small pulse between 600 W to 900 W (400 ms every 4 s)

Several conditions are summarized in Table 3.5.

SAMPLE 1	SAMPLE 2	SAMPLE 3	SAMPLE 4	SAMPLE 5
20 PH_3 RF 0 W LF 600 W	20 PH_3 RF 0 W LF pulse 600-900 W	20 PH_3 RF 40 W LF 600 W	20 PH_3 RF pulse 0-40 W LF 600 W	20 AsH_3 RF pulse 0-40 W LF 600 W
SAMPLE 6	SAMPLE 7	SAMPLE 8	SAMPLE 9	SAMPLE 10
20 AsH_3 RF 0 W LF 600 W	5 PH_3 RF 0 W LF 600 W	10 PH_3 RF 0 W LF 600 W	10 PH_3 RF pulse 0-40 W LF 600 W	10 AsH_3 RF pulse 0-40 W LF 600 W

Table 3.5. ICP-CVD conditions. All samples proceed from SiH_4 precursor with Ar and H_2 ambience.

In the same way that for PECVD, the calculus of the specific contact resistivity (ρ_c), sheet resistance (R_{SH}), the transfer length (L_T) and the contact resistance (R_c) have been done with the method described in section 2. The values obtained are presented in Table 3.6.

	S1	S2	S3	S4	S5
R_{SH} (kΩ)	16 k Ω	15 k Ω	15 k Ω	5.8 k Ω	27 k Ω
R_c (Ω)	133 Ω	15 Ω	86 Ω	29 Ω	45 Ω
R_c/R_{SH} (Ω %)	0.83	0.1	0.57	0.5	0.167
L_T (μm)	8 μm	0.9 μm	6 μm	5 μm	1.8 μm
ρ_c (Ωxcm^2)	1.07×10^{-2}	1.4×10^{-4}	5.2×10^{-3}	1.5×10^{-3}	8.1×10^{-4}

	S6	S7	S8	S9	S10
R_{SH} (kΩ)	26 k Ω	67 k Ω	18 k Ω	8 k Ω	23 k Ω
R_c (Ω)	74 Ω	1.7 k Ω	51 Ω	25 Ω	356 Ω
R_c/R_{SH} (Ω %)	0.285	2.54	0.283	0.313	1.55
L_T (μm)	3 μm	3.4 μm	2.5 μm	4.3 μm	8.2 μm
ρ_c (Ωxcm^2)	2.2×10^{-3}	5.8×10^{-2}	1.3×10^{-3}	1.1×10^{-3}	2.8×10^{-2}

Table 3.6. Values obtained on TLM devices deposited by ICP-CVD technique.

The sheet resistance depends on the resistivity and the thickness of the layer, observing Table 3.6, their values are higher with Arsine as doping gas than when the sample is doped with Phosphine.

In order to organize these results, it was decided to represent them in the Figure 3.11, in which appear the values of the resistivity of specific contact as a function of the transfer length (since this parameter defines the length from which more than 60% of the current enters in the contacts). The ratios R_c/R_{SH} are also presented on this figure, and represent the percentage of the contact resistance over the sheet resistance.

Here it can be observed that as the L_T value increases; the ratios R_c/R_{SH} also increase. This is logical, because, as it was explained in previous sections, for small values of the contact resistivity ρ_c , that the current enters quickly in the contact, leading to a small value of the R_c/R_{SH} . Therefore these two parameters increase in proportion with L_T value.

The unique value that presents a relatively low value of transfer length L_T , 3.4 μm , and higher specific contact resistance corresponds to Sample 7, this can be due to it's the unique condition that uses a low concentration of doping gas, PH_3 5 sccm. This sample will be studied later to see

if it also present different values than the rest of the conditions for the resistivity or the sensitivity.

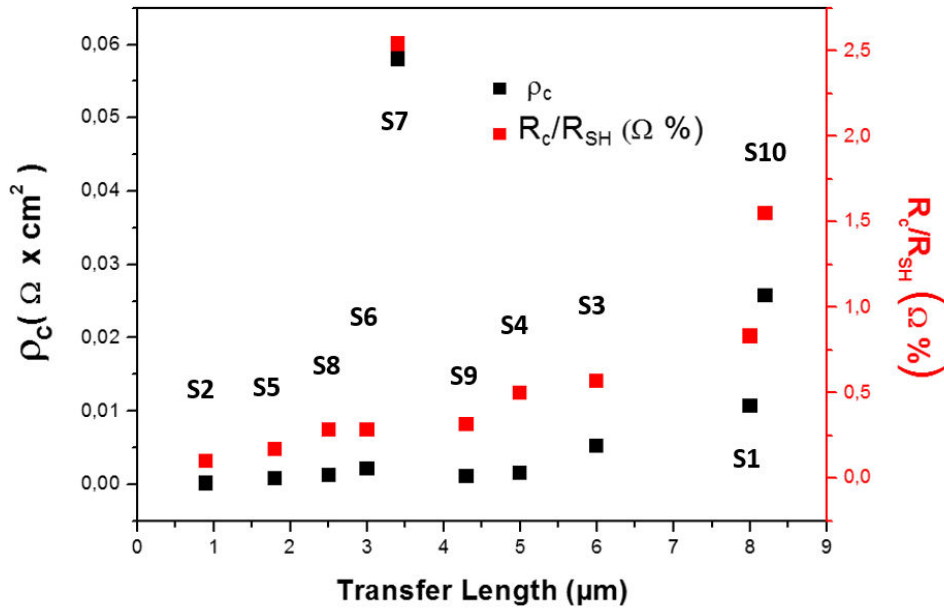


Figure 3.11. ICP-CVD results of it specific contact resistance (ρ_c) and R_c/R_{SH} in function of its transfer length (L_T).

Now some relevant cases can be commented of the Figure 3.11:

- S2 is the sample with the lowest values, this is normal because LF power pulses are used, and this effect should increase the crystallinity and therefore the conductivity making smaller the values for L_T , ρ_c and R_c/R_{SH} .
- It was also observed that for the same doping gas flow rate (AsH_3 or PH_3), when pulses are applied in RF power (samples 4 versus samples 1 and 3 and sample 5 versus sample 6), the values of the specific contact resistivity are lower, for the samples where RF power pulse is applied. Figure 3.12 shows an example of this. Moreover, to verify if the grain size is bigger when pulses are applied in the RF power, the crystallinity fraction ($f_c\%$), measured on these samples, was calculated from Raman spectroscopy measurement. Table 3.7 shows the values obtained.

	(S4) 20 PH ₃ RF pulse 0-40 W	(S3) 20 PH ₃ RF 40 W	(S1) 20 PH ₃ RF 0 W
Crystallinity fraction	79.82 %	72.8 %	71.4 %

	(S5) 20 AsH ₃ RF pulse 0-40 W	(S6) 20 AsH ₃ RF 0 W
Crystallinity fraction	66.4 %	64.4 %

Table 3.7 Results obtained for the crystallinity fraction ($f_c\%$).

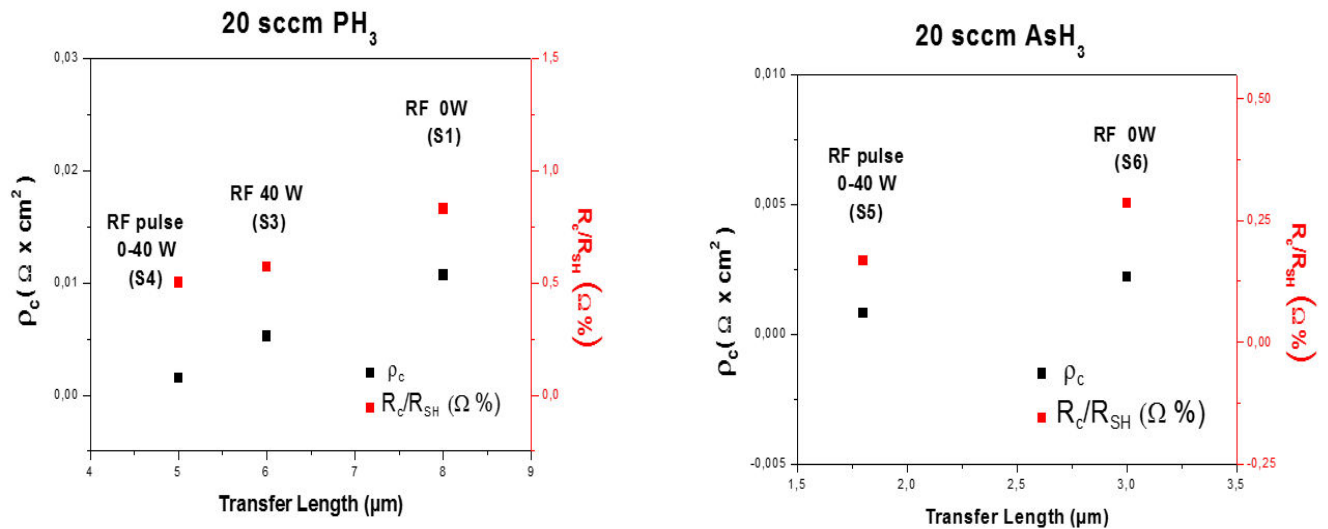


Figure 3.12. Effect on specific contact resistance (ρ_c) and R_c/R_{sh} when it is applied pulses in RF power.

Therefore, in the results of the crystallinity fraction presented in Table 3.7, it is interesting to observe that applying small pulses on RF power is more efficient than a continuous bias to obtain higher crystallinity fraction and lower transfer length value (L_T). Moreover when we select Phosphine as doping gas, it leads to higher crystallinity than Arsine and the impact of RF bias on As incorporation seems negligible, this fact was also noticed during high temperature deposition by LPCVD at 700 °C [18]. However, it is important to comment that RF pulse adjunction leads to

a strong increase of the layer stress which could induce sticking issue on Kapton® such as trouble of pilling.

To verify this and see the uniformity, it was performed a mapping of the resistivity. As it was demonstrated for the samples deposited by PECVD technique, when the thickness of the substrate is reduced, the standard deviation of the results obtained increases. However, to improve our skills in the manipulation of thin substrates that will be used in the devices for dynamic measurement in Chapter 4, all the samples were performed with low thickness substrate. Table 3.8 shows the values obtained for the resistivity mapping for all the samples. Figure 3.13 shows these values sorted in increasing order according to their resistivity.

Mapping resistivity					
	S1	S2	S3	S4	S5
ρ ($\Omega\text{xc}\text{m}$)	0.165 ± 0.0228	0.154 ± 0.0153	0.143 ± 0.0538	0.108 ± 0.0533	0.289 ± 0.0238
	S6	S7	S8	S9	S10
ρ ($\Omega\text{xc}\text{m}$)	0.273 ± 0.0413	0.668 ± 0.0447	0.170 ± 0.0151	0.083 ± 0.008	0.226 ± 0.0083

Table 3.8. Mapping of resistivity and it standard deviation using ICP-CVD deposition.

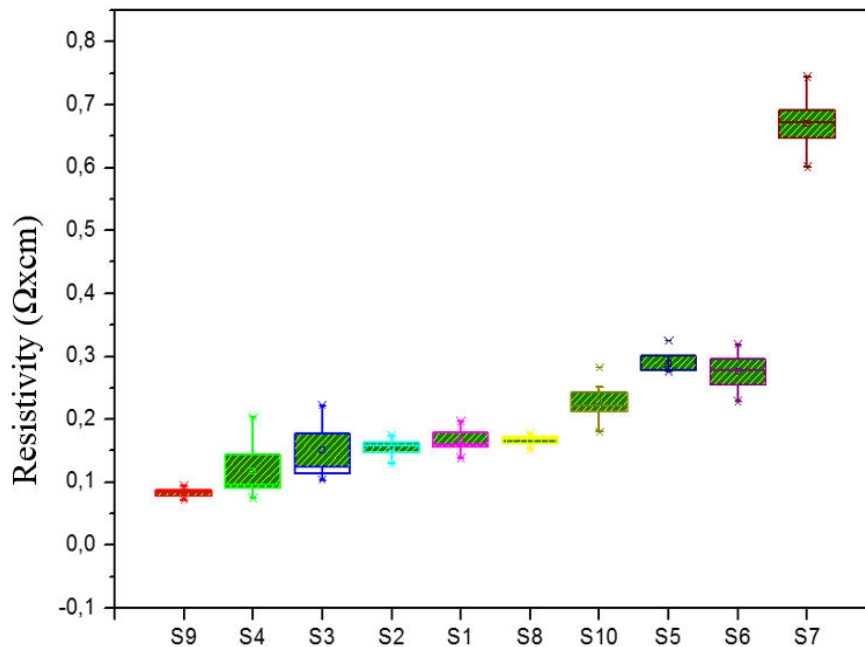


Figure 3.13. Representation of the resistivity mapping and its standard deviation on ICP-CVD deposition.

Observing the results of Figure 3.13, it is represented the values of the resistivity and its standard deviation, devices that present higher dispersion are S4 and S3 that correspond to the samples doped with 20 sccm of PH₃ where RF bias was applied by pulsed of 0-40 W or with a constant RF bias of 40 W. The higher standard deviation of these samples if they are compared with S1 can come because we suspect that the effect of the global stress on the layer induces lower uniformity in the mapping, this higher strain in the layer. It can come from bigger crystallinity, Table 3.7, this means bigger grain size and therefore bigger conductivity but also higher strain in the layer. For that reason, it is important to find a compromise between all these parameters. Moreover, it is observed than S9, S8, S2 show very good uniformity which could be interesting for the final application.

7. Study of the sensitivity of $\mu\text{c-Si}$ under different strain

7.1 Strain calculation

To investigate the sensitivity of $\mu\text{c-Si}$, the structure is submitted to different bending radius of curvature R and the electrical change of the resistance is measured. As was commented in Chapter 2, the parameter used to measure it is well-known as Gauge factor (GF) and is defined in Formula 3.5. Hence, GF in a material depends both on the geometrical change and on the resistivity change.

$$\text{GF} = \frac{\frac{\Delta R}{R}}{\epsilon} \quad (3.5)$$

When the film/substrate structure is bent, the top surface is under tension and the bottom surface is under compression. It exists one part inside the sheet that does not suffer from any strain, this is known as the neutral plane. Figure 3.14 shows the film/substrate structure under bending and the thicknesses are defined such as d_f and d_s and Young's modulus Y_f and Y_s for the film and the substrate.

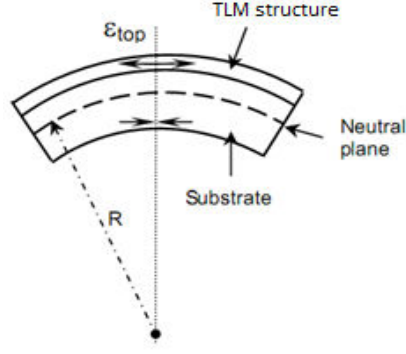


Figure 3.14: Film/substrate structure under a bending radii

In function of the nature of the substrate two different cases are used to calculate the strain in the top surface (ϵ_{top}) [20]:

- a) The film is deposited on a stiff substrate:

If the Young's modulus is the same for film and substrate, the neutral surface corresponds to the middle of the structure and the strain in the top surface is given by formula 3.6:

$$\epsilon_{top} = \left(\frac{d_f + d_s}{2R} \right) \quad (3.6)$$

- b) The film is deposited on a compliant substrate:

If the Young's modulus of the film is bigger than the Young's modulus of the substrate ($Y_f > Y_s$), the neutral surface shifts from the mid surface toward the film. As a consequence, the strain on the upper surface is given by formula 3.7:

$$\epsilon_{top} = \left(\frac{d_f + d_s}{2R} \right) \frac{(1 + 2\eta + \chi\eta^2)}{(1 + \eta)(1 + \chi\eta)} \quad \text{Where } \eta = \frac{d_f}{d_s} \quad \text{and } \chi = \frac{Y_f}{Y_s} \quad (3.7)$$

Figure 3.15 represents the normalized strain in the film (ϵ_{top}) in function of the thickness d_f/d_s . In this Figure, the two cases commented up are compared, a) when film/substrate have the same Young's modulus ($Y_f/Y_s \approx 1$) and, b) when the Young's modulus of the film is higher than the substrate ($Y_f/Y_s \approx 100$).

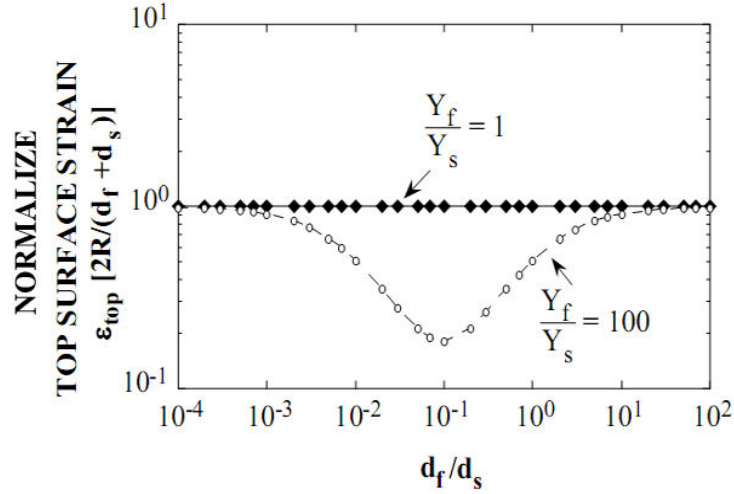


Figure 3.15. Normalize graphic of top surface strain vs the thickness ratio d_f/d_s [19].

In our case, in order to determinate the sensibility of the structure for static deformations, the devices are fixed over half cylinders with different diameters, as shown in Figure 3.16. I-V measurement is performed at room temperature using the Agilent B1500A software within a voltage range of ± 1 V.

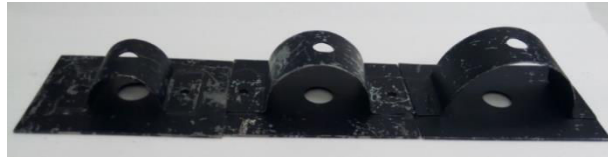


Figure 3.16. Tensile diameter 2 cm, 3 cm and 4 cm.

The characterization process consists in first measuring the resistance without bending (flat substrate) to obtain the initial value. Then, the sample is fixed onto the highest curvature (lowest diameter, 2 cm). This is an important step to obtain a good linearity in the curve. Indeed, when the sample is submitted to the highest bending curvature radius, some cracks can be created, and that increases the value of the resistance. After that, the resistance is measured again without bending (flat state) and this new value is taken as the initial value of the resistance (R_0).

One time that this step is done, the resistance is bent from the higher diameter (5 cm) to the lower (2 cm) and between each bending, resistors are re-flattened.

So to obtain reliability in measurement first, it is necessary to apply to the substrate the highest stresses in order to pre-create the cracks in the layers.

7.2 Strain calculation for our structures

In our case, the film is deposited on a compliant substrate, and for this reason, the calculus realized for the applied strain was done with Formula 3.7. Here it is necessary take in account given values such as the thickness (d) and Young's modulus (Y) for each layer. Table 3.9 shows a summary of them.

	Kapton®	SiNx	μc-Si
Young's modulus (Y)	2.5 GPa	183 GPa	80 GPa
Thickness (d)	50 or 25 μm	50 nm	100 nm

Table 3.9 Thickness (d) and Young's modulus (Y) for the layer used in the structure.

The values obtained for the calculus of each radius of curvature are shown in Table 3.11, the strain ϵ applied is calculated using a bi-layer simplified model [20]. This model only takes into account the substrate and the stiffest layer, because these will determine the mechanical behaviour of the device. Moreover, this model does not consider the electrodes.

Hence, three different calculations depending on the structure are done for each R value.

As shown in Table 3.9, the value of Young's modulus of SiNx is higher than the value of μc-Si. For this reason, for the samples with this layer, the calculation are realized in function of Kapton® substrate and of the SiNx layer.

	Top surface strain calculation ($\epsilon_{top} \%$)		
Radii curvature	Kapton® (50 μm) + SiNx (50 nm) + μC-Si (100 nm)	Kapton® (25 μm) + SiNx (50 nm) + μC-Si (100 nm)	Kapton® (25 μm) + μC-Si (100 nm)
R = 2.5 cm	0.093	0.044	0.045
R = 2 cm	0.117	0.055	0.056
R = 1.5 cm	0.155	0.073	0.074
R = 1 cm	0.233	0.110	0.112
R = 0.5 cm	0.466	0.218	0.223

Table 3.10. Calculations of the strain on the top of the surface for different structures.

8. Sensitivity for N- type $\mu\text{c-Si}$ deposition by PECVD

As we previously studied the deformation detection sensitivity of films elaborated by PECVD [3], our first objective here was to verify that the GF value of $\mu\text{c-Si}$ deposited with this technique presents the same value regardless of the structure.

The values for the strain calculation were extracted from Table 3.10 and the parameters used to deposit $\mu\text{c-Si}$ by PECVD were presented in Section 6.1 above. The three different structures are presented below, and their resistance variation versus the strain calculation is drawn (Figures 3.17, 3.18 and 3.19). GF parameter, is calculated from an average slope of each curve.

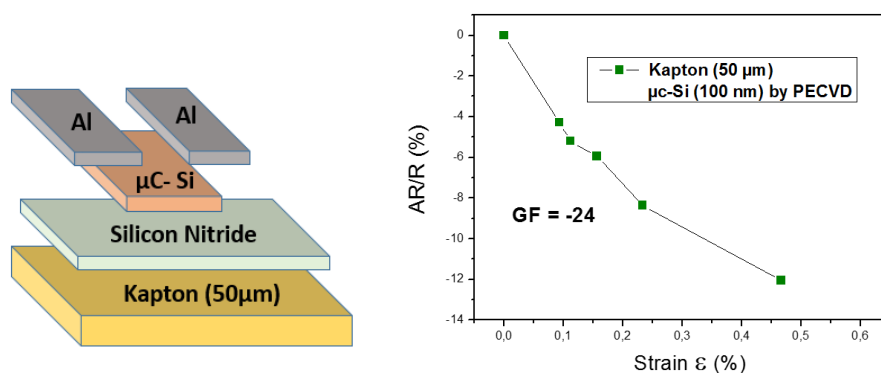


Figure 3.17: GF determination for Kapton® (50 μm) + SiNx (50 nm) + N-type $\mu\text{c-Si}$ (100 nm).

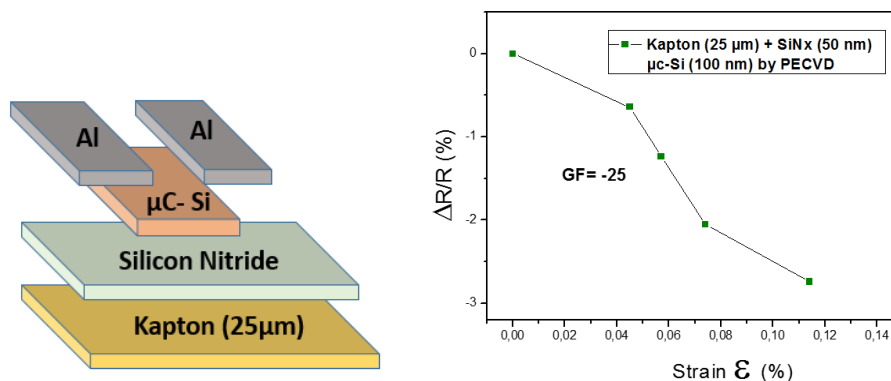


Figure 3.18: GF determination for Kapton® (25 μm) + SiNx (50 nm) + N-type $\mu\text{c-Si}$ (100 nm).

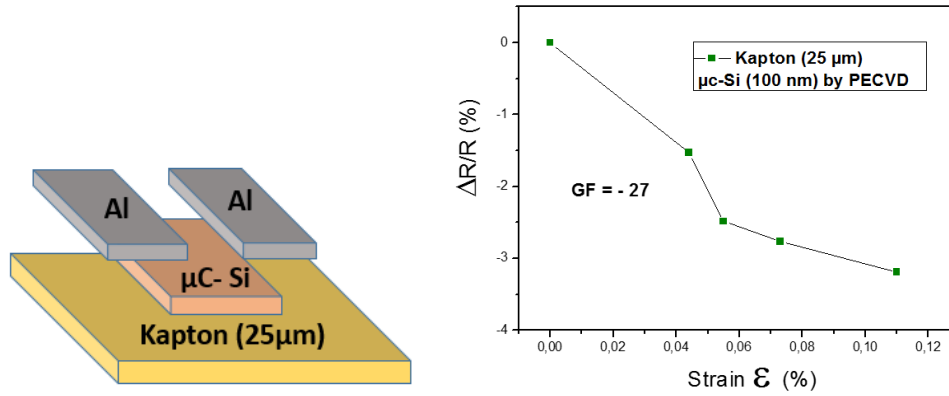


Figure 3.19: GF determination for Kapton® (25 µm) + N-type µc-Si (100 nm).

By observing the results obtained for all these structures, the GF value is practically the same in all cases. However, it is easy to see that the linearity of the slope is worse when the thickness of the substrate is reduced, from 50 µm to 25 µm. This occurs especially during characterization under high strains.

9. Sensitivity for N-type µc-Si deposition by ICP-CVD

As it was commented before, for ICP-CVD technique, the optimal deposition parameters are yet not defined as in the PECVD. Therefore, it is necessary to investigate which could be a good candidate to be used as sensing material under weak deformations. This will be done by analyzing the 10 different conditions showed before in Table 3.6.

To organize the data, the study is divided into different sections and subsections:

a) In function of the nature of the doping gas:

The gases selected to dope µc-Si are AsH₃ and PH₃. To verify if these gases have different behavior in plasma using the same deposition conditions. It is done a comparison where it is only vary the nature of the doping gas to see if there is some effect on sensitivity or if the electrical and mechanical behavior of the material.

b) Selected PH₃ as doping gases:

It has been investigated which plasma parameters can be improved by using PH₃ as doping gas. To do that, the doping flow rate (sccm) of PH₃ has been varied, the effect of applying a pulse on RF or on LF has been studied as well as different constant values of RF power.

One of the biggest problem found during the characterization, beside of the handling of the thin substrate, was the standard deviation of the results, not only in the initial value, but also during the strain deformations.

For all the conditions presented, an average of 5-6 resistances was characterized. For that reason, the graphics are represent with box plot, showing that the standard deviation of some sample is very large, especially for the higher strain.

9.1 Doping gas: AsH₃ or PH₃

When a semiconductor is doped, it means that some “impurities” are added that will change the electrical, optical and structural properties. Silicon belongs to the group IV and the most common dopant agents for it are the group III such as Boron (P-type) or the group V such as Arsine or Phosphine (N-type).

In our case, we decided to focus our depositions on the N-type. We selected AsH₃ and PH₃ as doping agents. Both will be investigated in order to analyze if, by using the same conditions, it exists some change in the sensitivity (GF), or in the resistivity.

This study is divided into several sections such as the comparison of the effect of constant RF and LF power (ICP Power), the influence to add some pulse on RF power or the variation of the doping gas flow rate.

9.1.1 Deposition with constant RF and LF power:

To see the effect of RF and LF power, a doping flow rate of 20 sccm for AsH₃ and PH₃ is tested, with constant RF and LF powers (RF:0 W and LF:600 W). Table 3.11 summarizes the conditions used and the values obtained from the GF.

	RF	LF	Doping gas	GF
SAMPLE 1	0 W	600 W	20 PH₃	-33
SAMPLE 6			20 AsH₃	-35

Table 3.11. Summary conditions and value of the GF obtained for sample 1 and 6.

Moreover, Figure 3.20 presents the box plot of the resistance values under strain. The value of the GF that corresponds to the slope, was extracted from this graphics. GF values are practically the

same for both gases. However, the values of the dispersion obtained in the deformations are higher for PH_3 .

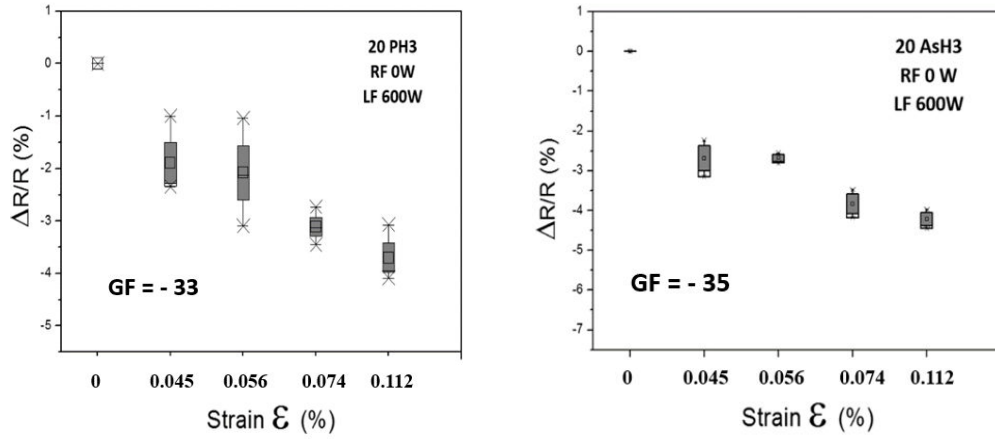


Figure 3.20. Box plot graphic for conditions of Sample 1 and Sample 6.

Figure 3.21 [21] shows the Raman peak in single-crystal silicon when no stress is applied. On this Figure is indicated the shift direction produced in the spectrum when it is submitted to tensile or compressive stress. Raman measurement in flat state was performed for both doping gases, Figure 3.22.

Here, it was observed that for the sample 6 which was doped with AsH_3 , the value of Raman peak corresponds to 521 cm^{-1} . However, when silicon is doped using PH_3 , the value of Raman peak corresponds to 522 cm^{-1} . This change in the spectrum is generated for the stress in the lattice.

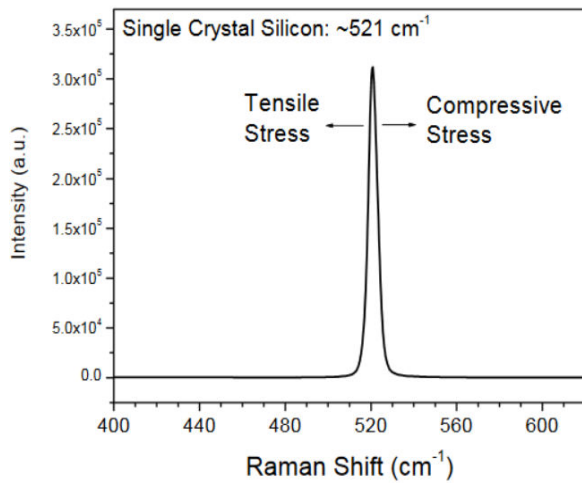


Figure 3.21. Raman spectrum of stress-free single crystal silicon [21].

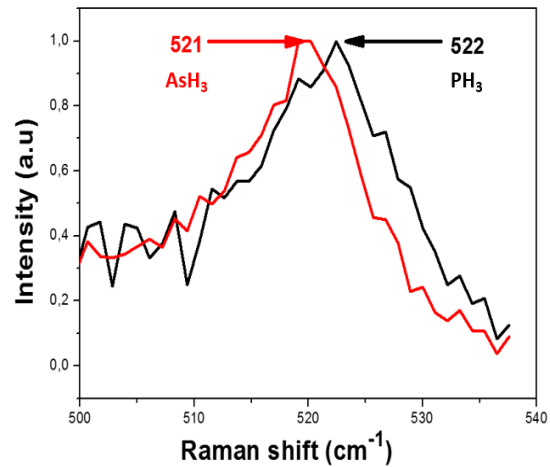


Figure 3.22. Raman spectrum of Sample 1 (black) and sample 6 (red).

This shift can be explained by the fact that the ionic radius of Arsine (119 pm) is similar to that of Silicon (111 pm), but is higher for Phosphorus (195 pm). When the atomic radius is different to the host atoms, this causes strain lattice hence, instability in the crystal structure and in the measures.

The use of Phosphorus as doping gas, whose radius is larger than the host (silicon) induces a compressive stress in the lattice, however for Arsine the ionic radius is similar to silicon, maintain constant the lattice. Therefore, the sensitivity or GF value of both gases is the same however, as it is verify through Raman study and observing Figure 3.20 the linearity obtain during the deformations is better for AsH₃.

9.1.2 Influence on deposition with Pulse in RF power

The values obtained in the GF using a constant RF and LF power is practically the same for both doping gases. We decided then to test if while applying some pulse on RF power, it is possible to see some differences in the sensitivity of N-type μ c-Si. As in previous section, Table 3.12 shows the conditions used with its values followed by the graphics obtained, Figure 3.23.

	RF	LF	Doping gas	GF
SAMPLE 4	PULSE 0-40 W	600 W	20 PH₃	- 30
SAMPLE 5			20 AsH₃	- 45

Table 3.12. Summary conditions and value of the GF obtained for sample 4 and 5.

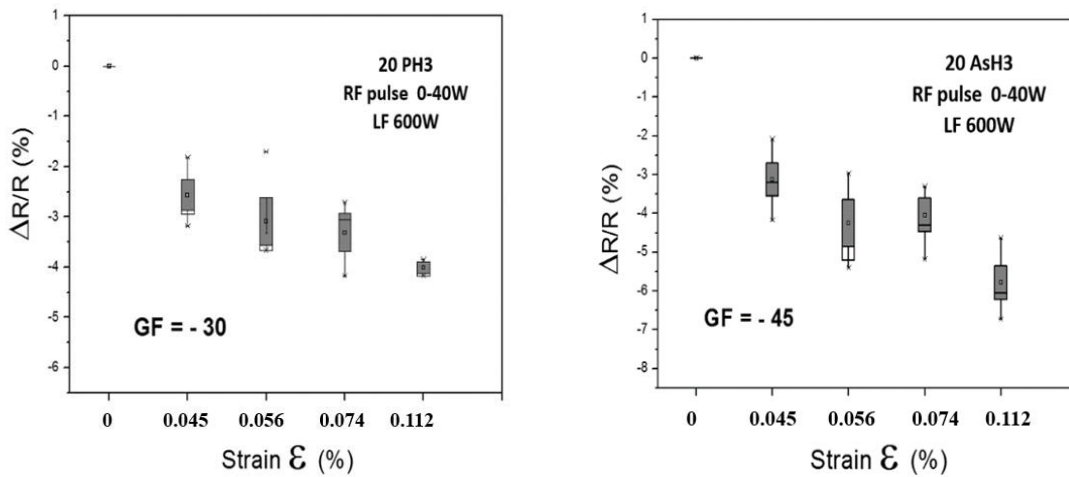


Figure 3.23. Box plot graphic for conditions of Sample 4 and Sample 5.

Here it is obtained a remarkable difference in the GF between both doping agents when a pulse is applied in the RF power.

This is due to the addition of RF pulses in the plasma which generates a bias during the deposition compared to the traditional process without RF power [22]. This bias increase the stress of the layer but also crystallinity and by the way the GF. We can notice that this effect is mainly observable with As as a doping element. It is very interesting to note that RF Bias combined with As incorporation as an effect on piezoresistivity and seems to be more or less useless on P doped layers, once again it should be an effect of the size of the atoms (As is smaller) or perhaps of the strength of links between H and As and P and H during the process of dopant dissociation.

Hence, making a comparison for PH_3 as doping gas, the value of the GF is the same when RF power is applied with RF:0 W (Table 3.11) and RF pulse between 0-40 W (Table 3.12). However, observing the results obtained during the resistivity mapping, the standard deviation of the values is double when the sample is deposited applying pulses in RF power.

When pulses are applied in RF power, and by using AsH_3 as doped gas, the value of the sensitivity increases from -35 to -45. This can be due to the fact that applying pulses on RF power, helps the molecules' dissociation during the deposition process. AsH_3 presents a slow diffusion, around ten times less, than PH_3 as it is shown in the literature [23]. Our theory is then that with the application of pulse in the plasma, this diffusion is accelerated, and leads to an increase of the GF compared to the one obtained with a constant pulse plasma. However, it is important to note that RF bias adjunction has no effect on PH_3 doped layer for GF results.

9.1.3 Effect of doping flow rate with pulse in RF power

After analyzing the sensitivity of the samples while applying pulses in the RF power, we will study the influence of the flow rates of the doping gases on the sensitivity, when they are reduced by half, from 20 sccm to 10 sccm.

Firstly, this was analyzed for PH_3 as doping gas. Table 3.13 shows that there are quite no variation in GF while decreasing the doping level. Figure 3.24 presents the box plot of the change of the resistance under strain. This can be due to the necessity dose required for this gas under the chosen conditions tends to be immediately saturated, which is sufficient with 10 sccm.

Doping Gas: PH ₃				
RF	LF	Gas flow [sccm]		GF
PULSE 0-40 W	600 W	20 sccm	SAMPLE 4	-30
		10 sccm	SAMPLE 9	-35

Table 3.13. Summary conditions and value of the GF obtained for sample 1 and 6.

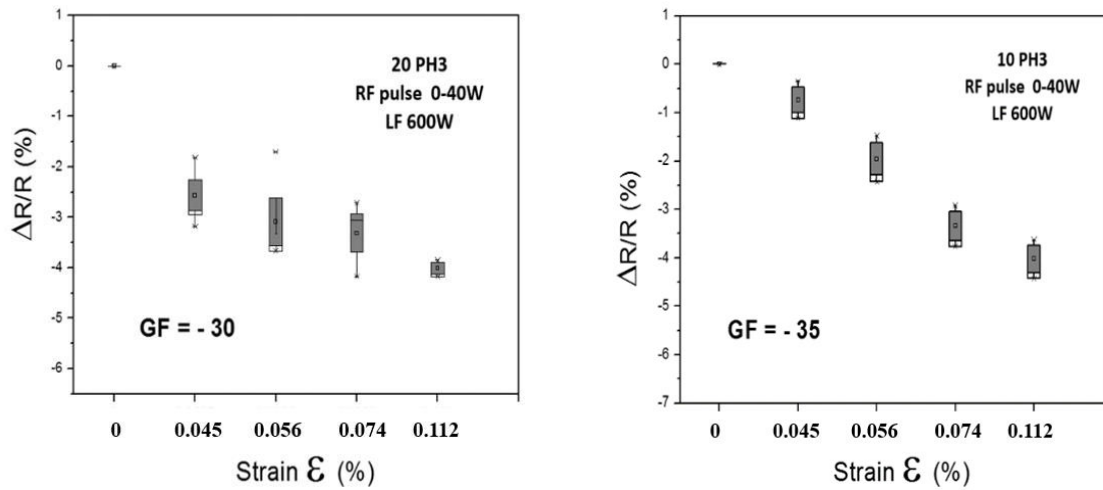


Figure 3.24. Box plot graphic for conditions of Sample 4 and Sample 9.

Here on Figure 3.24, it could be observed that decrease of the resistivity (level of doping) increase GF and also linear regression quality of the measurements.

Secondly, the case of AsH₃ as doping gas is studied. Table 3.14 shows that GF decrease from -45 to -33. Hence the flow rate for this doping gas is relevant in the sensitivity in this case. Indeed, when the gas flow rate of AsH₃ increases, the sensitivity of the material also increases.

Moreover, if it is observed the graphic of Figure 3.25 obtained using a gas flow of AsH₃ of 20 sccm, there are a strongly decrease the uniformity during the deformation, it can come from an increment in the crystalline fraction that increases the instability in the layer.

Doping Gas: AsH ₃				
RF	LF	Gas flow [sccm]		GF
PULSE 0-40 W	600 W	20 sccm	SAMPLE 5	-45
		10 sccm	SAMPLE 10	-33

Table 3.14. Summary conditions and value of the GF obtained for sample 5 and 10.

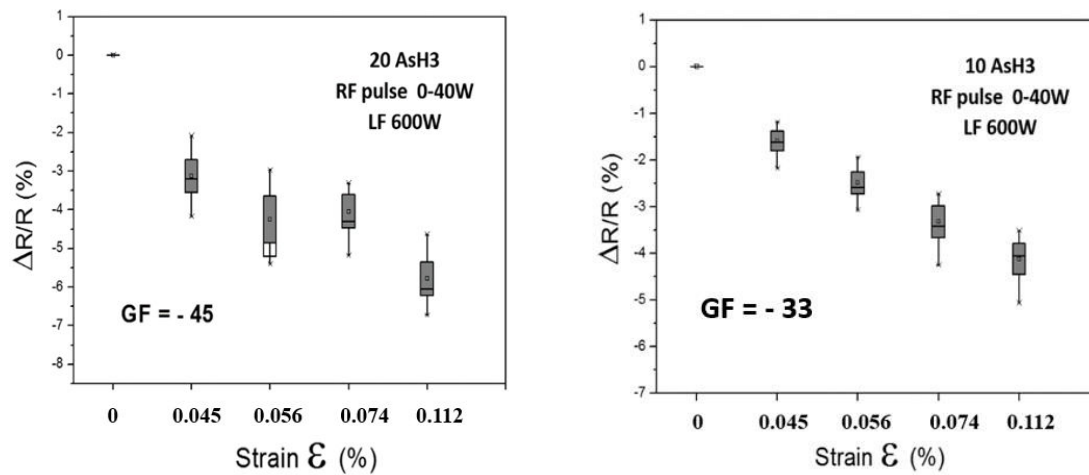


Figure 3.25. Box plot graphic for conditions of Sample 5 and Sample 10.

9.2 Investigation PH₃ as doping gas

In the case of AsH₃ as doping gas, we obtained different results in the sensitivity, depending on the application of pulses in the RF power or when the doping gas flow rate is varied.

It was decided to continue our research using PH₃ as doping gas to see if the modification of the deposition conditions improves the sensitivity. To this end, the following studies are proposed.

9.2.1 Constant RF: 0 W and 40 W

In previous sections, we studied the effect of RF power by applying a constant RF power (RF: 0 W) and with pulse in the range 0-40 W. However, no effect are really detected. For that reason, we have tested if there are some difference when the RF is constant but with higher power, 40 W. When the power is incremented, we add some bias voltage in the plasma which is totally absent using a single ICP plasma. Table 3.15 shows the conditions and the values obtained for the GF.

DOPING GAS:20 (sccm) PH₃			
	RF	LF	GF
SAMPLE 1	0 W	600 W	- 33
SAMPLE 3	40 W		- 35

Table 3.15. Summary conditions and value of the GF obtained for sample 1 and 3.

It is not surprising that these values are quite the same (even if we could notice a 20% variation). Indeed, when pulses in the RF power were applied and the maximum power applied during the pulse correspond to the constant value of RF: 40 W. In this case, GF is higher with a constant bias rather than a pulsed one

9.2.2 Effect of LF or RF power

As it was study before, the applied pulse in RF power does not affect the sensitivity (GF is around -30). For that reason, it was decided to see the effect of the pulse in LF power because it power increase the chemical density of the plasma, improving the disassociation of the molecules.

A study of this effect was done by applying pulse in the LF power from 600 W to 900 W.

Table 3.16 shows a comparative between a constant RF power and the effect of apply pulse in RF and LF power.

DOPING GAS:20 (sccm) PH₃			
	RF	LF	GF
SAMPLE 1	0 W	600 W	- 33
SAMPLE 2	0 W	PULSE	- 45
SAMPLE 4	PULSE	600W	- 30

Table 3.16. Summary conditions and value of the GF obtained for sample 1, 2 and 4.

The pulses addition in LF power produce an increment in the crystallinity fraction also produce an increment in the conductivity due to the decrease of amorphous fraction in boundaries between $\mu\text{c-Si}$ grains of the material, improving its sensitivity. Therefore, only the LF pulse seems to be efficient in case of PH_3 doping

9.2.3 Flow rate in PH_3 with RF: 0 W

Previously, in Table 3.14, the effect of the gas flow rate was studied, when the deposition is realized with pulsed RF between 0 W and 40 W. For this reason, the experiment was repeated by reducing the doping gas flow rate to 20, 10 and 5 sccm. Table 3.17 presents the values obtained for the resistivity and for GF depending of the flow rate used during the deposition process. Figure 3.27 shows these results.

DOPING GAS: PH_3					
	RF	LF	Flow rate [sccm]	ρ (Ωxcm)	GF
SAMPLE 1	0 W	600 W	20 sccm	0.165 ± 0.0228	-33
SAMPLE 8			10 sccm	0.170 ± 0.0151	-45
SAMPLE 7			5 sccm	0.668 ± 0.0447	-60

Table 3.17. Summary conditions and value of the GF obtained for samples 1, 7 and 8.

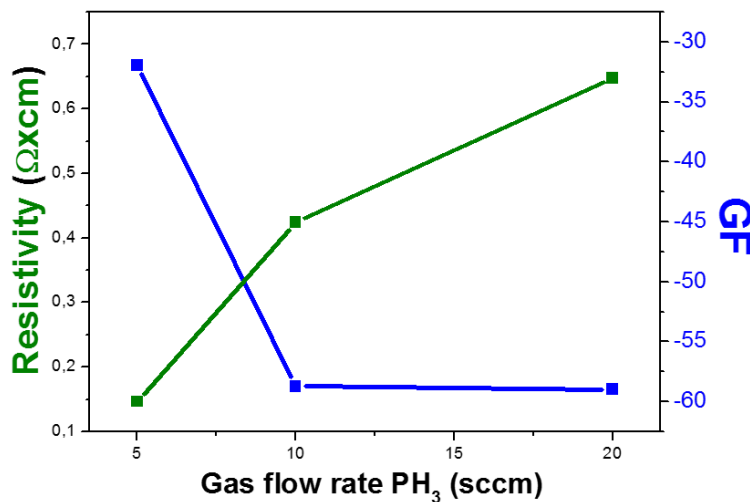


Figure 3.26. Resistivity and GF values in function of gas flow rate (PH_3), conditions of samples 1, 7 and 8.

On Figure 3.26, it is observed that, when the doping concentration is reduced, it leads to an increase in the gauge factor. However, in previous Table 3.14, when AsH_3 is used as doping gas, it occurs in the contrary sense, the GF increases when the flow rate is incremented. This is also observed in the literature, as shown in Figure 3.27 in fact that represents the value of GF for P and N type depositions on polysilicon versus the doping concentration. Here the GF increments until one optimal concentration and after that, it decreases when the doping concentration increases [24].

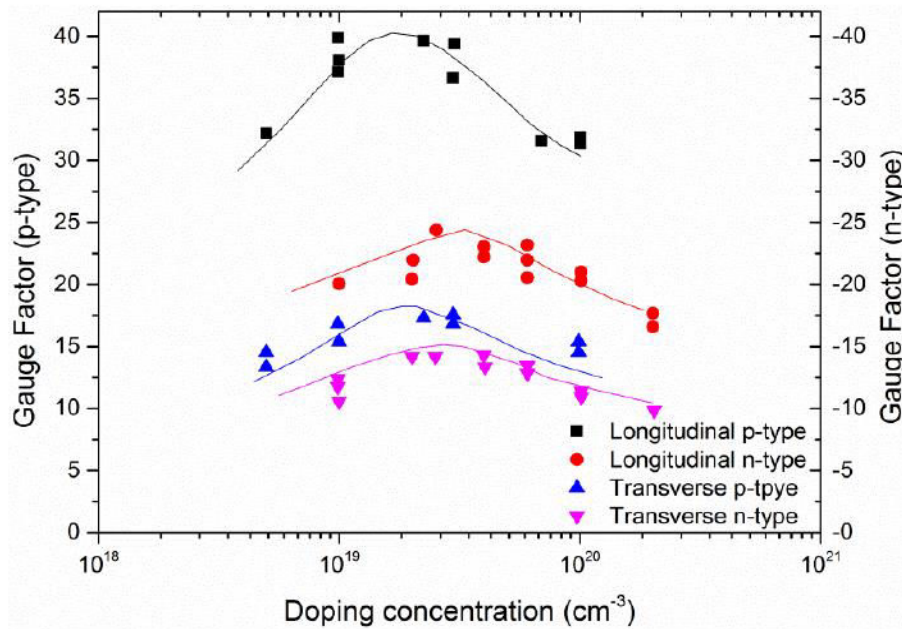


Figure 3.27. GF as a function of doping concentration for boron and phosphorus doped material [24].

10. Conclusion

Throughout this chapter, the piezoresistive properties of $\mu\text{c-Si}$ deposited by two different techniques PECVD and ICP-CVD was analyzed. TLM structure was used for this purpose.

The study was separated into two different parts where during the first part the aim was to study different parameters such as the specific contact resistance or the uniformity of the deposition through resistivity measurement at different points of the sample and in the second part, is focused on the calculation of the sensibility (GF) using different bending radii.

With the results obtained, several things can be highlighted depending on the deposition technique used (PECVD or ICP-CVD).

For samples deposited by PECVD technique, the values obtained for $\mu\text{c-Si}$ were similar to the values obtained before in the laboratory for this material, $\text{GF} = -25$. Moreover, it was observed that a decrease in the thickness of the global structure does not affect the sensitivity of $\mu\text{c-Si}$, as we obtained similar values for the three structures. However, it affects the uniformity of the resistivity thus the standard deviation increase when the thickness of the structure is reduced. It can come from the difficulty of handling during the fabrication process.

ICP-CVD technique was investigated through ten different conditions based on the variation of some key parameters such as:

The nature of the dopant gas (AsH_3 or PH_3) and its concentration. The effect of the apply RF bias using a constant power value or varying the power by pulsing of 400 ms every 4 s. And the effect of LF or ICP power applying it in a continuous mode at 600 W or by small pulses of 900 W during 400 ms every 4 s taking as a base 600 W. The most interesting results can be sum up in the points below, such as:

- When RF power is applying by small pulses, it produces higher crystallinity fraction and lower transfer length value (L_T) being more efficient than use a continuous bias. However, RF pulse adjunction leads to a strong increase of the layer stress which could induce sticking issues on Kapton®.
- Using the same deposition conditions, when it is selected Phosphine as doping gas, it leads to obtain higher crystallinity than Arsine, this fact was also noticed during high-temperature deposition, 700 °C making that we obtain higher values of resistivity in the samples doped with Arsine. However, this affects the linear regression quality of the measurements when it is analyzed the sensitivity of the material to different bending radii.
- For PH_3 , only it appreciates an increment in the sensitivity when it is addition pulses to LF power. ICP power creates high energy in the plasma that affects the dissociation of the molecules that will produce an increment in the conductivity decreasing boundaries between $\mu\text{c-Si}$ grains, improving its sensitivity.

In the next chapter, we will use the deposition conditions used in sample 1 to fabricate the sensors dedicated to dynamic deformations because it offers a compromise between crystallinity

(higher than AsH_3 and lower resistivity than it), the values of its standard deviation are lower than the sample 4 deposited by applying pulses on RF power.

Moreover, the value of the sensitivity, $\text{GF} = -33$ is higher than the value obtained with PECVD, $\text{GF} = -25$. Moreover we decided to keep a strong level a PH_3 doping in order to decrease the global resistance of our devices especially if we want to use it in array design.

11. References

- [1] A. Goetzberger and R. M. Scarlett, ‘Research and investigation of inverse epitaxial uhf power transistors’, Clevite Transistor Palo Alto Ca Shockley Transistor Div, 1964.
- [2] S. Grover, ‘Effect of Transmission Line Measurement (TLM) Geometry on Specific Contact Resistivity Determination’, thesis Rochester Institute of Technology, 2016.
- [3] Y. Kervran ‘Cartographie d’un champ de pression induit par l’occlusion dentaire’, thesis Rennes 1, 2016.
- [4] S. Wolf and R. N. Tauber, Silicon Processing for the Vlsi Era: Process Technology, 2nd ed. Sunset Beach, Calif: Lattice Press, 2000.
- [5] N. Stavitski, J. H. Klootwijk, H. W. van Zeijl, A. Y. Kovalgin, and R. A.M. Wolters, ‘Cross-Bridge Kelvin Resistor Structures for Reliable Measurement of Low Contact Resistances and Contact Interface Characterization’, IEEE Transactions on Semiconductor Manufacturing, vol. 22, pp. 146–152, 2009.
- [6] D. J. Gardiner and P. R. Graves, Eds., Practical Raman Spectroscopy. Berlin Heidelberg: Springer-Verlag, 1989.
- [7] H. Wernerus, M. Bivour, L. Kroely, M. Hermle, and W. Wolke, ‘Characterization of Ultra-thin $\mu\text{c-Si:H}$ Films for Silicon Heterojunction Solar Cells’, Energy Procedia, vol. 55, pp. 310–319, 2014.
- [8] G. Viera, S. Huet, and L. Boufendi, ‘Crystal size and temperature measurements in nanostructured silicon using Raman spectroscopy’, J. Appl. Phys., vol. 90, pp. 4175–4183, 2001.
- [9] J. Zi, H. Büscher, C. Falter, W. Ludwig, K. Zhang, and X. Xie, ‘Raman shifts in Si nanocrystals’, Appl. Phys. Lett., vol. 69, no. 2, pp. 200–202, 1996.
- [10] E. Anastassakis, ‘Strain characterization of polycrystalline diamond and silicon systems’, J. Appl. Phys., vol. 86, pp. 249–258, 1999.
- [11] B. Le. Borgne, ‘Microcapteurs chimiques basés sur des couches nanométriques de silicium polycristallin : application à la détection de plomb’, thesis Rennes 1, 2016.
- [12] K. Kandoussi, ‘Procédé de fabrication à $T < 200^\circ\text{C}$ de transistors en couches minces de silicium microcristallin déposé par PECVD en mélange $\text{SiH}_4\text{-H}_2\text{-Ar}$.’, thesis, Rennes 1, 2007.

- [13] B. J. Jones and J. J. Ojeda, 'Substrate and material transfer effects on the surface chemistry and texture of diamond-like carbon deposited by plasma-enhanced chemical vapour deposition', *Surf. Interface Anal.*, vol. 44, no. 8, pp. 1187–1192, 2012.
- [14] W.-Y. Chang, T.-H. Fang, and Y.-C. Lin, 'Physical characteristics of polyimide films for flexible sensors', *Appl. Phys. A*, vol. 92, pp. 693–701, 2008.
- [15] M. Amirzada, A. Tatzel, V. Viereck, and H. Hillmer, 'Surface roughness analysis of SiO₂ for PECVD, PVD and IBD on different substrates', *Appl. Nanosci.*, vol. 6, pp. 215–222, 2015.
- [16] H. Gleskova, S. Wagner, and Z. Suo, 'Failure resistance of amorphous silicon transistors under extreme in-plane strain', *Appl. Phys. Lett.*, vol. 75, pp. 3011–3013, 1999.
- [17] J. Gaspar, A. Gualdino, B. Lemke, O. Paul, V. Chu, and J. P. Conde, 'Mechanical and piezoresistive properties of thin silicon films deposited by plasma-enhanced chemical vapor deposition and hot-wire chemical vapor deposition at low substrate temperatures', *J. Appl. Phys.*, vol. 112, p. 024906 (8pp.), 2012.
- [18] O. Sagazan, 'Maitrise des procédés de croissance épitaxiale du silicium monocristallin et polycristallin pour des applications micro-systèmes', thesis, Rennes 1, 2005.
- [19] Z. Suo, E. Ma, H. Gleskova, and S. Wagner, 'Mechanics of Rollable and Foldable Film on Foil Electronics', *Appl. Phys. Lett.*, vol. 74, pp. 1177–1179, Feb. 1999.
- [20] H. Gleskova, P. I. Hsu, Z. Xi, J. C. Sturm, Z. Suo, and S. Wagner, 'Field-effect mobility of amorphous silicon thin-film transistors under strain', *J. Non-Cryst. Solids*, vol. 338–340, no. 1 SPEC. ISS., pp. 732–735, 2004.
- [21] V. T. Srikar and S. Spearing, 'A Critical Review of Microscale Mechanical Testing Methods Used in the Design of Microelectromechanical Systems', *Exp. Mech.*, vol. 43, pp. 238–247, Sep. 2003.
- [22] D. Lundin and H. Pedersen, 'High Power Pulsed Plasma Enhanced Chemical Vapor Deposition: A Brief Overview of General Concepts and Early Results', presented at the *Physics Procedia*, vol. 46, pp. 3-11, 2013.
- [23] S. W. Jones, 'Diffusion in Silicon,' copyright (C) 2000 IC Knowledge LLC, pp. 1-68, 2008.

- [24] D. Grech, 'Development of a Quasi-concertina MEMS sensor for the characterization of biopolymers', University of Southampton, Engineering and the Environment, Doctoral Thesis, 2014.

CHAPTER 4 - Piezoresistive response of N-type $\mu\text{c-Si}$ under dynamic deformations

1. Introduction

The previous section has been focussed on the piezoresistive effect of N-type microcrystalline silicon, deposited by using two different deposition techniques, PECVD and ICP-CVD.

Transmission line measure (TLM) structure was used to extract parameters such as contact resistance (R_c), specific contact resistivity (ρ_c) or sheet resistance of the semiconductor (R_{SH}). Moreover, the uniformity and the sensitivity of μc -Si when the material is submitted to different curvature radii, corresponding to the gauge factor (GF), were studied.

These parameters were obtained through a static characterization bending test, however, one of the main innovations of this thesis is to study how μc -Si reacts to dynamic deformations to perform a sensor that is able to detect fast, continuous and weak deformations.

There are important advantages when dynamic measurements are realized because it provides more information about the behaviour of the materials and the sensor's structure. To obtain a sensor with good reliability and accuracy, the reaction to the applied stimulus should be linear, with high sensibility. The amplitude of the variations should present similar values and moreover, the intrinsic structure of the materials should be able to come back quickly to the initial state.

Unfortunately, the main disadvantage of dynamic deformation is that it requires expensive and sophisticated characterization systems. For this reason, in our case, various low-cost prototypes have been developed with a home-made acquisition system set up. These have been evolved along this thesis until the completion of the final design.

Since this was the first time μc -Si was submitted to dynamic deformations in the laboratory, we did not know how it would react. For this reason, the first circuit was designed to be used with a wide range of resistance values. To make a comparison between the structures studied, different parameters as geometries were tested to characterize the sensors and those to which all the sensors are able to react were selected.

Hence, along this chapter, we will explain the process followed in the development of the new acquisition system, the considerations taken to choose the appropriate microcontroller and the creation of a new specific software code for this one. Furthermore, an electronic circuit has been developed to adapt the new design. Several prototypes were created to obtain a reliable frequency system that allows working with variable deformations and allows to apply different wave shapes

over the devices. Therefore, in order to create the new dynamic set up, it was necessary to modify the computer processing, the connectors and the prototypes to realize the deformation.

The signal processing system selected for this new system is the Arduino platform, because it presents some advantages as a good quality to price ratio, a big forum platform with many projects and examples, a C-based programming language that allows a user with basic programming knowledge configures the microcontroller. However, it presents some design limitations as the resolution levels, the range of input voltage, the processing speed, and so on. These limits will be commented below. This fact forces us to look for other alternatives to adapt our sensors and take full advantage of all the possibilities offered by Arduino.

2. Characterization system

One of the main reasons to discard TLM mask to perform dynamic measurements is that its design is not adequate for this type of measurement; moreover, due to its geometry design, it induces noise during its characterization.

The previous characterization system based on probes with needles on the edge, it is not compatible with dynamic deformations, so it was necessary to create a new one dedicated to dynamic deformations.

The first problem was to design a system to applied continuous deformations always with the same amplitude and modulating frequency. To do that, several ideas were proposed, such as flex tensional piezoelectric actuator, or the use of a motor with cylinders that press the sensor; however, all these options were not precise.

After some research and testing with a homemade system used to apply the deformations, a flow control system called Elveflow OB1 [1] was bought. This equipment is based on piezoelectric regulators, enabling a flow control 20 times more precise and 10 times faster than the other flow controllers on the market. Generally, it is used for microfluidic applications but in our case, it has been configured to be used with compressed air. Moreover, it was necessary to create a platform to apply this pressure. For this goal, the sensor is placed onto a homemade vibration membrane that changes its shape when the impulse is applied. As the sensor is totally attached to the membrane, the impulse is exactly reproduced on the sensor. The vibration membrane is

connected to the pressure supply machine whose outlet can be set with a specific pressure range that can be modulated to create different shapes. The system is shown on Figure 4.1.

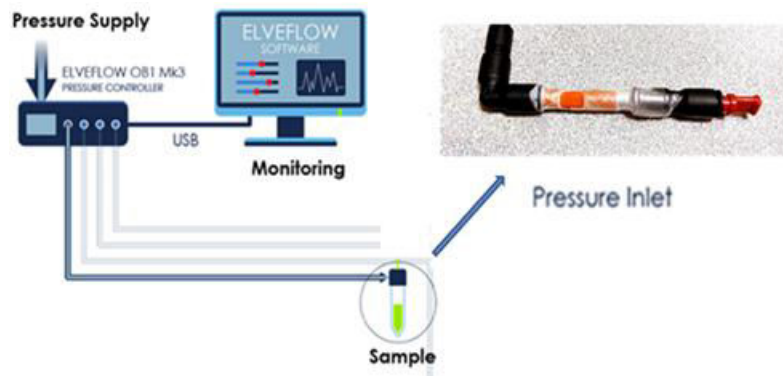


Figure 4.1. Schematic of Elveflow OB1 pressure machine and rubber membrane [1].

For the TLM mask, the electrodes are very close to the place where the deformation is applied and the probes used to realize the characterization have a needle in the edge to realize the contact between the devices' electrodes and the acquisition system, as shown Figure 4.2. For dynamic measurements, this method is not a good option for two reasons: *i*) due to the low thickness of the substrate ($25\text{ }\mu\text{m}$) it is easier that the needle makes holes on it during the manipulation, *ii*) moreover, when the deformation is applied, the membrane moves and the distance between the probes and the electrodes changes. For that reason, in order not to lose contact, it is necessary that the probes move with the stimulus. This fact was an important reason in the design of the new mask to place the electrodes at the edge of the mask area and the devices structure in the centre where will be applied the deformations.

To perform the connection between devices probes we tried different methods until we found the most appropriated to our goal.

For the design of the new mask, the electrodes have been done following the dimensions required to use the connector shown in Figure 4.3. These connectors used a kind of pins that must be embedded in the substrate, however when some vibrations of the deformation go to the edge, the pins produced a tear on the thin substrate.

Another option, tested to discard the use of the probes needles, pins or another method that implies creating holes on the substrate, was to use directly thin wires soldered to the electrodes through silver conductive Epoxy. Figure 4.4 shows an example of this.

With this method, the contact between electrodes and probes is total; moreover there are no holes on the substrate. The big drawback is that the solder have to be done on each device, with difficulty for the handle and with high time-consuming.

Finally, to optimize the time and make a mix between the main advantages of the three connector's methods used, it was designed a board card shown on Figure 4.5. It consists of a piece of PCB card where the electrodes are printed with the same dimensions than the electrodes of our mask design and both of them are pressed between them.



Figure 4.2. Characterization system based on probes with needles to perform static deformations.

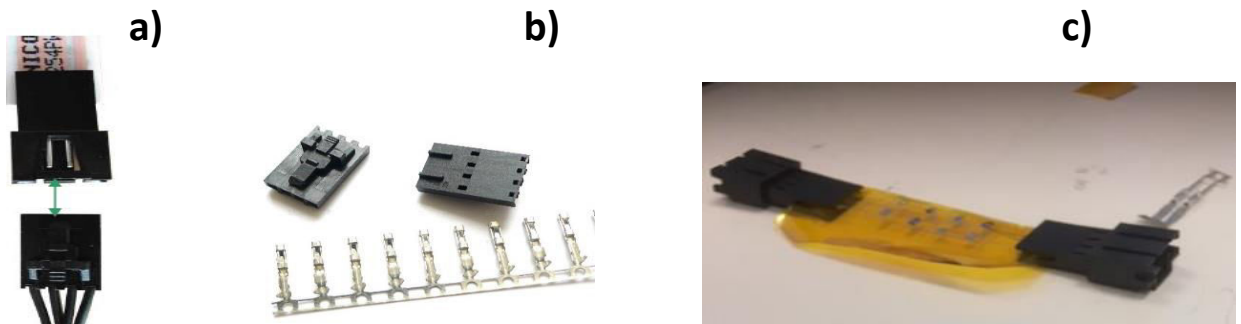


Figure 4.3. a) Connectors adapter for the new mask b) Pins that are embedded to the substrate c) New mask design with the connector.



Figure 4.4. Silver conductive Epoxy and example of one of our sensor

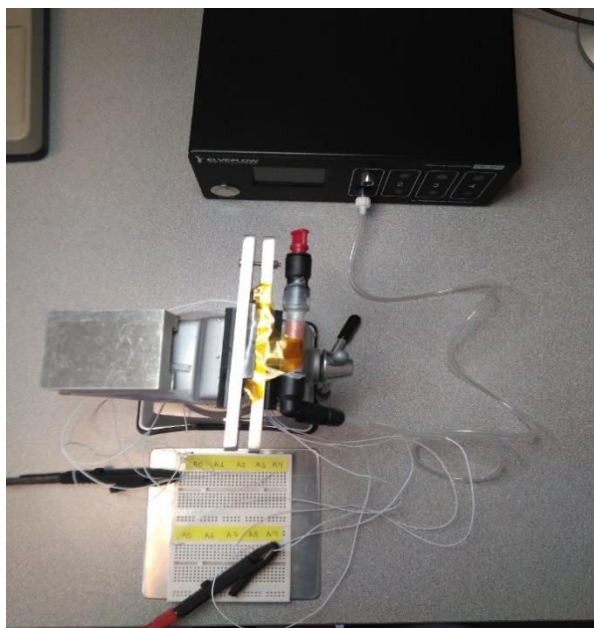


Figure 4.5. Board card of resin with printed electrodes and final system with the sensors connected to the board card.

3. Data acquisition system

The necessity to change the probes connectors forced us to modify the acquisition system. We decided to choose a small system that can be easily transported to get a mobile system.

Currently, in the electronic market we can find different low-cost hardware to perform data acquisition. However for our project, Arduino was selected because it is one of the most used. This platform gives huge information, documents, forums and projects available that helped us to solve our problems.

Then, to show the possibilities that it offers and the considerations that had to be taken into account, its architecture and the basic knowledge that it is necessary to understand how to work with this microcontroller are briefly explained. Figure 4.6 shows a picture of Arduino UNO with its components.

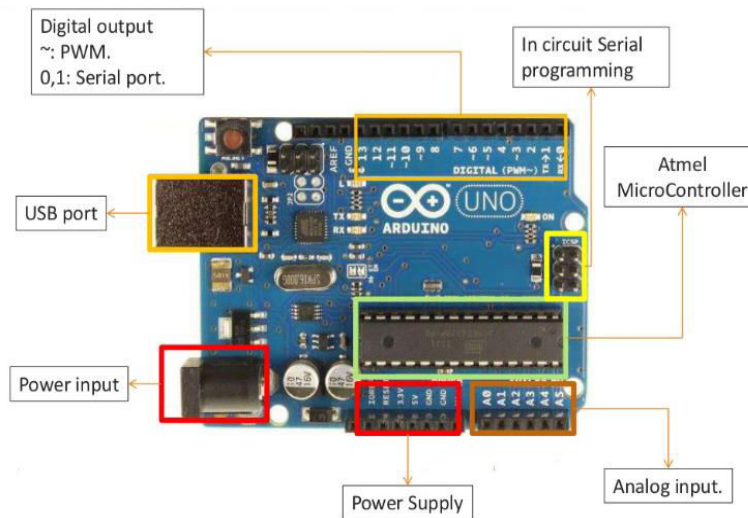


Figure 4.6. Arduino UNO architecture [2].

The pins' groups can be divided into the digital pins and the analog pins. However, for our circuit, only analog pins are used and they are used to transform the signal produced by the sensor into information easy to process for the ADC converter.

The analog pins are connected to the ADC converter through a multiplexer. This is a necessary component as the Arduino doesn't present the possibility to work with more than one input at the same time, which means that once one input is analysed, it can shift to the next one. The time that it needs to read one analog input and pass to the next takes around 100 microseconds, so the maximum reading rate is about 10,000 times a second [2]. This is important to take it into account if we want to compare the data of several inputs.

Each of these pins is capable of digitizing an input signal between 0 V and 5 VCC, converting the input voltage to a numerical value that goes from zero to 1023; this range of values corresponds to the resolution of the ADC [3]. Depending on the ADC chose and the technology used in the microcontroller, we will be limited to certain design parameters (resolution levels, input voltage levels, processing speed, etc.).

In Arduino's case, the microcontroller used is ATME328P-PU, the most important characteristics of Arduino UNO are shown in Table 4.1 [2].

Voltage range	0-5 V	CPU	8 bits
Microcontroller	ATmega328P	Clock frequency	16 MHz
Digital Pins	14	ADC resolution	10 bits
Analog/PWM Pins	6	Current outside pins	40 mA

Table 4.1. Basic specifications of the Arduino UNO [2].

4. Deformation measurement: electronic and signal processing

For our targeted application, Arduino presents some limitations in respect to the resolution, voltage range or processing speed. For that reason, it was necessary to create an adaptive electronic circuit to measure the voltage variation produced when the sensors are submitted to different and continuous deformations.

For Arduino, the resolution of the ADC is 4.88 mV, it corresponds to the minimum step between two data points. Our sensors react with variations of few mV for that reason the idea of the adaptive circuit is to select only the variation produced by the deformation and make the amplification of it.

Figure 4.7 shows the global schematic of the adaptive circuit. However, following it will be explained all the steps follow before introducing the signal in the microcontroller.

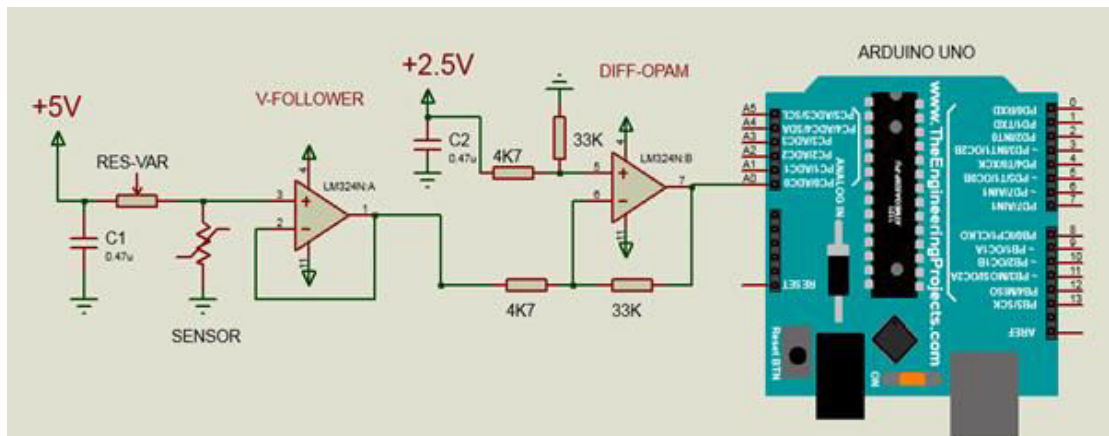


Figure 4.7. Schematic used to adapt our sensor to the acquisition system.

The first block, as shown in Figure 4.8, is used to design a voltage divider between our sensor and a variable resistance or potentiometer.

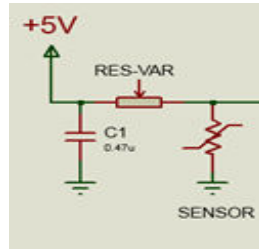


Figure 4.8. Schematic of a voltage divider between our sensor and a variable resistance.

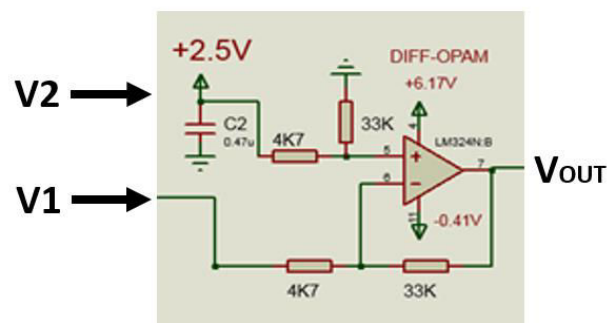
After that, the signal is introduced in an operational buffer or voltage follower, the goal of this component is to prevent the signal source from being affected by any voltages or current.

When the value of the variable resistance in the voltage divider is changed, it is possible to adjust the value of the voltage that we want in the output. It is important to control this value to determinate the voltage reference that will be introduced in Arduino, thus this value will correspond to the negative voltage input, V1, of the differential amplifier.

The last block used is the differential amplifier. The purpose of this electronic component is double: it makes a difference between two input voltages, which suppresses any voltage common to the two inputs and it amplifies this difference.

Figure 4.9 shows the electronic schematic of this component, where there are two input voltages, V1 (-) that is the voltage signal providing for the voltage divider block, Figure 4.8, and V2 (+) a reference voltage that we have defined as 2.5 V.

Moreover, it is possible to do an amplification step which in our case corresponds to gain ≈ 7 .



$$V_{OUT} = \text{Gain} \times (V2 - V1)$$

Figure 4.9. Schematic differential amplifier.

When the design of the differential amplifier block was realized, we decided to introduce the signal from our sensor in the negative input, V1 (-). This is due to the fact that for our sensors, the

semiconductor material selected is N-type $\mu\text{c-Si}$ and as explained in Chapter 2, with tensile strain, its value decreases. Therefore, in order to make it visually simpler, the signal is inverted, so when a tensile pulse is applied, the resulting signal will increase. One of the main advantages of our design is that it is possible to shift the voltage signal through the voltage divider to fix our signal input reference in Arduino to a determined value. For example, if the input voltage reference is fixed to 2 V it is possible to apply deformations in both senses for our sensor, compressive and tensile.

5. Problems and limitation of acquisition system

5.1 Electrical noise

One of the biggest problems we found during the acquisition was the electrical noise. The low level of the variation produced in the signal when the impulse pressure is applied makes it difficult to have distinguishable levels between the electrical noise of the circuit and the variation of the signal.

Depending on the variation of the pressure applied, the signals obtained by the strain gauge can be very small. As a consequence, error signals can even exceed the amplitudes of the measuring signals, so, in order to determine the sensitivity of our sensor and its working range, this error signal must be suppressed by hardware or by software. Figure 4.10 is an example, a square pulse signal is applied with a weak variation of pressure, 20 mbar. We observe then that the sensor is sensible enough to follow the shape of the signal applied, however by observing this graphic, we can see that the level of noise is 0.02 V and the voltage variation on the sensor is 0.01 V. Hence, the noise totally covers the sensor signal.

For a square signal, where the deformation applied stays in the same position for certain time, it is possible to distinguish something, however, when the impulse applied is with short duration it is not possible to differentiate the noise from the actual signal.

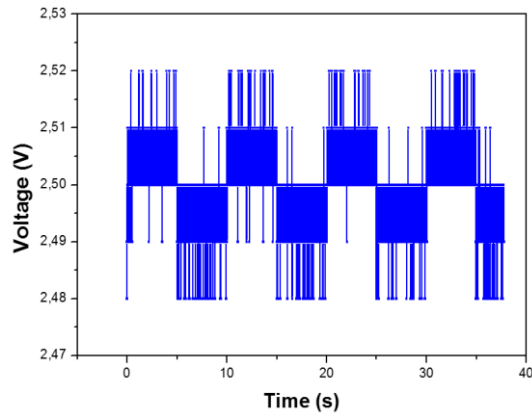


Figure 4.10. Signal obtained when a square signal is applied with variable pressure 40-20 mbar with pulse duration of 5 seconds.

To try to eliminate this problem, we decided to remove the noise of the recovered signal. The filter condition was realized by Origin 8 software. To do this, we first calculated the FFT (Fast Fourier Transform) and based on it, the original signal was filtered with a low pass filter. Figure 4.11 shows an example of a sensor reaction when it is applied ECG signal using a pressure variation of 400 mbar and a frequency of 1 Hz and it is filtered using a low pass filter with a cut-off frequency $f_c = 48$ Hz. The red wave corresponds to the filtered signal and the black one is the original signal.

However, this cut-off frequency (f_c) is not always the same, there are some variations on it that could come from different sources such as the vibration of the membrane, the frequency pulse applied or from the $\mu\text{-Si}$ layer. Moreover, it was not possible to obtain good filtering of the signal in all cases because of the resolution of the ADC, 10 bits, the digital signal obtained is not very accurate for good signal treatment condition.

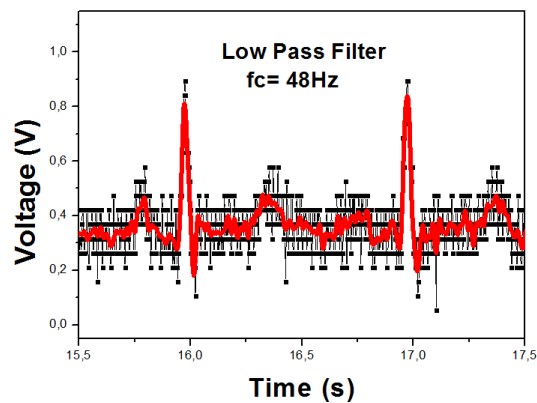


Figure 4.11. Low pass filter with cut-off frequency $f_c = 48$ Hz. ECG shape using a variation of pressure of 400 mbar

5.2 Increase ADC resolution since 10 to 32 bits

The other main problem along with the noise is the resolution level of the ADC. As it was commented before, Arduino's ADC has a voltage range from 0-5 V and 10 bits of the resolution, so the minimum quantum step corresponds to 4.88 mV. To improve this resolution, there are only two possible solutions:

1. Arduino has the option to modify the voltage reference of the ADC with the AREF pin, this pin gives us 3.3 V instead of 5 V. Using 3.3 V, the minimum distance between two points will be 3.22 mV instead of 4.88 mV. However, this option reduces the maximum voltage range of the ADC since 5 V to 3.3 V, in this way the hardware amplification that we can realize also is reduced.
2. The second option, which is also the most efficient, is to increment the ADC bits without varying its voltage range. To do this, the unique solution is to connect a new module to Arduino. The selected module is called ADS126 [5], it is a 32-bit Analog-to-Digital Converter (ADC) with Programmable Gain Amplifier (PGA). Moreover this module offers some incorporated filter such as 50 Hz reject filter or some others that can be configured. Thanks to the higher resolution, it will be easier to filter the signal later with Origin software.

6. Sensor design to perform dynamic measures

When dynamic deformations are applied, there are several factors that influence the behaviour of the devices. To obtain a sensor that reacts quickly, linearly and with a good sensibility to the deformations, it is necessary to select the appropriate materials and design because both are relevant for the sensor working.

In our case, we wanted to investigate $\mu\text{c-Si}$ effect under dynamic deformation and use different geometry design to improve its sensitivity.

Depending on the sensor's application and the nature of the substrate (rigid, flexible or stretchable), there are different geometries such as serpentine, rosette, etc. Selecting an appropriate design will help to improve the sensitivity as well as the quality-life and efficiency of the devices.

As it was commented before, the necessity to modify the probe for the characterization system to apply dynamic deformations offered us the possibility to change the mask design for a new one adapted to our new acquisition system. It was then necessary to consider different factors.

In a strain sensor, the Gauge factor (GF) depends on the Formula 4.1:

$$GF = (1 + 2\nu) + \frac{(\Delta\rho)}{\rho} = \frac{dR/R}{\varepsilon} \quad (4.1)$$

with ε the mechanical strain, R the electrical resistance, ν the Poisson's ratio, ρ the resistivity.

By observing this formula, it can be deduced that to improve the GF it is necessary to increase the variation of the resistance induced by deformation. Figure 4.12 shows the design of a resistance. Hence, to improve the sensitivity, the length (L) must be increased without increasing the cross-sectional area (A).

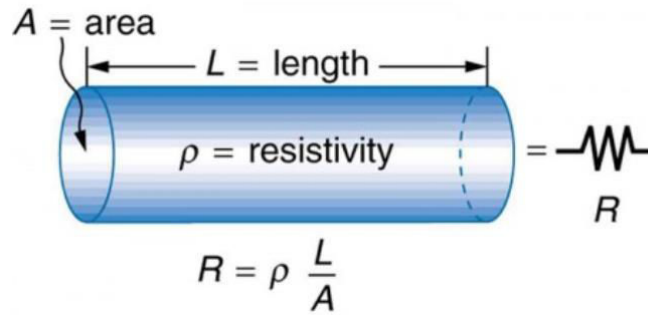


Figure 4.12. Resistance design and formula area definition [6].

Our sensors designs are based on strain gauges. For commercial gauges, their length is the active or strain-sensitive length of the grid and, as shown in Figure 4.13, resistance is generally designed with a long length in a small area. However in our case, due to the relative rigidity of $\mu\text{c-Si}$ and the previous problems found on this material with the cracks, it was decided to increment the length using a simple design.

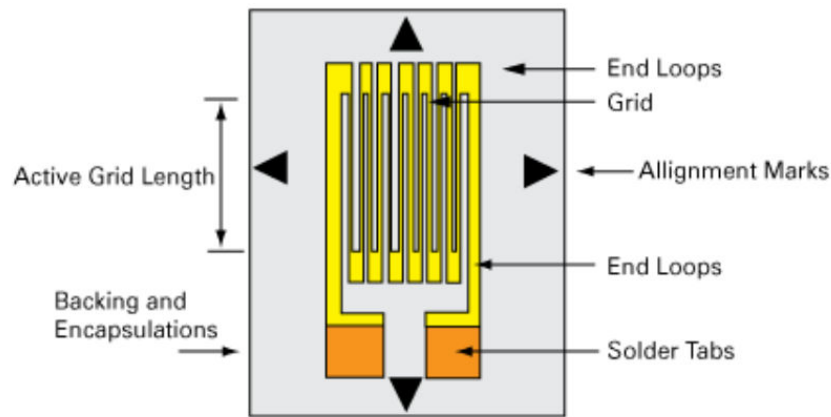


Figure 4.13. Design for a commercial strain gauge sensor [7].

To study the geometry, a mask was designed with Virtuoso Analog Design Software shown in Figure 4.14. It is composed of resistances designs with square shapes and ten resistances in parallel. Table 4.2 presents the different dimensions of this mask design; for the same length (L) there are two different structures with different width (W) (a) and (b).

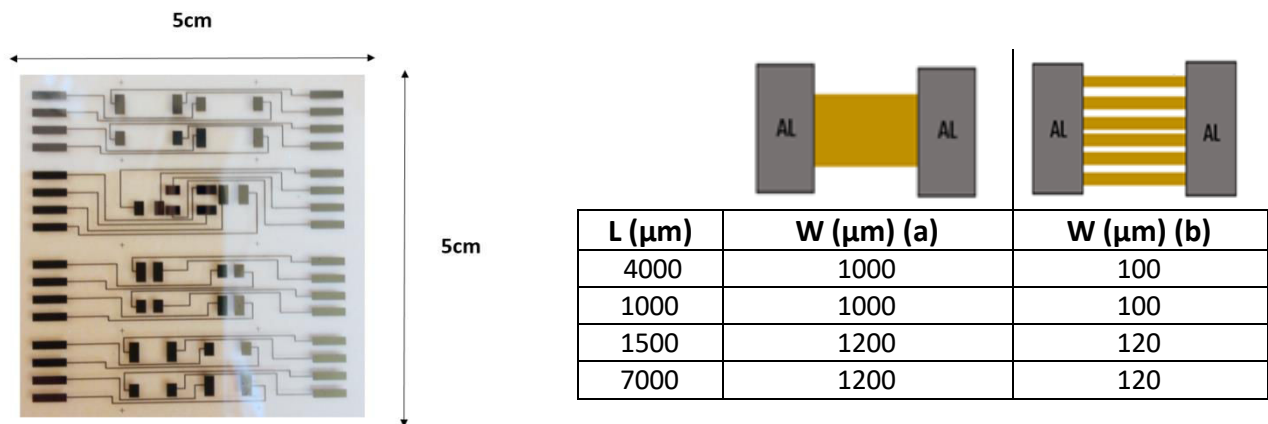


Figure 4.14. Mask resistance design.

Table 4.2. Dimensions of the resistances of the mask of Figure 4.14.

Figures 4.15 (c), (d), (e) belong to a mask available in the laboratory. The design of this mask is realized to be used with the characterization probes that use needles. To use them with dynamic deformations, it was necessary to stick wires using adhesive conductive epoxy to the 2 rectangular aluminium contacts. Following, in Figure 4.15 all of the shapes studied are presented.

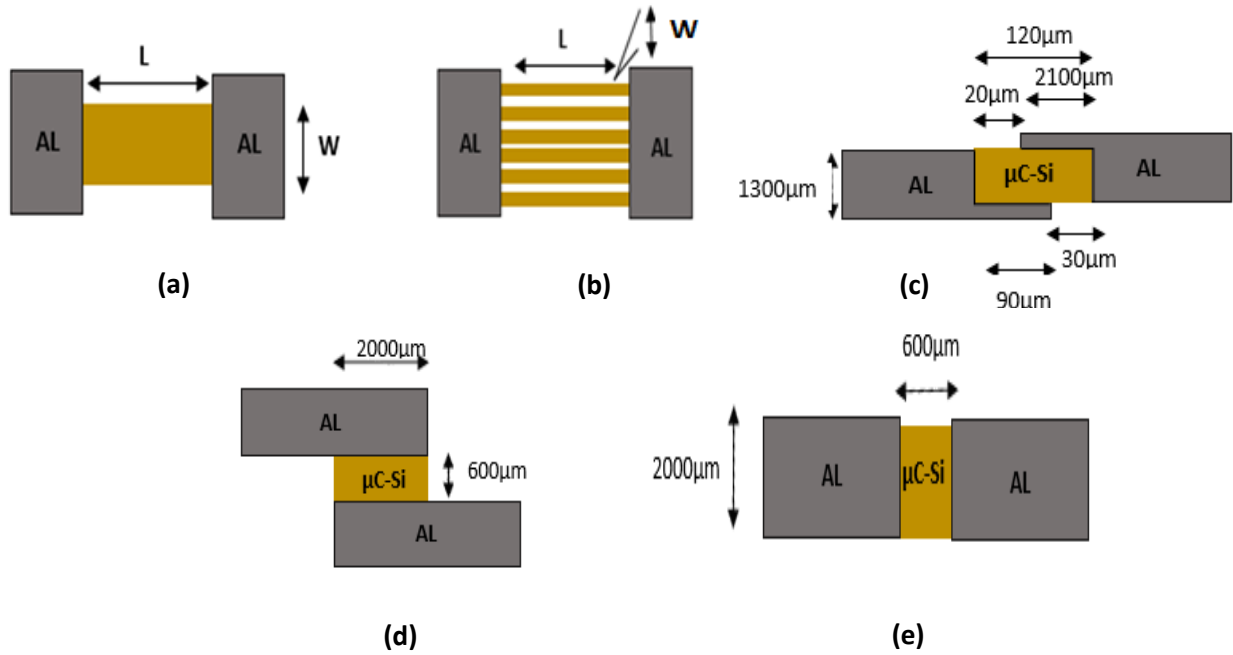


Figure 4.15. Shapes design of the structures studied.

Experimental protocol

The sensors are attached on a vibration membrane connected to a flow controller that injects the specific signal shape with the desired pressure. The sensor should reproduce the same shape as the signal applied. Figure 4.16 shows the membrane and how the sensor is attached on it.

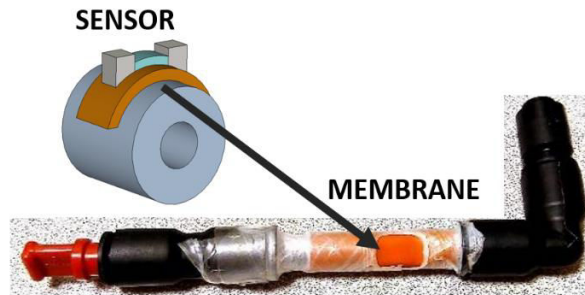


Figure 4.16. Membrane homemade design and sensor place during the deformation.

In order to evaluate the sensitivity of the different structures for weak deformation, we studied their reaction to the same stimulus to determine which design and dimensions could be a good choice for our targeted application.

This was the first time that these structures were submitted to dynamic deformation, so it was necessary to select the stimulus applied to perform our study. To do that, sensors were submitted to different conditions such as maximum and minimum pressure, wave shape, frequency and duration of pulse until we determined with which conditions a reaction is observed for all the structures. Finally, the selected conditions are shown in Figure 4.17 which corresponds to a simple square pulse with a pressure variation of pressure of 200 mbar and a selected frequency of 0.1 Hz.

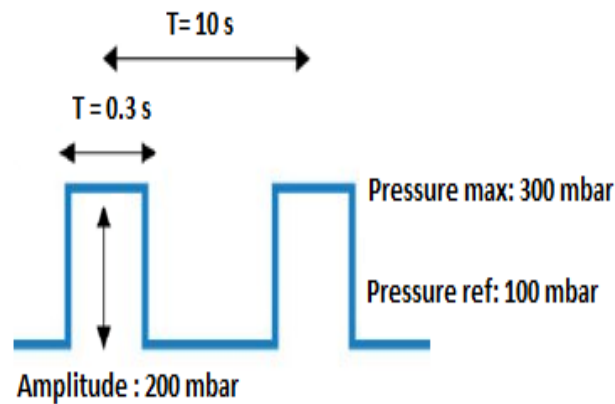


Figure 4.17. Wave conditions selected to do the study of sensitivity in our sensors.

6.1 Design electrodes configuration

To better understand the influence of the sensors behaviour design under strain, the first step is to select which electrode configuration is more sensible to the deformations. The correlation between resistance and current flows perpendicular or parallel to the direction of strain was previously reported [8], [9], [10]. These studies demonstrated that when the strain is applied, the stress is concentrated on the electrodes and causes cracks that are perpendicular to the strain direction [11].

Hence, the sense of the current flow in the function of the strain deformation has an important effect on sensor performance. The position of the electrodes determines the current flow sense and corresponds to the length value (L). Figure 4.18 shows two of these possibilities.

In Figure 4.18 (a) the strain applied is perpendicular to the current flow and the signal applied is almost not appreciated and it does not react to half of the stimuli applied, Figure 4.19 (a). This can come from the deformation is produced in the width (W) of the resistance. However, when

the current-strains are parallel between them, Figure 4.18 (b), the deformation is applied over the length (L). This structure is shown less drift, more uniformity in the amplitude of the peaks and better response and recovery time, Figure 4.19 (b).

Both graphics of Figure 4.19 have been normalized, because for this section the main interest is the study of the signal waveforms obtained in both cases. The effect in the reliability of the structure, the linearity, the uniformity in the amplitude of the peaks to see which configuration helps to recover faster the initial shape to react to all the applied stimuli. As we expected and it was previously demonstrated in the literature, the best configuration is one where the strain applied is parallel to the current flow which corresponds to Figure 4.19 (b). This structure will be studied later without normalization to see its voltage variation in front of a deformation.

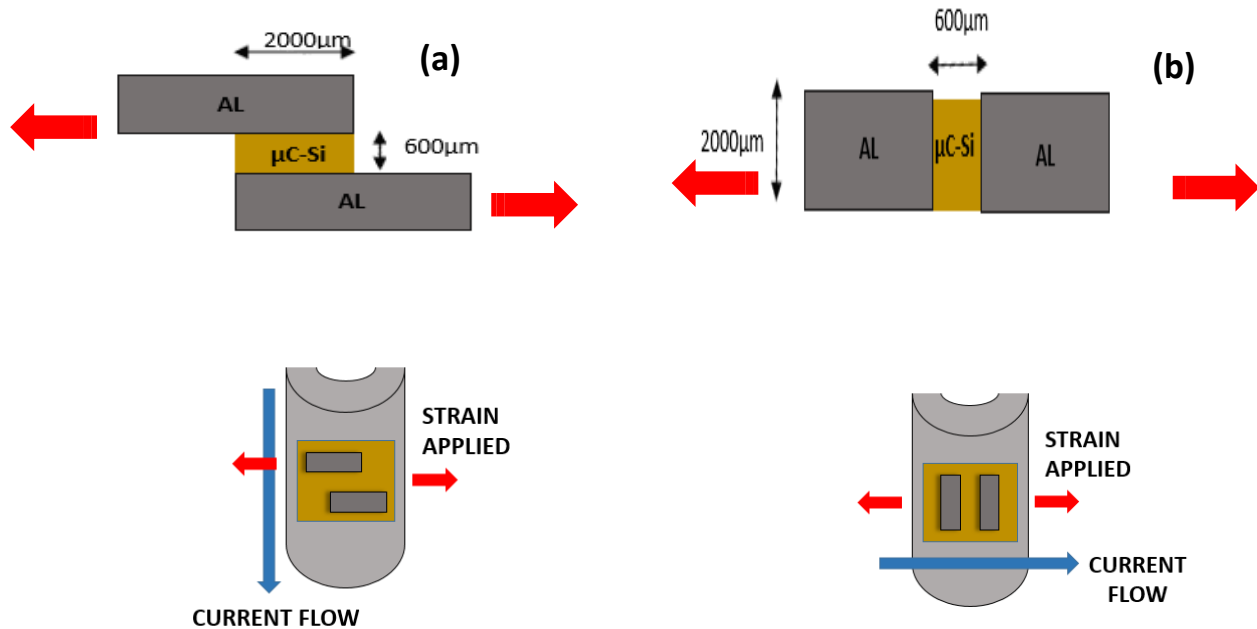


Figure 4.18. Electrodes configuration: (a) The strain applied is perpendicular to the current flow; (b) The strain applied is parallel to the current flow.

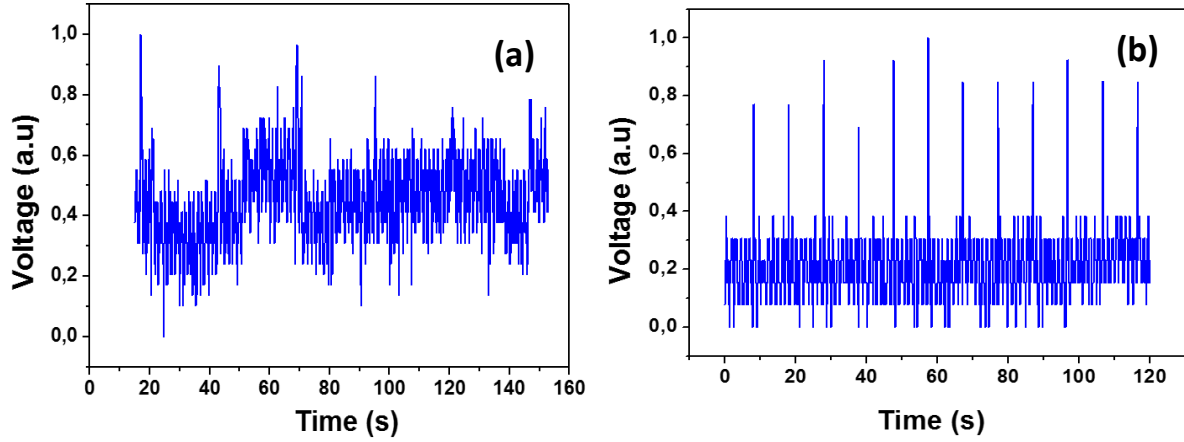


Figure 4.19. Normalized results obtained with electrodes configuration of Figure 4.21. (a) The strain applied is perpendicular to the current flow; (b) The strain applied is parallel to the current flow.

In addition, it was decided to analyze the structure of Figure 4.20 where the current flow has two different directions, first parallels to the strain and later perpendicular to it. However, using this structure, it is impossible to obtain a distinguishable signal. For that reason as the results are impossible to analyse, we could discard this kind of geometry.

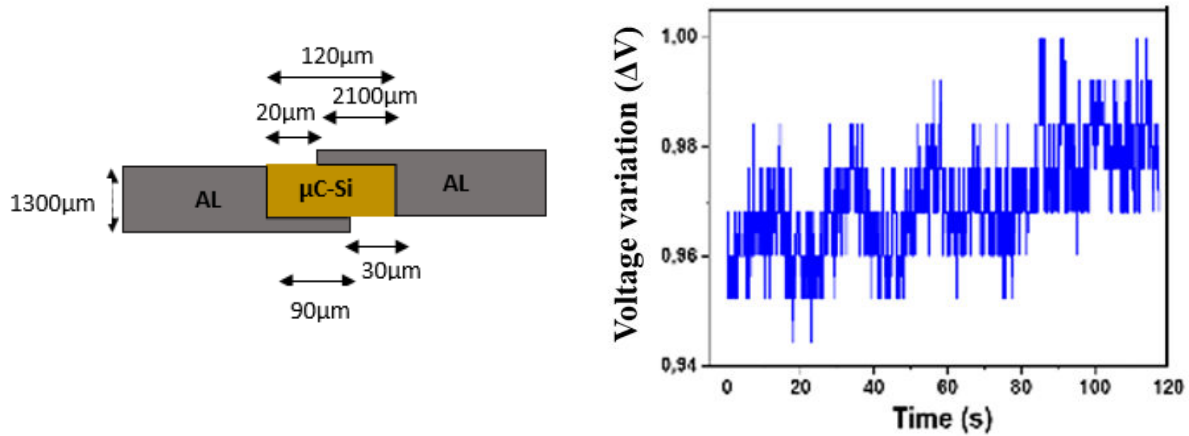


Figure 4.20. Structure design with electrodes configurations for current flow perpendicular and parallel to the strain.

Hence, between the three design electrodes configurations, the most appropriated corresponds to the design where the strain is parallel to the current flow, Figure 4.19 (b).

6.2 Geometry selection and dimensions

One time that the design of the electrodes configuration is selected, two different geometries are studied, square shape and ten resistances in parallel.

Figure 4.21 is formed by ten resistances in parallel, this design presents different dimensions that are shown in Table 4.2. However, due to the large length (L) and short width (W) it was impossible to obtain results as they were broken during the characterization, or they present a lot of cracks that can come from the handling during the fabrication process.

The only structure that works was for the dimensions $L=1000\text{ }\mu\text{m}$ and $W=100\text{ }\mu\text{m}$, which corresponds to the smallest. However, as shown in Figure 4.21, the voltage variation changes strongly during the characterization. This is due to the fact that the value of the resistance is formed by the equivalence of the ten resistances. The low value of the width (W) compared to the length (L) increases the resistance sensitivity but makes it too fragile during measurements.

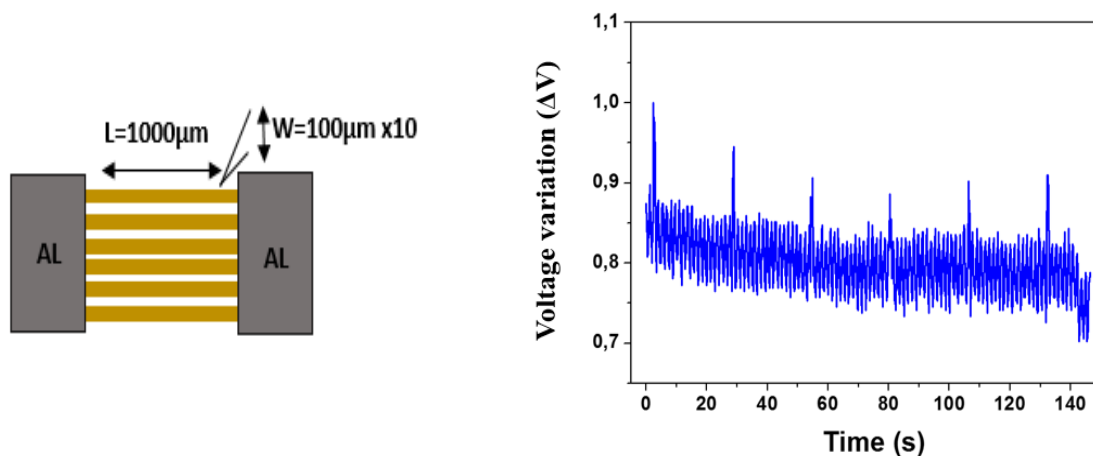


Figure 4.21. Structure of ten resistances in parallel its waveform applying signal of Figure 4.17.

An important disadvantage of this structure is that some of these resistances are broken during the measurement so that the voltage variation changes abruptly. Moreover, its response shows a drift that hinders the post-filtered signal treatment. This drift can be due to the drastic degradation of the structure. Hence, due to the low percentage of resistances that work, the short life-time and the accuracy, this structure is discarded such a reliable option. However, due to the interesting results obtained in the voltage variation, later it can be interesting to investigate the reliability of this shape using lower dimensions and fewer parallel resistances.

The last structure selected in this section is the square shape resistance using different dimensions ratio. For a strain gauge, the level of sensitivity is generally related to the resistance geometry and in particular to its length/width ratio, as shown in Figure 4.13. In our case, it was decided to study three different cases:

a) Ratio $L/W = 1$; with $L = 1000 \mu\text{m}$ and $W = 1000 \mu\text{m}$

Figure 4.22 shows the structure and its dimensions next to the graphic obtained. The waveform applied for its characterization is shown in Figure 4.17 and it consists in a pulse signal every 10 s, however as shown in Figure 4.22, the duration between two peaks is around 20 s. So, it seems that the structure is not able to react to all the stimuli applied presenting a poor response time. Moreover, the amplitudes of the peaks for the voltage variation are not the same. The average of this value corresponds to $\Delta V = 0.15 \text{ V}$ if it is not taken into account the stimuli not detected.

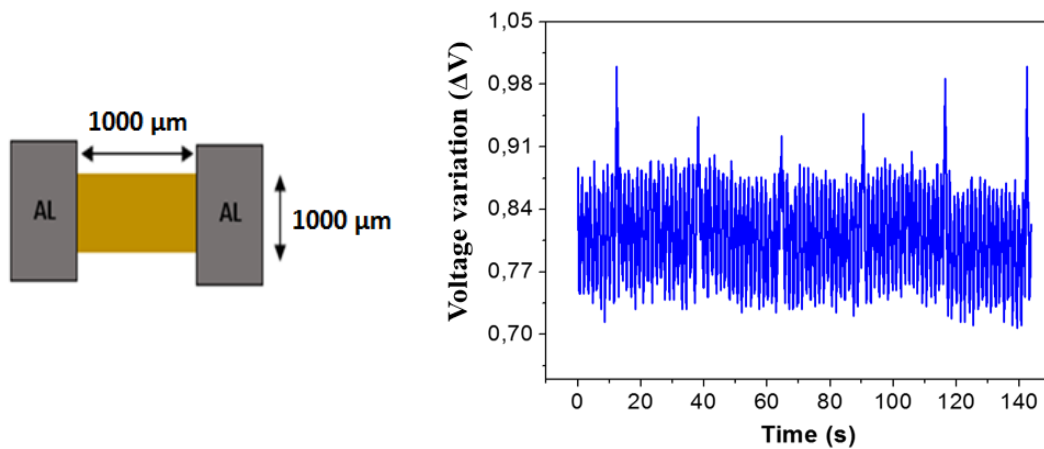


Figure 4.22. Study of square shape resistance when length (L) and width (W) have the same dimensions and it is applied the waveform of Figure 4.17.

The value of the voltage variation is relatively high but the fact that the structure is not able to react to all the stimuli is a big drawback. The frequency used between the pulses applied during its characterization is relatively low, 0.1 Hz, however for the targeted application the frequency want to be increased, at least until 0.2 Hz, and the structure should be able to react accurately to faster loading offloading cycles.

b) Ratio $L > W$: with $L=1500\ \mu\text{m}$ $W=1200\ \mu\text{m}$

For this case where the length (L) is bigger than the width (W), the structures for $L=4000\ \mu\text{m}$ $W=1000\ \mu\text{m}$ and $L=7000\ \mu\text{m}$ $W=1200\ \mu\text{m}$ were also analysed, however, these were broken during the characterization, and are automatically discarded.

Figure 4.23, shows the results obtained for the structure with $L=1500\ \mu\text{m}$ $W=1200\ \mu\text{m}$ where the ratio between length and width is practically the same as for the previous structure where $L/W=1$, however, by comparing the results obtained for the voltage variation, in Figure 4.22 it is around $\Delta V= 0.15\ \text{V}$ and for Figure 4.23, this is $\Delta V= 0.07\ \text{V}$.

The structure is able to react to signal waveform every 10 s but with different amplitude. This effect can come for a relative large length the global structure needs more time to react.

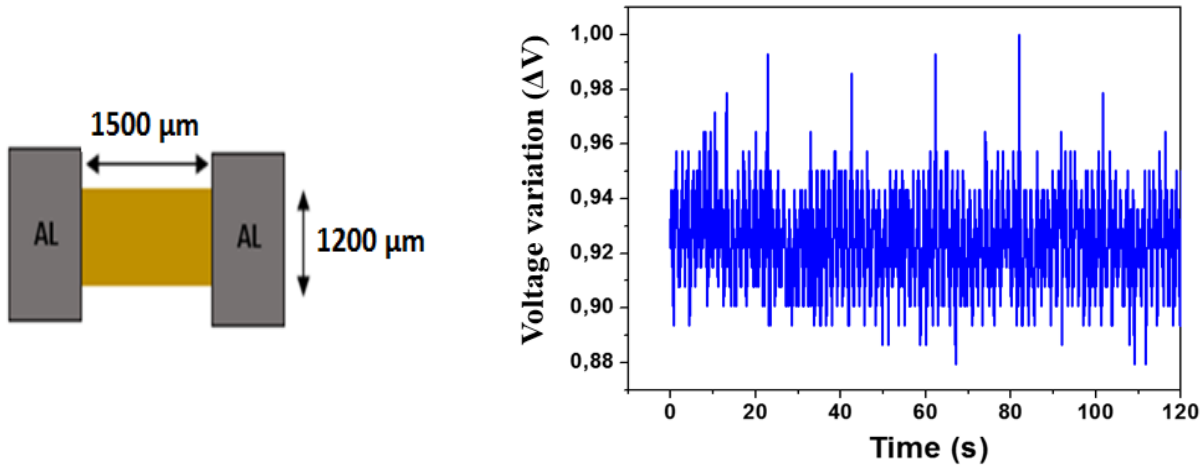


Figure 4.23. Study of rectangle shape when length (L) is higher than the width (W) with applied signal of Figure 4.17.

c) Ratio $L \ll W$ with $L=600\ \mu\text{m}$ $W=2000\ \mu\text{m}$

To finalize our study, it was decided to investigate the effect when the length (L) is smaller than the width (W). As shown in the graphic obtained in Figure 4.24. The sensor is able to react to all the applied stimuli, moreover, all peaks present similar amplitude values, $\Delta V= 0.07\ \text{V}$. This can be due to the fact that the low dimensions of the length help the intrinsic structure of the material to come back easily to initial state. Thus the structure reacted fast to all the applied having a good recovery and time response.

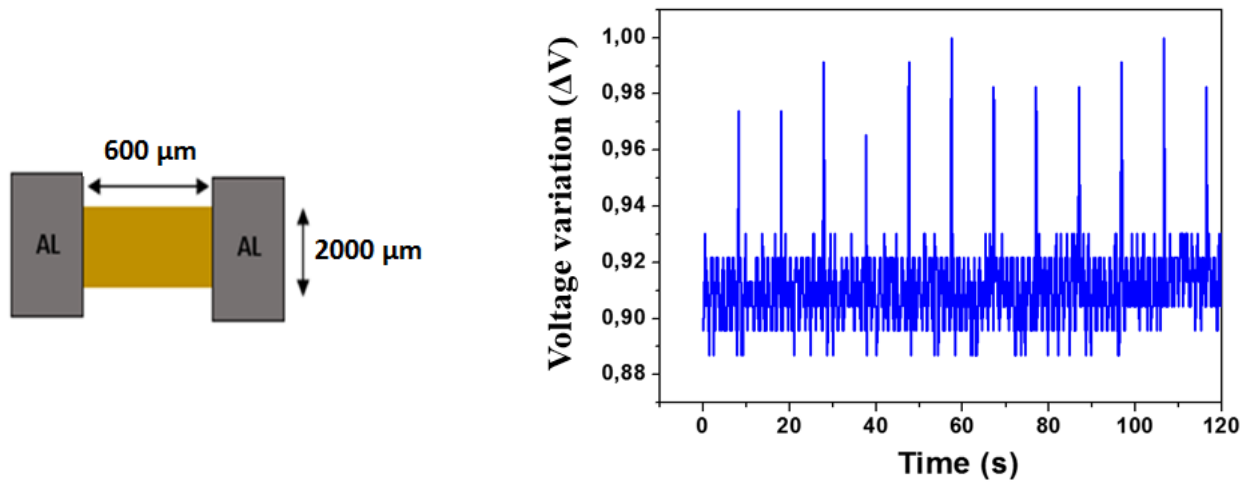


Figure 4.24. Study of rectangle shape when length (L) is lower than the width (W) with applied signal of Figure 4.17.

This sensor presents a good sensitivity and its ability to respect the frequency pulse of the signal of Figure 4.17, it was decided to verify if it also presents this ability to do it with more complex signals waveform such as ECG signal. The general shape of this signal is given in Figure 4.25. This wave presents a lot of small and tiny variations such as Q or S peaks. The frequency has been reduced to 0.025 Hz to see in detail if the device is able to follow exactly the shape of the applied signal, even for the small peaks variations. Results are shown in Figure 4.26 allows concluding that the sensor is able to detect a complex signal such ECG that it is formed by different shapes convolutions (pulses, sinusoidal, constant shape).

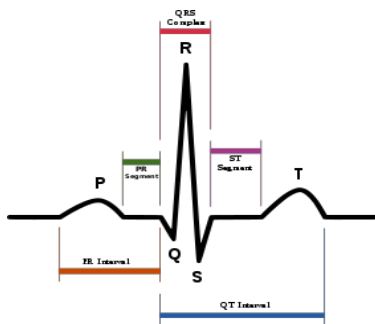


Figure 4.25. ECG waves.

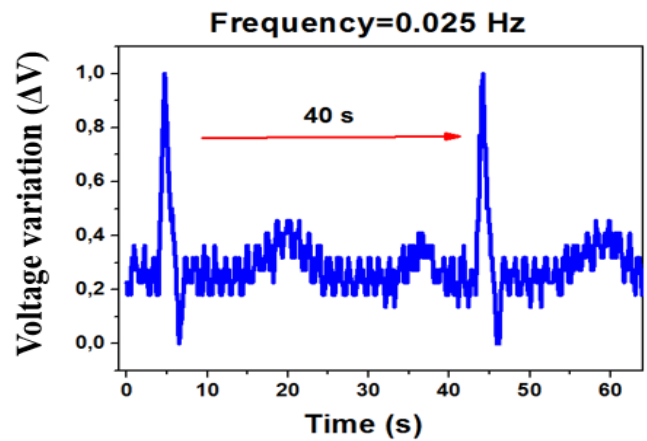


Figure 4.26. ECG waves obtained with structure of frequency = 0.025 Hz.

Afterward, it was tested if this shape is able to reproduce this complex shape when the frequency is increased until 0.2 Hz, the results appear in Figure 4.27. The ECG signal can be recognized, however, the accuracy is lower for this frequency, this can come from the ADC resolution of Arduino, 10 bits, which limits us to obtain more points during our acquisition.

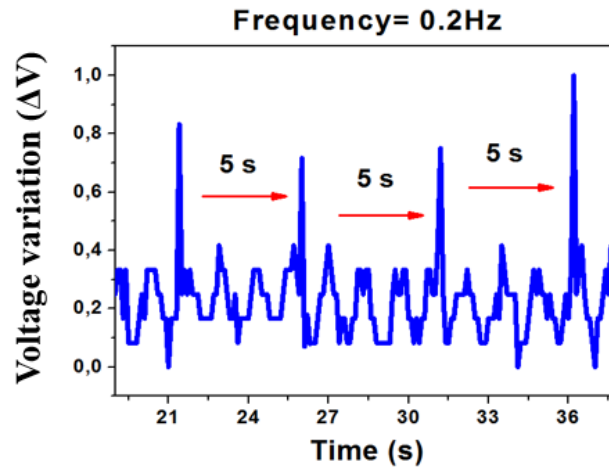


Figure 4.27. ECG waves obtained with structure of Figure 4.24 with frequency = 0.2Hz.

Hence, the structure of Figure 4.24 is able to react quickly, linearly and moreover also presents a good reliability, less drift and the data are more reproducible.

Along this part, various alternatives were studied to try to obtain which could be the interesting options to create a new mask design dedicated to the detection of fast and weak deformation signals. The highlighted points are commented below:

- For all the structure dimensions and sensor's shapes studied, the smallest dimensions are the more precise and with better reliability. The square shape with dimensions of $L=600\text{ }\mu\text{m}$ $W=2000\text{ }\mu\text{m}$ is the most accurate and it has good response and recovery time to follow different waves impulse at different frequencies.
- Another shape that can be interesting to study reducing the dimensions is that of square parallel shapes.

All of these considerations have been taken into account to create the new mask design presented below.

7. Design dedicated to detect weak dynamic signal

After studying the electrodes configuration, resistances shape, and the dimensions that present the better performance, it was decided to design a new mask more appropriated to detect weak, continuous and fast deformations. The design is shown on Figure 4.28. It is formed by a matrix of 5x5 resistances, 5 resistances in a straight line, and different shapes design such as rosette, serpentine or 5 resistances in parallel.

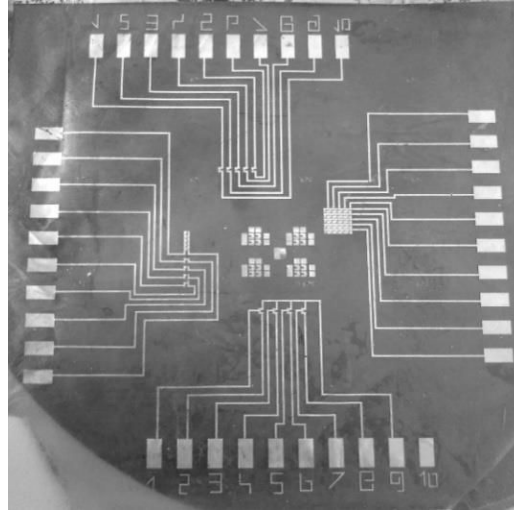


Figure 4.28. Last mask design with different structures and shapes.

Here the electrodes configuration is relatively far from the devices structure, as we try to avoid the effect of the deformation impulse on the electrical contacts and it will help us in the manipulation, during the characterization process.

The study of this mask is separated into several parts:

a) The first part is focussed on the study of the different strain gauge designs. For this purpose, the gauges are submitted to three different wave shapes (sinusoidal, square and triangle signals) with different pressures levels. A fatigue test is also presented to study the reliability of the device. One time that the most precise, accuracy and linear strain gauge design of this mask is selected, this is submitted to different tests such as sensitivity during continuous loading - offloading cycles.

b) The other part of this study is focused on the matrix. This is formed by 25 resistances in an area of 1x1 cm². For this structure, the resistance values are measured at the beginning and after

one hour of continuous loading - offloading cycles to verify if some degradation on their resistance value appears. Mapping is also performed for the sensitivity of the 25 resistances with a simple pulse and a frequency of 0.2 Hz. To finish this study, ECG stimulation tests are also realized on the matrix.

7.1 Mask shapes design

As was commented in the previous section, it appears that the design with smaller dimensions presents better performance under dynamic deformations. For that reason, on this mask, it was decided to test some new structures design but using a small dimension shape. The six different designs of the mask are presented in Figure 4.29.

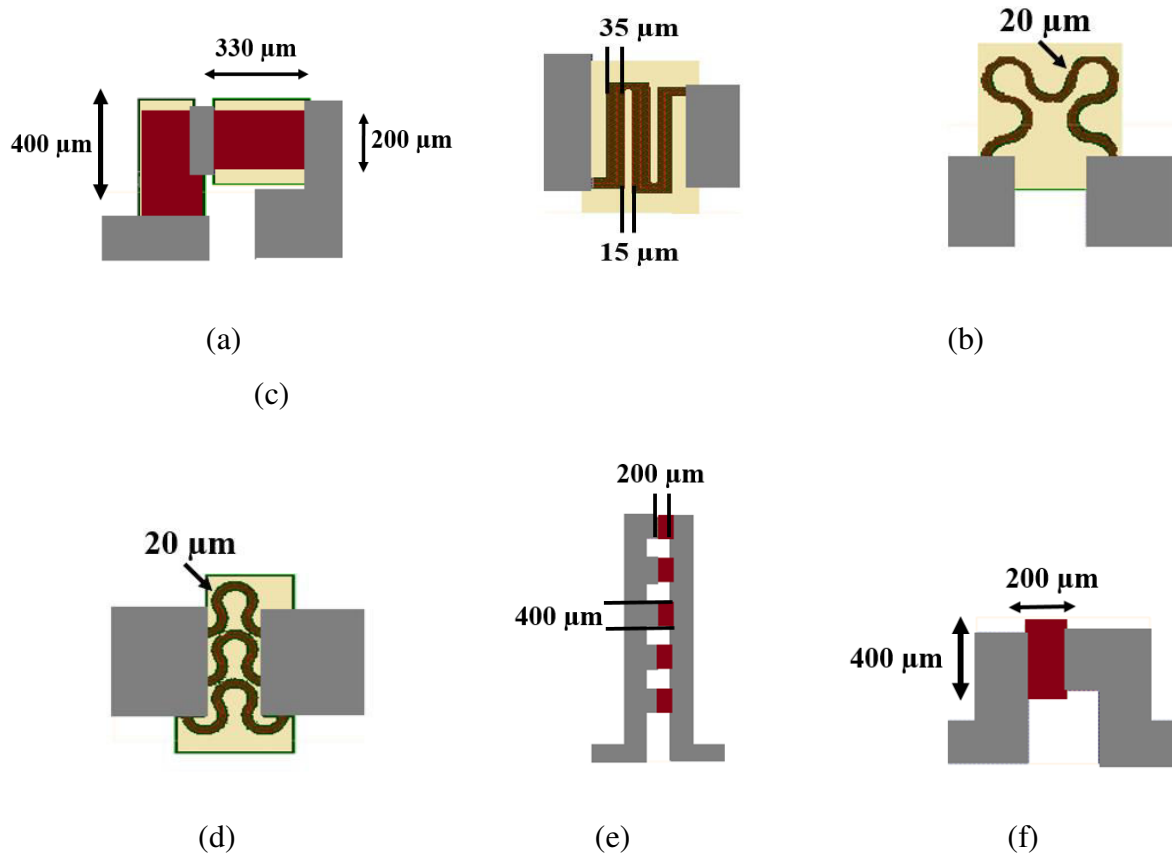


Figure 4.29. Shapes design for the mask presented in Figure 4.31 and dimensions: (a) Rosette shape, (b) U-shape, (c) simple serpentine shape, (d) three parallel serpentine shapes, (e) 5 resistances in parallel, (f) square shape.

The first structure, Figure 4.29 (a) corresponds to a biaxial rosette shape. The objective to fabricate this design is that, by using the strain gauge with a simple square shape, only the

deformation applied in one direction is measured. A strain gauge rosette, in our case, consists of two orientated resistances in a perpendicular direction, 90° . This design, composed of two or more closely positioned gauge, separated by with various orientations, is usual in the literature [12] and it allows to analyse unknown stress direction.

Serpentine shapes can also be used to increase the flexibility of inorganic materials when they are subjected to stretch or strain. They are also patterned in our mask, although this kind of shape is more dedicated to stretchable substrates. The designs consist of a U-shape with straight corners as shown in Figure 4.29 (b), a simple serpentine shape, Figure 4.29 (c), and three parallel serpentine shapes, Figure 4.29 (d).

Another structure present in the mask consists of 5 resistances in parallel, shown in Figure 4.29 (e). This design was also performed in the first mask design and it was observed that the voltage variation obtained with this structure is higher than the voltage variation obtained with the simple shape. However during this first study, due to the large dimensions of the length, these structures were more fragile, and it was difficult to obtain reproducible results. For this reason, for the design of this mask, the length has been considerably reduced.

Finally, the last simple shape present in this mask is a normal square resistance shape, shown in Figure 4.29 (f). It was decided to study the behaviour of the structures for different excitation waves and different pressure levels.

The characterization of the six resistances was performed at the same time and under the same characterization conditions. The applied waveforms consist of three different shapes with variable pressure levels as shown in Table 4.3, and for a frequency fixed at 0.2 Hz. The pressure variation makes reference to the difference between the maximum and the minimum pressure applied.

Signal applied	Pressure variation (ΔP)		
	$\Delta P= 100$ mbar	$\Delta P= 200$ mbar	$\Delta P= 400$ mbar
Sinusoidal waveform	$\Delta P= 100$ mbar	$\Delta P= 200$ mbar	$\Delta P= 400$ mbar
Square waveform	$\Delta P= 100$ mbar	$\Delta P= 200$ mbar	$\Delta P= 400$ mbar
Pulse waveform	$\Delta P= 100$ mbar	$\Delta P= 200$ mbar	$\Delta P= 400$ mbar

Table 4.3. Conditions used during the characterization of the different resistance shapes.

The goal of these applied signals is different: for the sinusoidal waveform, the pressure is gradually increased and decreased. However, for the square waveform, the pressure change abruptly but it is maintained in high or low state during a few seconds and for pulse wave, the structure is subjected to a strong variation of pressure in a short time.

With these different waveforms, it can be verified if the structures present the same recovery time and respond to different signals and amplitudes.

The results obtained for the waveform of each design are presented in the Annex. The signals, are filtered and the red line will correspond to the waveform obtained after using a filter conditioner step that consists of a low pass filter with a cut frequency of 27 Hz.

This is followed by commentary on the results obtained for the different design of Figure 4.29 and the conditions in Table 4.3

a) Rosette shape

Signals waveforms obtained for the different stimuli are presented in the Annex-a) Figure 4.30 (a), (b) and (c). Table 4.4 summarized the amplitude values obtained for the different waveforms, and for the different pressure levels. Figure 4.31 shows an example of the sensor of rosette shape obtained. During the fabrication process, it was found some problems to alignment the mask this come from the expansion and compression of Kapton®, and because the sensors are not positioned in the same area, around 4 cm of distance between them as shown Figure 4.28. This forced us to have certain mismatch to find a compromise between all the designs. This problem was contemplated during the design of the mask for that reason, as shown Figure 4.31 there is a certain margin to align the electrodes and the square shape of $\mu\text{c-Si}$.

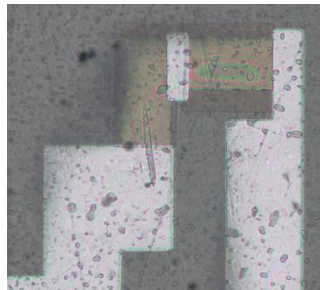


Figure 4.31. Example of the sensor obtain using the design of the rosette shape.

Here, the voltage variation obtained is the same for the same variation of pressure, and is independent of the signal shape applied (sinusoidal, square or pulse).

However, observing the results obtained when a pulse wave is applied, Annex-a) Figure 4.30 (c), the linearity or the drift of the signal is worst, especially in the case of $\Delta P = 100$ mbar, where it is 0.04 V.

	Voltage variation (ΔV)		
	$\Delta P = 100$ mbar	$\Delta P = 200$ mbar	$\Delta P = 400$ mbar
Sinusoidal wave	0.02 V	0.04 V	0.06 V
Square wave	0.02 V	0.04 V	0.06 V
Pulse wave	0.02 V	0.04 V	0.06 V

Table 4.4. Voltage variation for rosette structure applying the waveforms of Table 4.3

Rosette shape is able to reproduce the waveform of the signal applied and it reacts with the correct period to every 5 s without delay. However, the amplitude of the voltage variation is not very high even for the higher pressure variation, 400 mbar which value corresponds to 0.06 V.

b) U-Shape

This shape is the most popular shape of the commercial strain gauge. However as it can be observed in the graphics of Annex-b) Figure 4.32 (a), (b), (c), it is not able to reproduce the waveform applied and its values present a lot of instability, even with higher pressure variation, $\Delta P = 400$ mbar. Especially in the case of 100 mbar (Annex-b) Figure 4.32 (c)), to detect the pressure variation in the case of pulses, it was mandatory to use the filtered signal (red). Moreover, for this kind of design, all the graphics present a drift on its signal.

	Voltage variation (ΔV)		
	$\Delta P = 100$ mbar	$\Delta P = 200$ mbar	$\Delta P = 400$ mbar
Sinusoidal wave	0.02 V	Not reaction	0.08 V
Square wave	0.02 V	Not clear	0.08 V
Pulse wave	0.02 V	0.03 V	0.04 V

Table 4.5. Voltage variation for U-shape applying the waveforms of Table 4.3.

The poor results obtained with this shape can come from the bad definition of the shape obtained for this structure. Figure 4.33 shows the real shape obtained for this sensor. Here, it appears that it corresponds to square shape with holes in the edge of the structure. This bad definition can arise from the difficulties of work with the thin-film substrate, as explained in Chapter 2 and the low space between the grids, 15 μ m, whose dimensions are shown in Figure 4.29.



Figure 4.33 Real shape obtained for U-shape design the poor definition can be the origin of the bad behaviour show in Annex-Figure 4.32 (a), (b), (c)

c) Simple serpentine shape

This kind of shape is designed for stretchable substrates. However, it was decided to see its effect using our materials. As we can see in the different Annex-c) Figures 4.34 and in Table 4.6, the voltage variation is not very high and moreover, reacts practically with the same amplitude in front of different pressures. All the graphics obtained present a strong drift, especially the signal obtained for the simple pulse waves, in Annex-c) Figure 4.34 (c).

	Voltage variation (ΔV)		
	$\Delta P= 100$ mbar	$\Delta P= 200$ mbar	$\Delta P= 400$ mbar
Sinusoidal wave	0.02 V	0.03 V	0.04 V
Square wave	0.02 V	0.02 V	0.04 V
Pulse wave	Not appreciate	0.02 V	0.03 V

Table 4.6. Voltage variation for simple serpentine shape applying the waveforms of Table 4.3.

This structure does not present a high sensitivity to different pressure variations, as shown in Table 4.6. Therefore it will not an appropriate option to the targeted application but it presents a good shape definition after fabrication, Figure 4.35.



Figure 4.35 Serpentine shape design of one of our sensors. Width (W) of 20 μm .

d) Three serpentine shape in parallel

During the study of the simple serpentine shape, it was observed that the structure is able to replicate the waveform of the applied signal. However it presents practically the same variation of voltage for different levels of pressure. For that reason, it was decided to study the design of three serpentine shapes in parallel and see its influence on the sensitivity. By comparing the values of Tables 4.6 and 4.7, the values obtained for the parallel structure are higher. However, this voltage variation stays low such as for pulse waves with a pressure variation of 100 mbar, shown Annex-d) Figure 4.36 (c).

Figure 4.37 shows an example of our sensor using this design. For this structure it could be interesting to see its performance using a stretchable substrate.

	Voltage variation (ΔV)		
	$\Delta P = 100 \text{ mbar}$	$\Delta P = 200 \text{ mbar}$	$\Delta P = 400 \text{ mbar}$
Sinusoidal wave	0.02 V	0.04 V	0.06 V
Square wave	0.02 V	0.03 V	0.06 V
Pulse wave	Not clear	0.03 V	0.04 V

Table 4.7. Voltage variation for three serpentine shape in parallel structure for different waves and pressure variations.

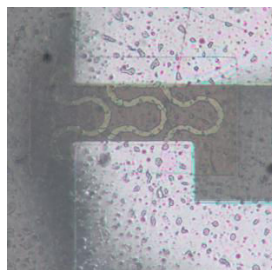


Figure 4.37 Three serpentine shape in parallel design of one of our sensors. Width (W) of 20 μm .

e) Five resistances in parallel.

The results obtained for this structure are summarized on Table 4.8 and the waveforms obtained are presented in the Annex-e) Figure 4.38. There are some important points to remark for this structure. As it was commented in previous points, in the design of the first mask, this structure was tested with different dimensions. However, due to the high length, it was practically impossible to obtain some reliable results due to its fragility. For this design, the area of $\mu\text{c-Si}$ is reduced and the devices do not present cracks problems. We can see that its reaction for different stimulus waves is considerably better than the other tested structures.

	Voltage variation (ΔV)		
	$\Delta P= 100 \text{ mbar}$	$\Delta P= 200 \text{ mbar}$	$\Delta P= 400 \text{ mbar}$
Sinusoidal wave	0.04 V	0.10 V	0.40 V
Square wave	0.04 V	0.24 V	0.40 V
Pulse wave	0.03 V	0.08 V	0.40 V

Table 4.8. Voltage variation for five resistances in parallel applying the waveforms of Table 4.3.

If we analyse the results obtained in Table 4.8, the values obtained for the voltage variation are higher than for the rest of the structures studied. Therefore this geometry design presents a better amplitude response than the rest, later it will be studied deeper through fatigue test.

f) Square shape

The last shape analyzed in this section corresponds to the square strain gauge design. Observing the values obtained in Table 4.9 and the shapes of the graphics of Annex-f) Figure 4.39 (a), (b), (c), it is demonstrated that between the different shapes studied, this design is the most precise and robust. The voltage variation follows an increment of 0.05 V when the variation of pressure is incremented. Moreover, for this design, the signals obtained are very linear and the sensor is more special integrated than the 5 resistance in parallel.

	Voltage variation (ΔV)		
	$\Delta P= 100$ mbar	$\Delta P= 200$ mbar	$\Delta P= 400$ mbar
Sinusoidal wave	0.10 V	0.15 V	0.30 V
Square wave	0.10 V	0.15 V	0.25 V
Pulse wave	0.10 V	0.15 V	0.30 V

Table 4.9. Voltage variation for square shape resistance applying the waveforms of Table 4.3.

Therefore between all the shapes studied for this mask it can highlight that if it is taking into account the linearity, the reproduction of the shape of the signal applied and the voltage variation for different pressure levels, the sensor shape with the best reliability corresponds to the square structure and the design of 5 resistances in parallel because it reacts with good amplitude and waveform to the different waves.

It is important to comment that for all the structures, it has been verified that the frequency of the waves is the same as the signal applied. For the next test, it was decided to see the effect in the behaviour when they are submitted to a loading offloading tests to see their performances in front of continuous deformations.

7.2 Loading-offloading cycles test

Due to the relative rigidity of microcrystalline silicon, it suffers from cyclic instability, during which buckling, cracking and even stripping often appear after numerous cycles. For that reason, to verify cyclic stability, the sensor was submitted to periodic endurance loading-offloading cycles. A fatigue test was performed for 15 min to verify if some degradation appears in the amplitude of the pulse detection and in the linearity of the sensor.

All the structures were submitted to a pulse wave of 200 mbar of pressure variation and the frequency of the pulses are 0.2 Hz. In Table 4.10 there are summarized all the values obtained for the amplitude of the pulse and the drift.

	Initial value	After 5 min	After 10 min	After 15min	Drift
Rosette shape	0.04 V	0.04 V	0.04 V	0.04 V	0.22 V
U-Shape	Not appreciate	Not appreciate	Not appreciate	Not appreciate	1.3 V
Simple serpentine shape	0.02 V	Not appreciate	Not appreciate	Not appreciate	0.3 V
Serpentine shape in parallel	0.03 V	0.02 V	0.02 V	0.02 V	0.25 V
Five parallel resistances	0.06 V	0.04 V	0.02 V	0.02 V	0.08 V
Square shape	0.15 V	0.15 V	0.15 V	0.15 V	0.05 V

Table 4.10 Voltage variation produced after a fatigue test of 15 minutes.

The graphics obtained for each structure during the loading offloading are shown in the Annex g) Figure 4.40. These curves show that the structures suffer from a drift that changes the level of the signal. For the structures of U-shape and simple serpentine shape, they were not able to react to the stimuli applied, moreover its degradation of the baseline or drift is really high.

For rosette shape, the amplitude of the voltage in front of the applied stimuli is constant during the 15 minutes of fatigue test and the drift of the signal corresponds is not very high, 0.2 V. However the main problem of this structure is its poor sensitivity obtained to the pressure detection, the voltage variation detected corresponds to 0.04 V. This is the same problem that presents the serpentine shape in parallel which voltage variation is 0.02 V.

Therefore, as demonstrated during the study of different waveforms and pressure the designs, the most appropriated for the targeted application are the structure with 5 resistances in parallel and the square shape. However, as shown in Table 4.10, the structure of 5 resistances in parallel suffers from a deterioration in its sensitivity, varying the amplitude of the detected signal, after 5 minutes of fatigue test from 0.06V at the beginning of the test and with a value of 0.02 V at the end.

The square shape is the structure that suffers less degradation in the linearity and in the sensitivity, because the amplitude of the response is always equal to 0.15 V, moreover it presents the lowest drift value, 0.05 V. Figure 4.41 shows the results obtained for square shape after a loading offloading test.

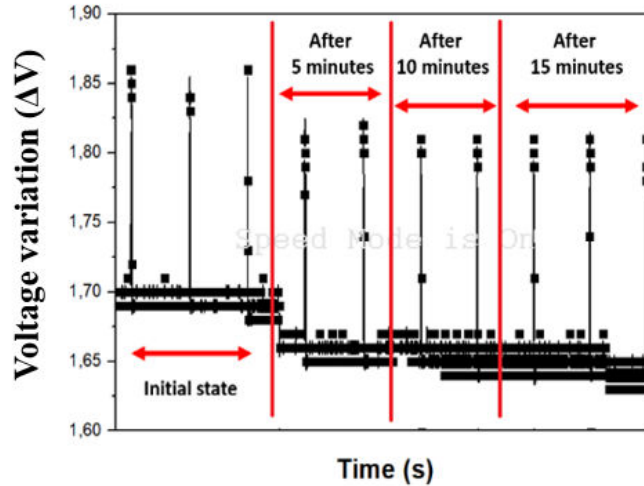


Figure 4.41. Loading –offloading test realized during 15 minutes for square shape

For that reason, in the next section, using the same dimensions it will be test its reaction when this shape is used to form a matrix of 25 sensors. But before the matrix construction, it was decided to see if there are some effects in the amplitude of the voltage detection if the structure is reversed, sticking $\mu\text{c-Si}$ to the membrane. We expected that the structure reacts in the same way independent if the pressure is applied at the top or bottom of the structure. This study is presented below.

7.3 Mechanical behaviour of square structure- life cycle.

The electrodes in the mask presented in Figure 4.29 were design to be far from the structure of the device. This offers us some flexibility to choose other position possibilities. For that reason to study the mechanical behaviour of the square structure, it was decided to reverse the structure and stick the sensor directly onto the membrane. As the structure is reversed, the deformations will be seen now such as compressive pulses.

Figure 4.42 shows the voltage variation when the sensor is submitted to a pulse waveform of 0.2 Hz using different pressure amplitudes during 10 minutes. The initial amplitude of pressure applied is 200 mbar later this is increment to 400 mbar and 600 mbar. After that, the cycle is repeated. The sensor reacts with approximately the same variation of voltage during the first and the second loading - offloading cycle.

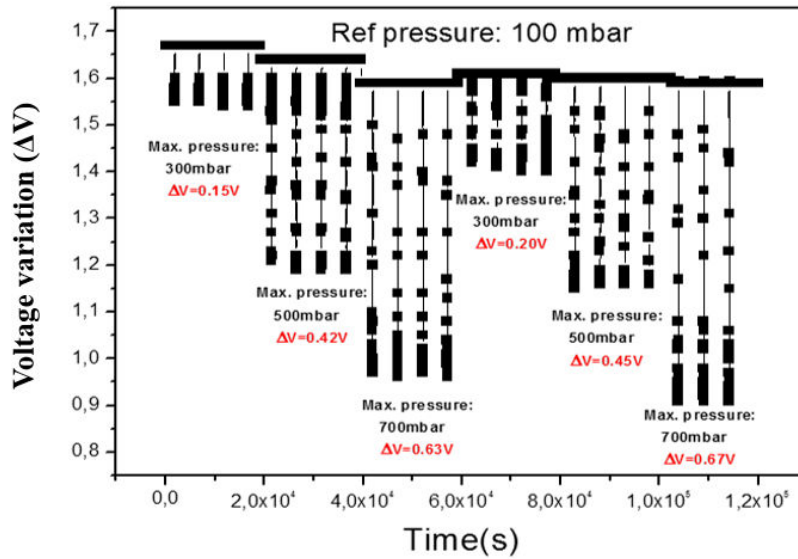


Figure 4.42. Fatigue test of pulse waves of 0.2Hz of frequency during 120 cycle for variable pressure.

There is drift in the voltage of 0.1 V during the second cycle, especially with a pressure variation of 200mbar, this can come from the cracks produced in the structure when this is submitted to the higher pressure variation of 600 mbar.

Moreover, if it is compared the results of Table 4.9 and Figure 4.42, the values obtained for the voltage variations are the same independent if the pressure is applied in the top or the bottom of the structure, around 0.15 V for variation of pressure of 200 mbar and 0.30 V for 400 mbar. This offers us the possibility to use this structure in both senses

8. Matrix characterization

8.1 Design and objective

The main motivation to design flexible sensor matrices is to measure the pressure distribution in an area. The principal limitation of the previous structures is that, according to their design, the deformation can be measure only in a punctual place instead of an area. Depending on the application, it is not easy to verify which part corresponds to the point of the maximum deformation applied. For that reason, with the design of our matrices, the size of the individual strain gauge has been decreased to cover a square area. It is then possible to obtain larger integration densities of sensors and thus to increase the spatial resolutions in a small area. Moreover, the advantage of the array or matrix construction is that it requires fewer connections.

The intersection between each row and each column corresponds to the electrodes of each sensor. So a 5 by 5 matrix is formed by 25 sensing nodes while only needing 5 connections. However, the main challenge during matrix characterization is that this kind of design is prone to parasitic crosstalk or "ghosting", this means that the electrical readings for inactivated nodes can be affected when pressure is applied on one node or on multiple nodes. Pressure matrices can be fabricated also using capacitive sensors, however in our case it was decided to use piezoresistive sensors, as in comparison to other technology, they require a less complex data acquisition system, and that moreover they are less sensitive to electromagnetic noise [13].

The design of our matrix is formed by 25 resistances in an area of $1 \times 1 \text{ cm}^2$. Each resistances have the same dimensions as the square shape, $L=200 \text{ }\mu\text{m}$, and $W=600 \text{ }\mu\text{m}$, with this we expected to obtain more or less the same voltage variation or sensitivity to the deformation for all the sensors and good homogeneity. Figure 4.43 shows the design of the matrix.

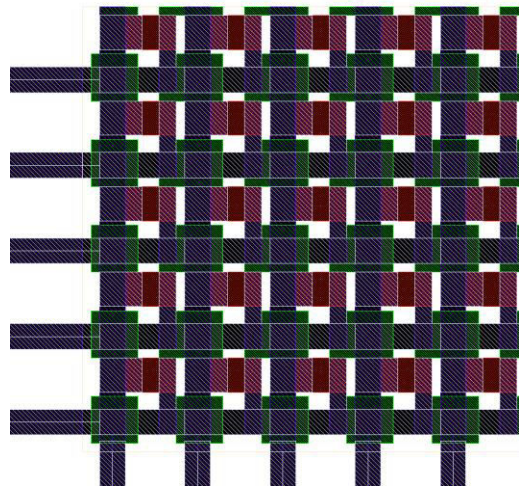


Figure 4.43 Layout of our matrix design formed by 25 resistance using a square shape with $L=200 \text{ }\mu\text{m}$, and $W=600 \text{ }\mu\text{m}$

The resistance across each node was measured before deformations and was within a range of $18 \text{ k}\Omega \pm 3 \text{ k}\Omega$. However, this value varies a little during its manipulation for characterization, (sticking on the membrane, electrodes connection, can create some cracks in the structure that increase the resistance value).

Unfortunately due to time limitation, complexity and requirement necessary to perform a good characterization system of a matrix, it was not possible to develop a new data acquisition and visualization system dedicated to this characterization, so for that reason this was firstly made

manually. However, one of the advantages to do it manually it is that it avoids cross-talking effect within the individual elements of the matrix.

To perform the manual characterization, the matrix was submitted to continuous deformations while the acquisition was elaborated by modifying the node connection.

8.2 Matrix amplitude response to dynamic pulse

The first characterization consists in submitting our matrix to a continuous pulses wave deformation. The signal presents a pressure variation of 200 mbar and the frequency between each pulse is 0.2 Hz. Figure 4.44 presents the colour mapping obtain after measuring the voltage variation of the reaction. The voltage variation when the pulse is applied is written on each cell, and the average value of the mapping is 0.11 ± 0.03 V.

The maximum value obtained corresponds to 0.15 V and the minimum is 0.08 V. In comparison with the results obtained in the voltage variation of the square sensor with the same wave applied (Table 4.9), which corresponds to 0.15 V the average of the matrix, 0.11 ± 0.03 V, is close from this value. The worst value of the voltage variation in the matrix corresponds to the sensors placed in the corners. However this is logical because those places correspond to the areas that are relatively far from the impulse centre. Additional to the colour mapping, in the annex adds the signal wave shape of the 25 sensors.

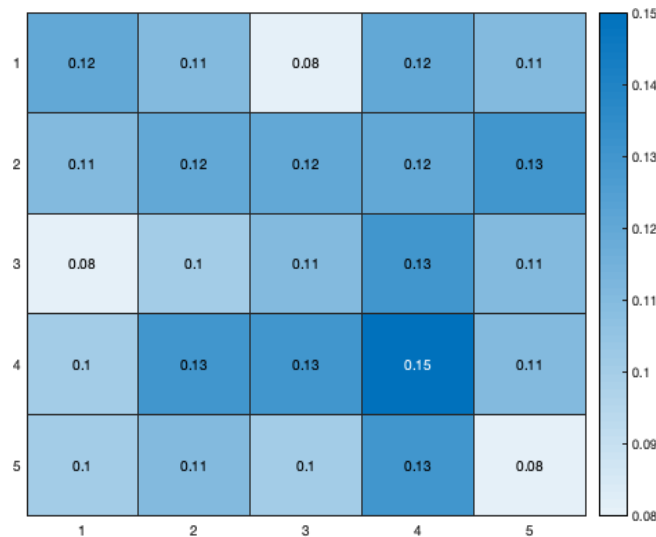


Figure 4.44. Voltage variation (V) obtained when the matrix is submitted to a pulse waveform of 200 mbar pressure variation and pulse frequency of 0.2 Hz.

For our goal, not only the sensitivity of the sensors is relevant, it is also important that it presents the ability to reproduce exactly the applied waveform because it offers us the possibility to use them in applications where the amplitude of the signal is less relevant or can be amplified with post-treatment. In the Annex h) Figure 4.45 shows the mapping waveform of the matrix when it is submitted to a pulse wave of 200 mbar of pressure variation using pulses frequency of 0.2 Hz

8.2 Matrix reaction to a complex waveform such as ECG signal

Here, the ECG signal is applied using pulse of 0.2 Hz of frequency with a maximum of pressure variation of 400 mbar. This value corresponds to the higher peak of the signal and in the matrix it has a value of 0.20 ± 0.05 V. This signal is interesting for its complexity because it is in fact composed of different shape signals as sinusoid, pulse and linear parts. Figure 4.46 shows that the 25 sensors are able to react fast to the different pressure and shapes that compound this signal and reproduce them. It offers then the possibility to use the matrix from different applications by using an appropriate acquisition system.

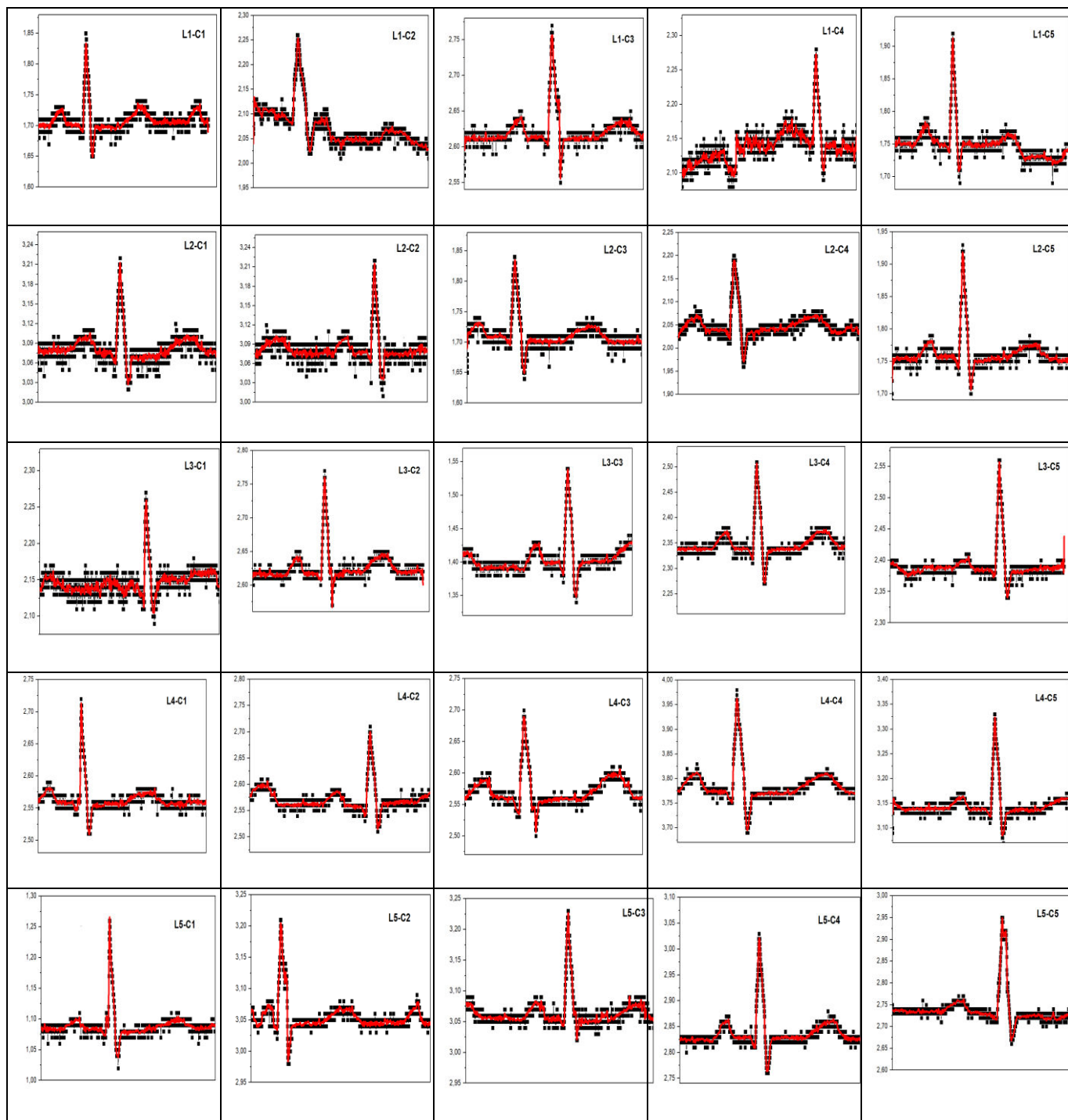


Figure 4.46. ECG signal mapping obtain using a frequency of 0.2 Hz and a maximum pressure variation of 400 mbar.

8.3 Matrix reliability

To verify the reliability of the matrix, it was decided to measure the relative variation of its resistance value after a loading offloading test of 1 hour and a half. With this test, it is possible to verify the degradation percentage presented after a continuous cycling deformations.

To calculate it, the resistances value is measured at the beginning and at the end of the test and the values that appear in the graphic of Figure 4.47 corresponds to the percentage of this variation.

Here it is observed that the degradation of the resistance is worst in the right corner it can come from this part corresponding to the electrical wires. Here the current is higher and the resistance suffers from a faster degradation.

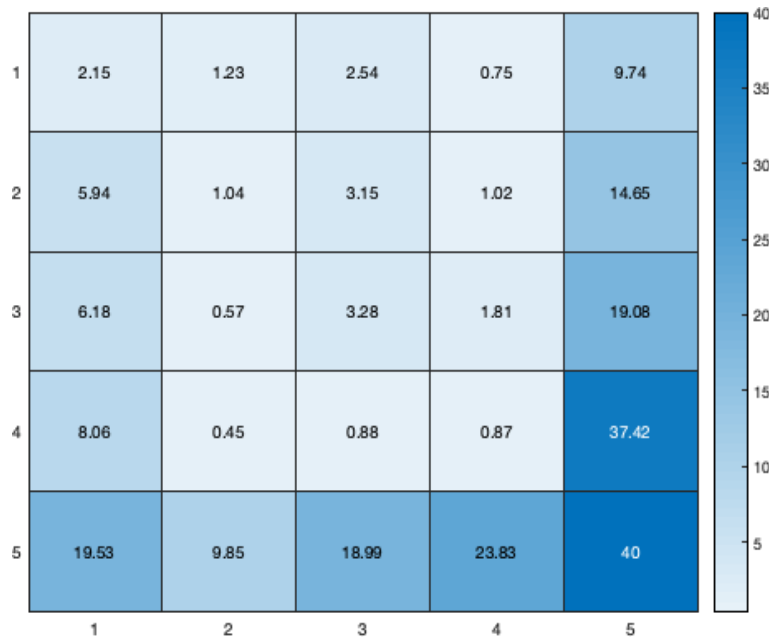


Figure 4.47. Relative variation of the resistance (%) after loading offloading test performed during 1 hour and half.

Therefore if it is compared to the matrix performance, with the single square structure, it is more or less the same, both react with similar amplitude to the same signal applied, around 0.15 V and are able to reproduce complex waveforms such as ECG signal.

However, the matrix presents advantages such as offers us at the same time the electrical measurement of 25 different sensors in an area of 1x1 cm². This is interesting to know which area

corresponds to the higher deformation with it is increased the spatial resolutions and it is possible to make an average of the signal amplitude to obtain more accurate results, another advantage of this is possible to obtain larger integration densities in a small area, reducing the fabrication cost and the connections necessary are reduced with this kind of design.

9. Conclusion

Throughout this chapter, we describe the steps followed to create our own home-made acquisition system to perform dynamic measurements. Different structures and designs have been studied to try to find which one can be more appropriate to our objective.

During this study, it was concluded that not only the flexibility of the materials affects the accuracy and operation of the sensors; the use of appropriate design can increase the sensitivity and linearity of them.

The electrodes position when the deformation is applied determines the direction of the current flow. During our study, it was observed that when the deformation is parallel to the current flow, the values obtained are more precise and there is no significant deviation.

In addition, different designs of structures with different dimensions were studied. Here it was concluded that between all of them, the small dimensions for a square design are the most robust and will help the global structure to return easily to its value initial.

In the last part, the mechanical and electrical behavior of a matrix of 25 resistances was studied. Its design is based on the dimension of the square shape and the results obtained for both structures to different fatigue tests an amplitude detection were similar. However, the matrix present important advantages against to the simple structure designs such as its large integration densities in a small area, or the possibility to reduce the fabrication cost and the connections necessary in this kind of design make it a good candidate to be used for measure weak and dynamic deformation in a small area.

10. Annex

a) Figure 4.30 Rosette shape- waveforms obtain with conditions Table 4.3

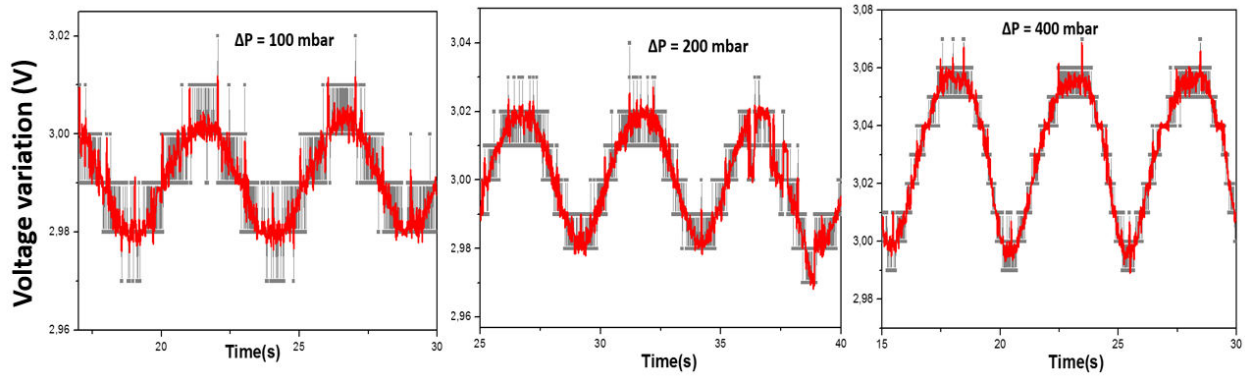


Figure 4.30 (a). Voltage variation for different pressure variations of 100 mbar, 200 mbar, 400 mbar when a sinusoidal wave is applied for rosette shape.

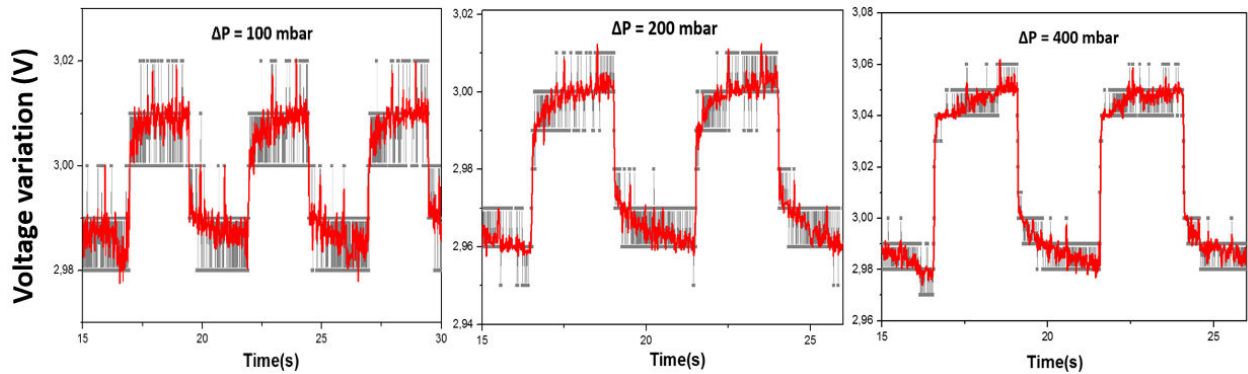


Figure 4.30 (b). Voltage variation for different pressure variations of 100 mbar, 200 mbar, 400 mbar when a square wave is applied for rosette shape.

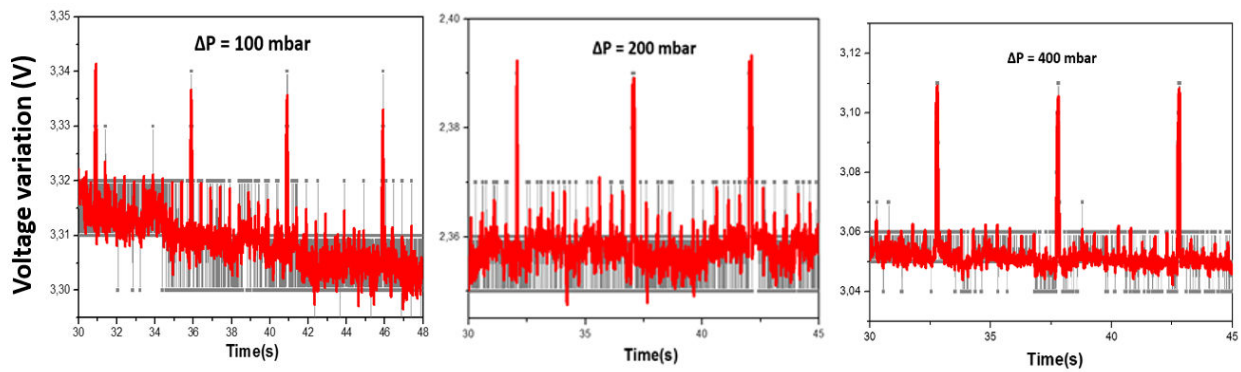


Figure 4.30 (c) Voltage variation for different pressure variations of 100 mbar, 200 mbar, 400 mbar when a sinusoidal wave is applied for rosette shape.

c) Figure 4.32 U-shape- waveforms obtain with conditions Table 4.3

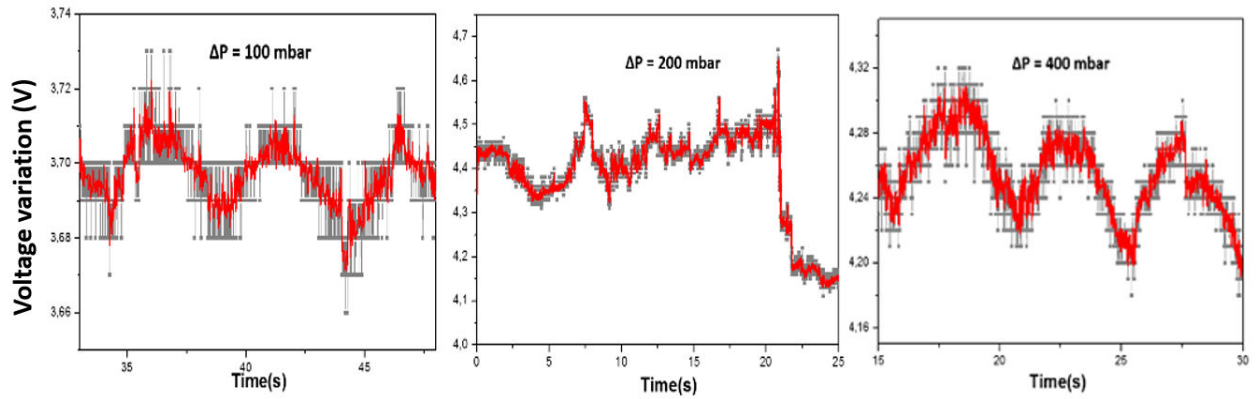


Figure 4.32 (a). Voltage variation for different pressure variation of 100 mbar, 200 mbar, 400 mbar when a sinusoidal wave is applied for U-shape.

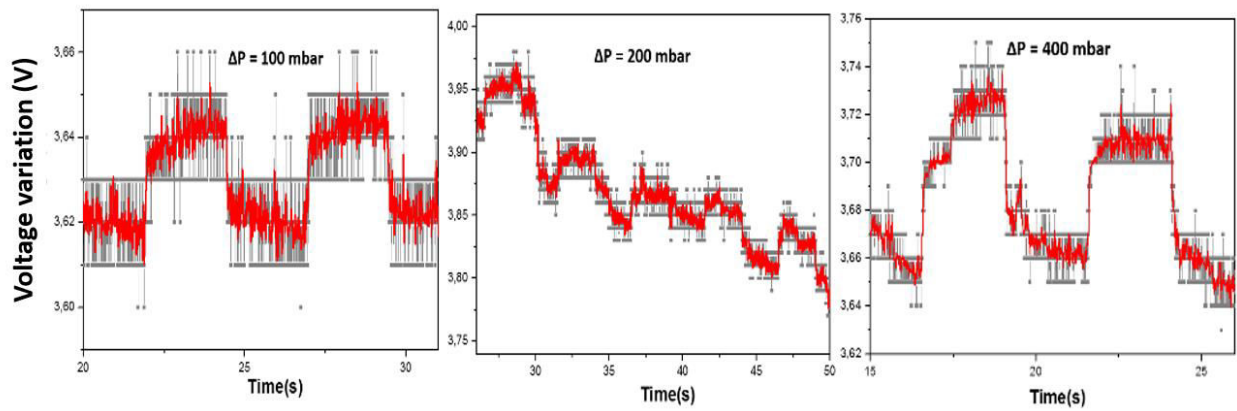


Figure 4.32 (b). Voltage variation for different pressure variation of 100 mbar, 200 mbar, 400 mbar when a square wave is applied for U-shape.

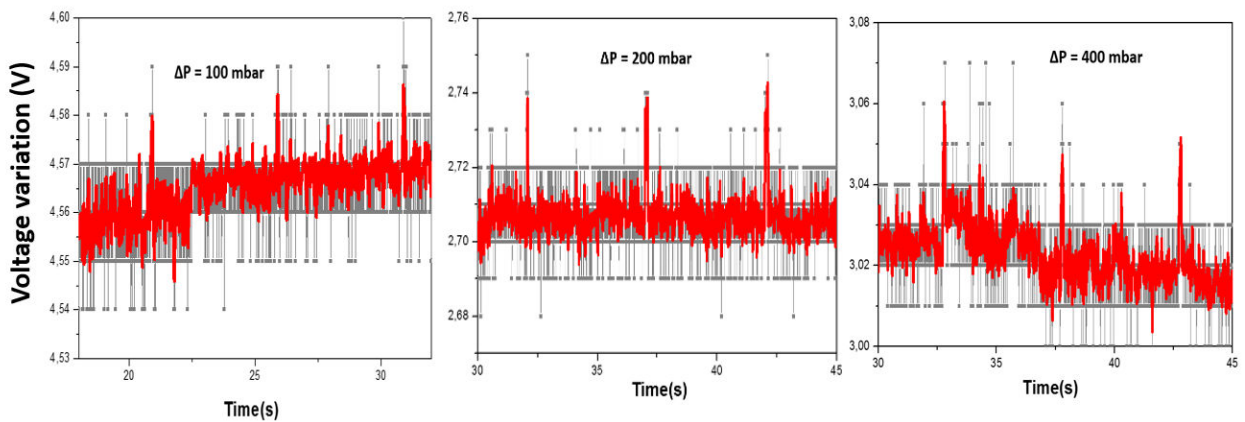


Figure 4.32 (c). Voltage variation for different pressure variation of 100 mbar, 200 mbar, 400 mbar when a pulse wave is applied for U-shape.

d) **Figure 4.34 Serpentine shape- waveforms obtain with conditions Table 4.3**

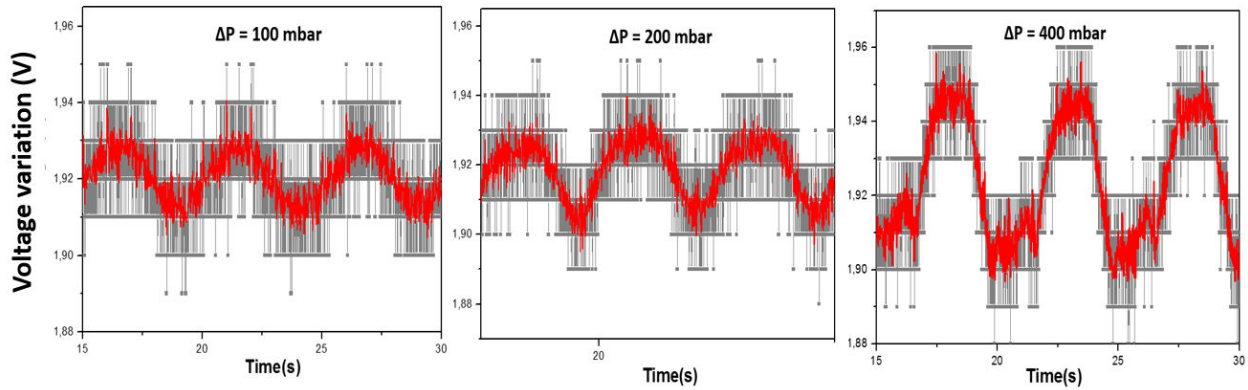


Figure 4.34 (a). Voltage variation for different pressure variation of 100 mbar, 200 mbar, 400 mbar when a sinusoidal wave is applied for serpentine shape.

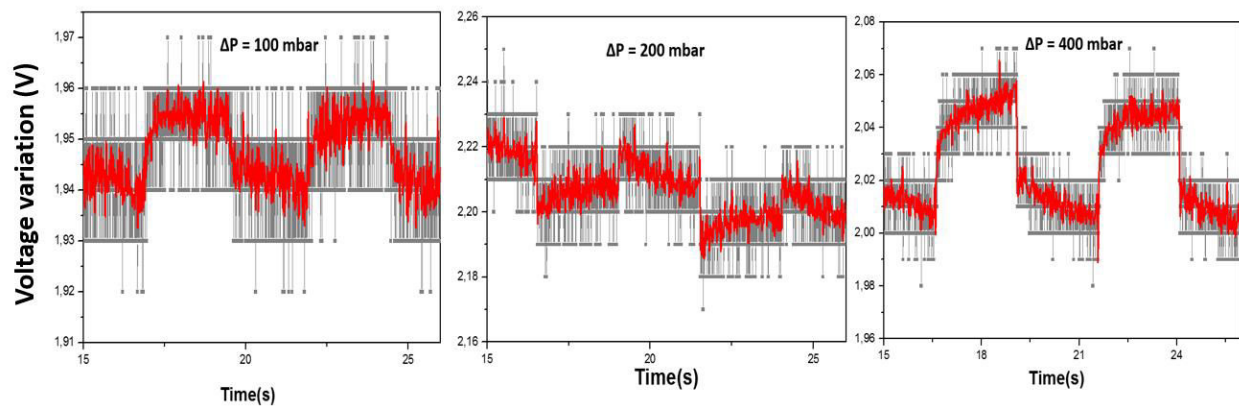


Figure 4.34. (b). Voltage variation for different pressure variation of 100 mbar, 200 mbar, 400 mbar when a square wave is applied for serpentine shape.

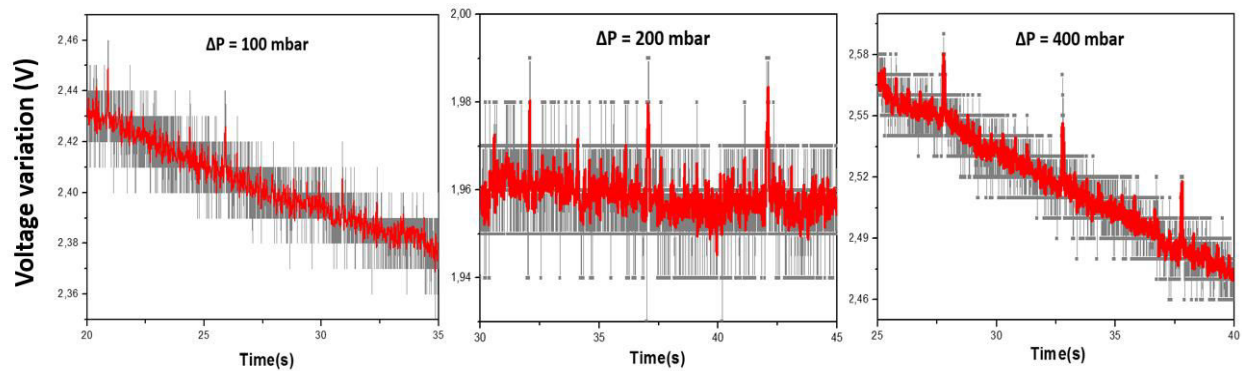


Figure 4.34 (c). Voltage variation for different pressure variation of 100 mbar, 200 mbar, 400 mbar when a pulse wave is applied for serpentine shape.

e) **Figure 4.36 Three serpentine shape in parallel- waveforms obtain with conditions Table 4.3**

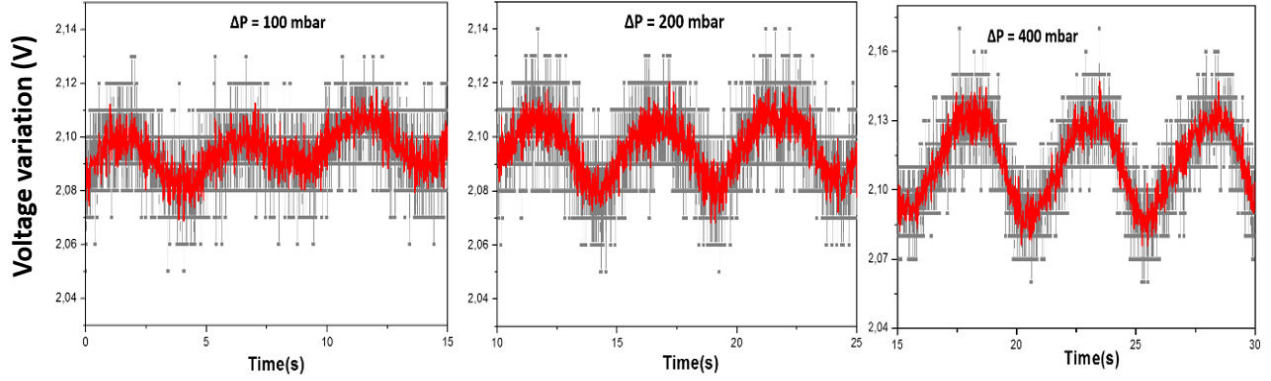


Figure 4.36 (a). Voltage variation for different pressure variation of 100 mbar, 200 mbar, 400 mbar when a sinusoidal wave is applied for three serpentine shape.

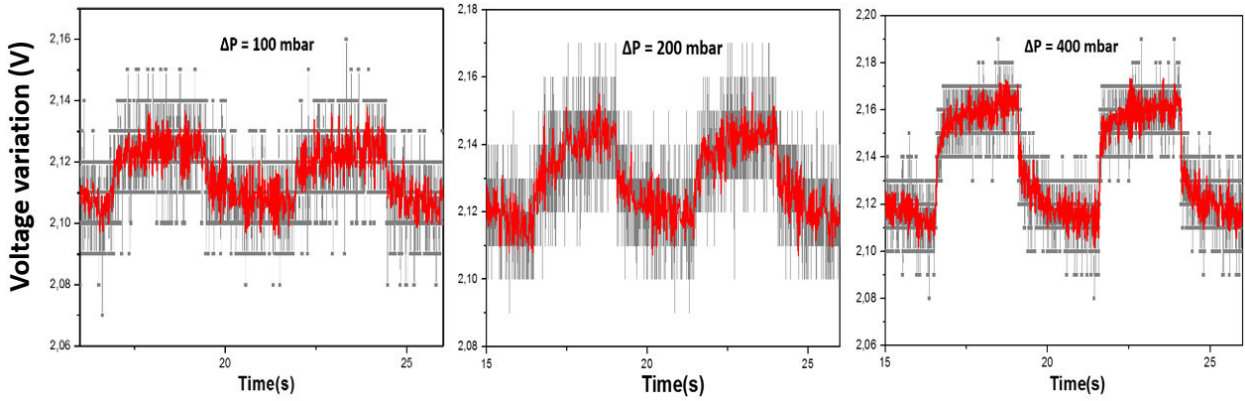


Figure 4.36 (b). Voltage variation for different pressure variation of 100 mbar, 200 mbar, 400 mbar when a square wave is applied for three serpentine shape

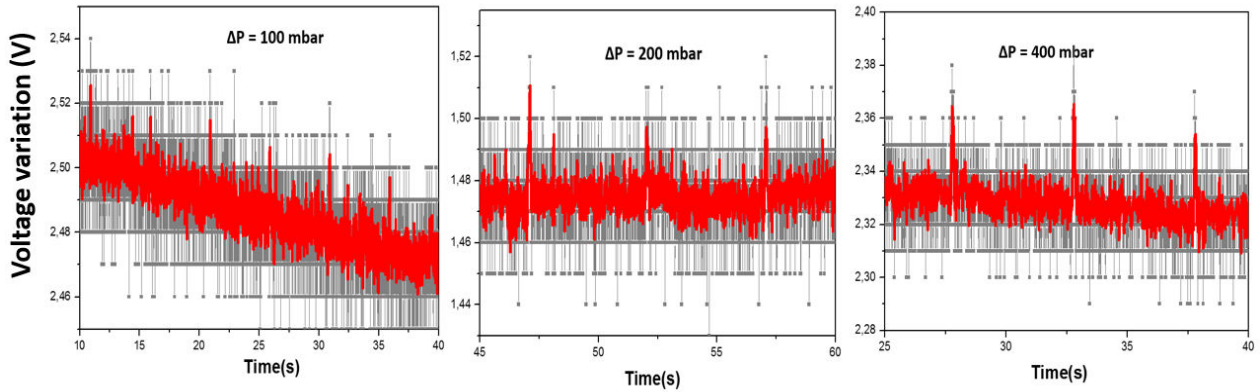


Figure 4.36 (c). Voltage variation for different pressure variation of 100 mbar, 200 mbar, 400 mbar when a pulse wave is applied for three serpentine shape.

f) **Figure 4.38 Five resistances in parallel - waveforms obtain with conditions Table 4.3**

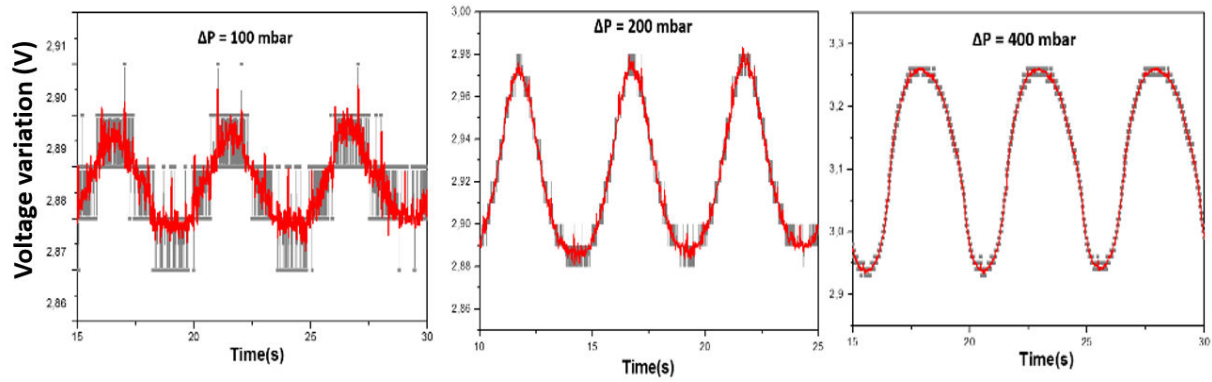


Figure 4.38 (a). Voltage variation for different pressure variation of 100 mbar, 200 mbar, 400 mbar when a sinusoidal wave is applied for 5 resistances in parallel.

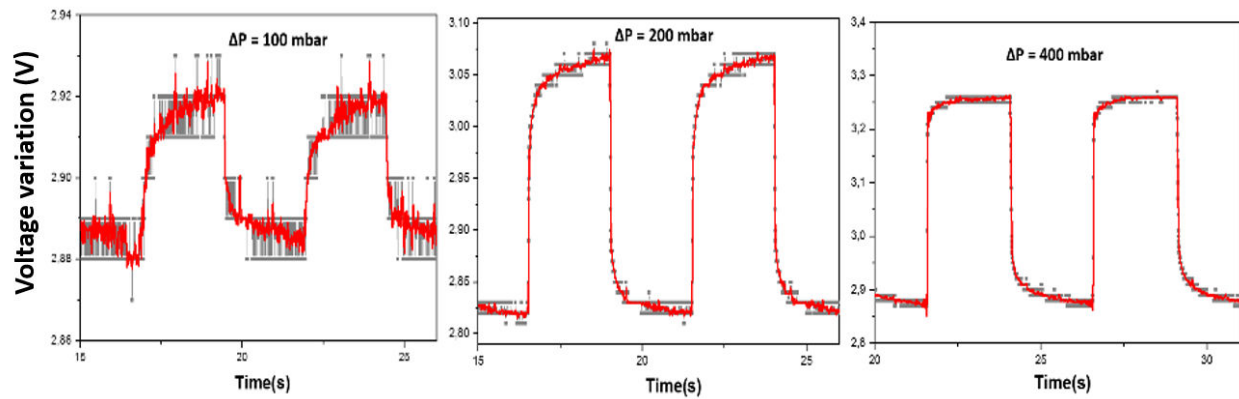


Figure 4.38 (b). Voltage variation for different pressure variation of 100 mbar, 200 mbar, 400 mbar when a square wave is applied for 5 resistances in parallel.

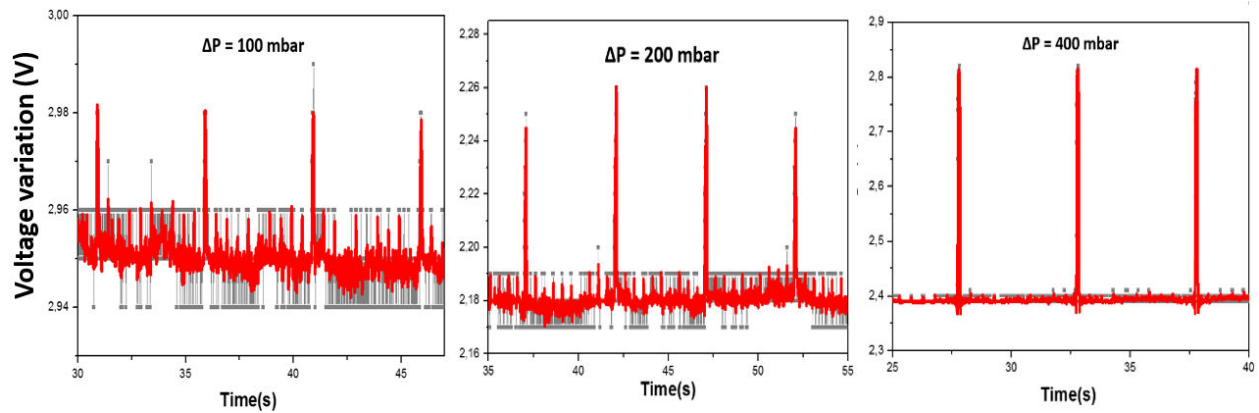


Figure 4.38 (c). Voltage variation for different pressure variation of 100 mbar, 200 mbar, 400 mbar when a pulse wave is applied for 5 resistances in parallel.

g) **Figure 4.39 Square shape resistance - waveforms obtain with conditions Table 4.3**

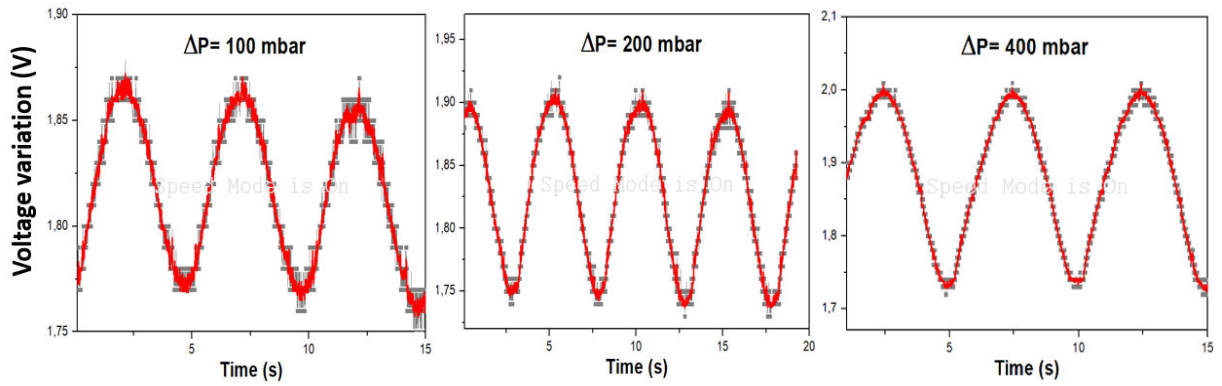


Figure 4.39 (a). Voltage variation for different pressure variation of 100 mbar, 200 mbar, 400 mbar when a sinusoidal wave is applied for a square shape resistance.

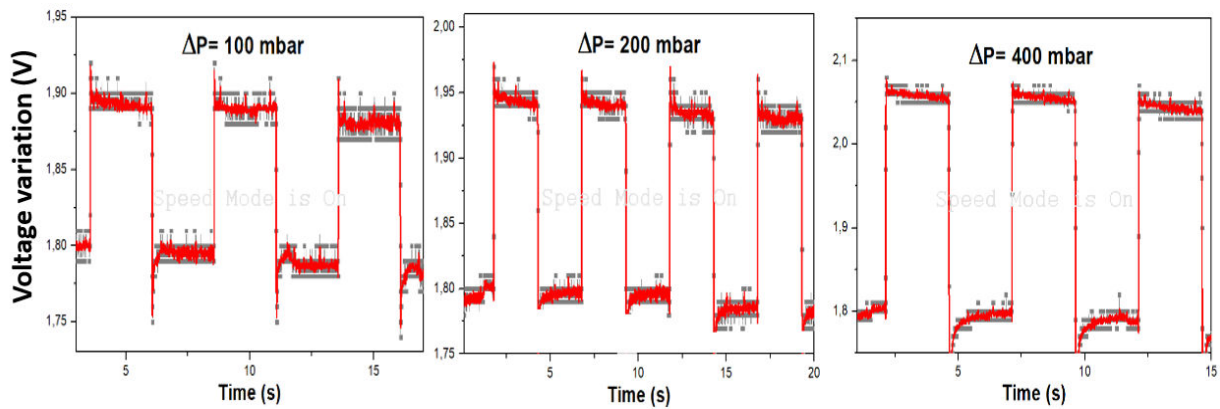


Figure 4.39 (b). Voltage variation for different pressure variation of 100 mbar, 200 mbar, 400 mbar when a square wave is applied for a square shape resistance.

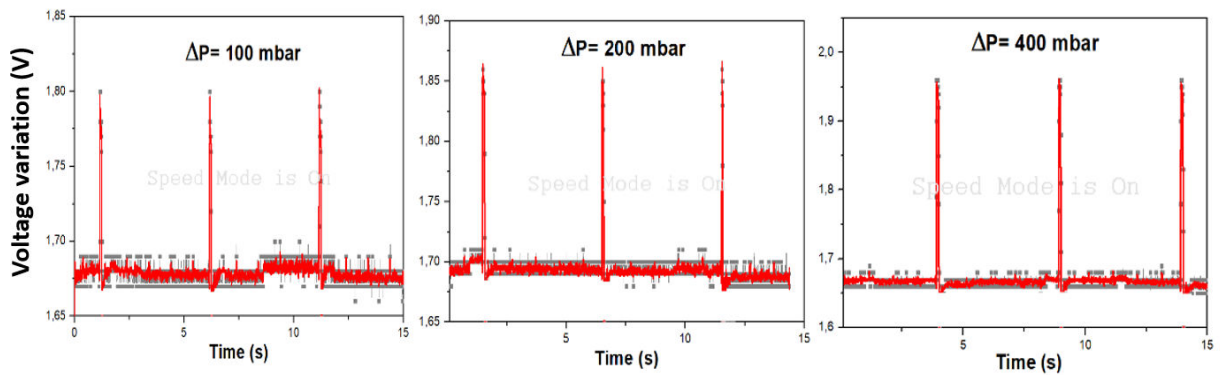
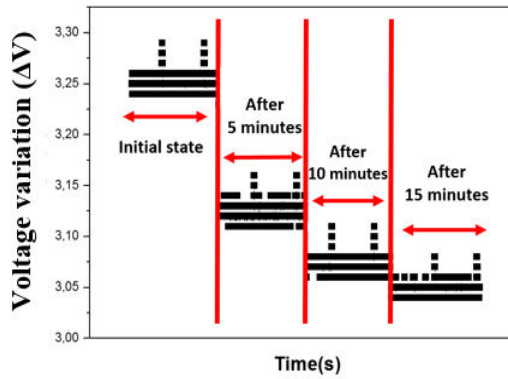
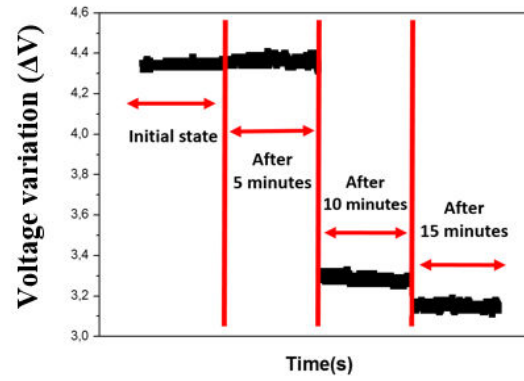


Figure 4.39 (c). Voltage variation for different pressure variation of 100 mbar, 200 mbar, 400 mbar when a pulse wave is applied for a square shape resistance.

g) Figure 4.40 Loading-offloading cycles test

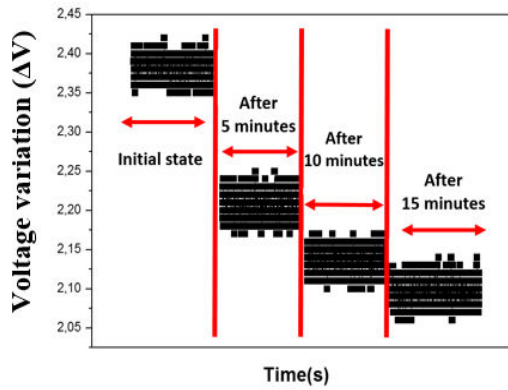


a)

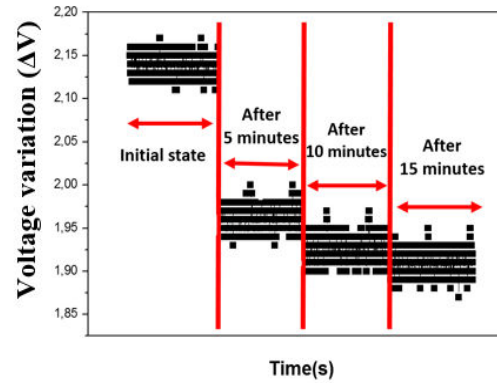


Rosette shape

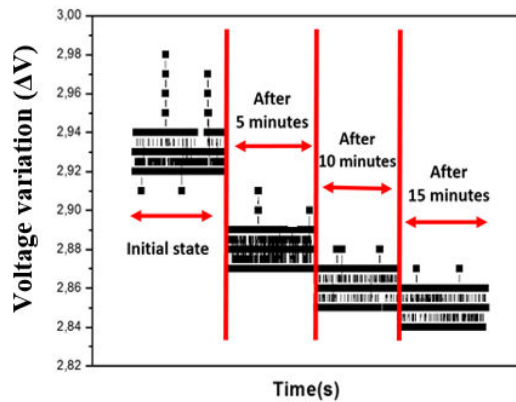
b) U-shape



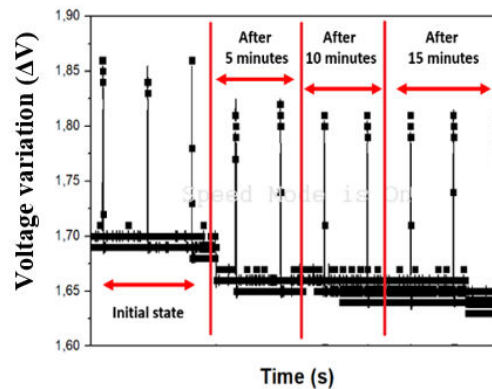
c) Simple serpentine shape



d) Serpentine shape in parallel



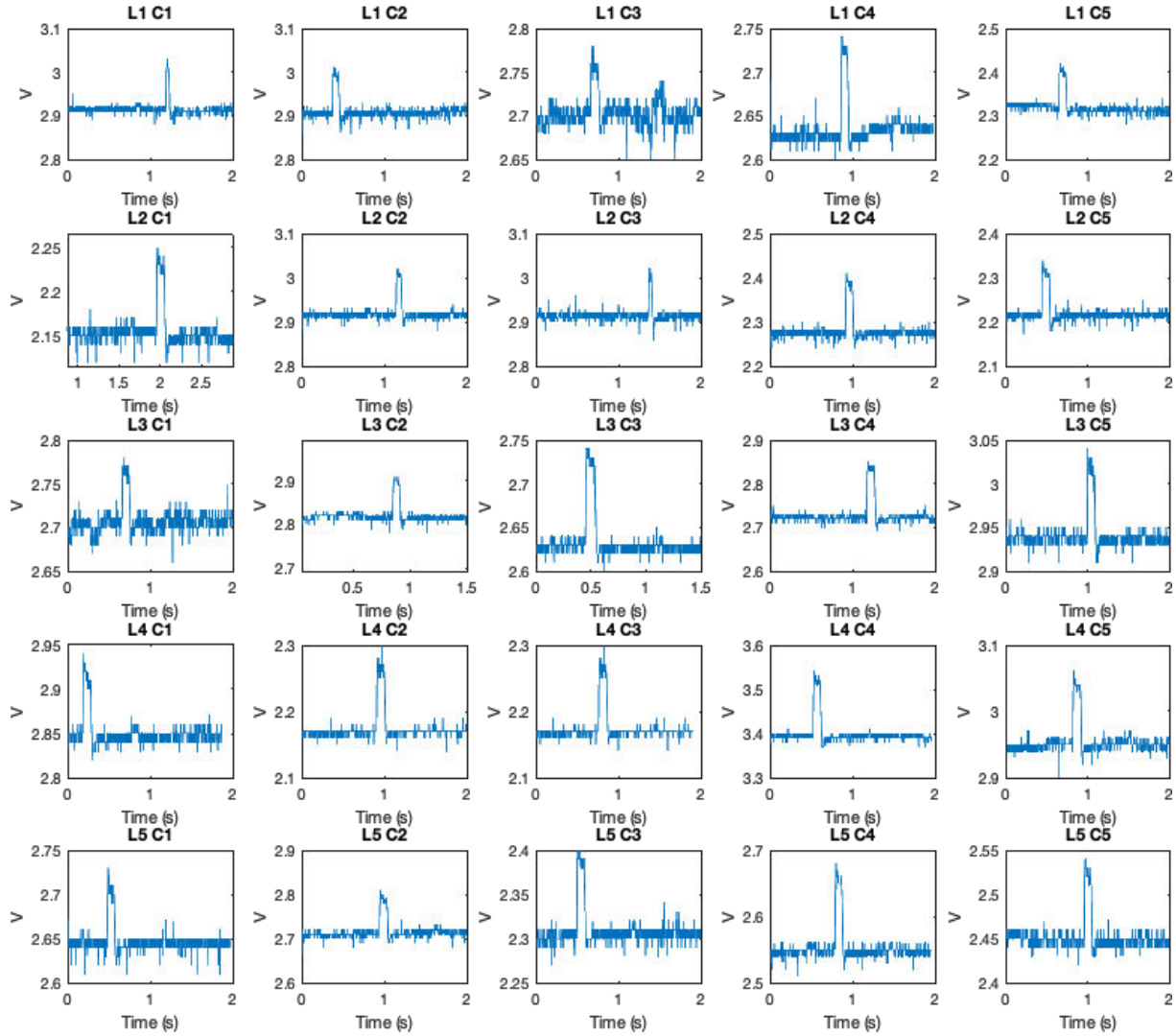
e) Five parallel resistances



f) Square shape

Figure 4.40. Loading –offloading test realized during 15 minutes for the different structures shapes.

h) Figure 4.45 Mapping waveform of the matrix



Mapping waveform of the matrix when it is submitted to a pulse wave of 200mbar of pressure variation using pulses frequency of 0.2Hz

11. References

- [1] Datasheet ‘OB1 - 4 channels microfluidic flow controller’, *Elveflow*.
- [2] Architecture of Arduino development board. <http://www.arduino.cc/>
- [3] ‘Know all about Analog to Digital ADC Converters’.<https://www.elprocus.com/analog-to-digital-adc-converter/>.
- [4] ‘MyoWare™ | Harness the power of your muscle signals!’, *Kickstarter*.
<https://www.kickstarter.com/projects/312488939/myowaretm-harness-the-power-of-your-muscle-signals>.
- [5] Datasheet ADS126x32-Bit, Precision,38-kSPS, Analog-to-DigitalConverter (ADC) with Programmable Gain Amplifier (PGA) and Voltage Reference
- [6] ‘Resistance and Resistivity | Physics’.<https://courses.lumenlearning.com/physics/chapter/20-3-resistance-and-resistivity/>.
- [7] K. Lloyd, ‘Strain Gauge Measurement using Signal Generator | Strain Gauge Sensitivity’, *MTI Instruments*.
- [8] Y. Chan, M. Skreta, H. McPhee, S. Saha, R. Deus, and L. Soleymani, ‘Solution-processed wrinkled electrodes enable the development of stretchable electrochemical biosensors’, *Analyst*, vol. 144, no. 1, pp. 172–179, 2018.
- [9] N. Liu, A. Chortos, T. Lei, L. Jin, T.R. Kim, W-G. Bae, C. Zhu, S. Wang, R. Pfattner, X.Chen, R.Sinclair, Z. Bao ‘Ultratransparent and stretchable graphene electrodes’, *Sci. Adv.*, vol. 3, no. 9, p. e1700159, pp. 1-10, 2017.
- [10] J. Lee, S. Kim, J. Lee, D. Yang, B. C. Park, S. Ryu, I. Park, ‘A stretchable strain sensor based on a metal nanoparticle thin film for human motion detection’, *Nanoscale*, vol. 6, no. 20, pp. 11932–11939, 2014.
- [11] J. Sheng, H-J. Jeong, K. Han, T. Hong, J. Park ‘Review of recent advances in flexible oxide semiconductor thin-film transistors: Journal of Information Display: Vol 18, No 4, pp. 159-172, 2017 <https://www.tandfonline.com/doi/full/10.1080/15980316.2017.1385544>.
- [12] ‘Dewesoft Training Portal - Strain measurement’.
<https://training.dewesoft.com/online/course/strain-measurement>.
- [13] M. Amjadi, K.-U. Kyung, I. Park, and M. Sitti, ‘Stretchable, Skin-Mountable, and Wearable Strain Sensors and Their Potential Applications: A Review’, *Adv. Funct. Mater.*, vol. 26, no. 11, pp. 1678–1698, 2016.

General conclusion and perspective

The objective of this thesis is to investigate the piezoresistivity properties of $\mu\text{c-Si}$ to develop a sensor able to react to continuous and dynamic deformations with good linearity, fast and with reproducible results.

To do that, the sensors are fabricated on $25\mu\text{m}$ of Kapton® substrate. This material is biocompatible and it can withstand chemical solutions. This makes it one of the most frequently used substrates for standard micro-manufacturing process. Although it can support high-temperature conditions, until $400\text{ }^{\circ}\text{C}$, the maximum temperature chosen during this fabrication process was an annealing at $180\text{ }^{\circ}\text{C}$, making the process compatible with other kinds of plastic substrates.

As a semiconductor material, $\mu\text{c-Si}$, deposited by two different techniques PECVD and ICP-CVD, is selected. The motivation to use this material is its compatibility with flexible substrates, moreover, it was widely investigated at the IETR however never as a pressure sensor for dynamic measurements.

We want to create sensors thinner as possible, to improve their flexibility and mechanical behaviour under dynamic deformations. To achieve it, the substrate thickness is reduced. However, this fact leads to increase the misalignment on the layers during the fabrication process and arises stress problems on the structure. To reduce this effect, Kapton® substrate is pre-baked after cleaning process for 30 min at $150\text{ }^{\circ}\text{C}$ and $\mu\text{c-Si}$ is deposited through a shadow mask.

The thesis is mainly divided in two parts, the first one where the piezoresistive properties of $\mu\text{c-Si}$ is investigated through static deformations and for the second part, this material is submitted to dynamic deformations. To investigate the piezoresistive properties of $\mu\text{c-Si}$ under static deformations. This material was deposited by two different techniques, PECVD and ICP-CVD.

$\mu\text{c-Si}$ deposited by PECVD has previously been investigated during K. Kandoussi's thesis and the deposition parameters have been optimized along it. For this reason, here it is studied if the reduction of the thickness in the structure affects $\mu\text{c-Si}$ sensitivity. The results obtained show that when the global structure is reduced, the resistivity uniformity of $\mu\text{c-Si}$ gets worse and its standard deviation is higher. However, it does not have influence on the sensitivity of the material, GF (gauge factor) that is practically the same for the three proposed structures, $\text{GF} = -$

25. This is interesting because the thickness reduction will improve the flexibility of the structure film/substrate when it will be subjected to dynamic measurement.

On the other hand, ICP-CVD technique is new in the laboratory for that reason it was necessary to investigate which conditions are the most appropriated for the targeted application. To do that, it was proposed ten different conditions based on the variation of some key parameters such as: i) The nature of the dopant gas (AsH_3 or PH_3) and its concentration. ii) The effect of the apply RF bias using a constant power value or varying the power by pulsing of 400 ms every 4 s. iii) The effect of LF or ICP power applying it in a continuous mode at 600W or in small pulses between 600W-900W for 400 ms every 4 s. The most interesting results can be summed up in the points below, such as:

- RF pulse adjunction leads to increase the crystalline fraction compared to that obtained for deposits elaborated with continuous bias. However, it also affects the layer stress which could induce sticking issues on Kapton®.
- Under the same deposition conditions, films doped with PH_3 present a higher crystallinity and a lower resistivity than those obtained with AsH_3 . However, the samples deposited with PH_3 , present lower linearity during the static measurements.
- For AsH_3 an increment in the sensitivity (GF) is produced when RF power is applying by small pulses. However, for PH_3 , this only occurs when it is addition pulses to ICP-CVD power because this creates high energy in the plasma that affects the dissociation of the molecules.

To fabricate the sensors that will be submitted to dynamic deformations, it was decided to select ICP-CVD as deposition technology. PH_3 was selected as doping gas because it offers a compromise between crystallinity and resistivity. To obtain a low standard deviation in the deformations, the plasma is created without applying pulses on RF power. Moreover, for this condition (sample 1) the value of the sensitivity for GF= -33 is higher than the value obtained with PECVD, GF= -25.

The second part is concentrated on the mechanical and electrical behaviour of $\mu\text{c-Si}$ under dynamic deformations.

First, it was necessary to create our own home-made acquisition system to perform dynamic measurements. After that, different structures and designs were studied to try to find which one can be more appropriate to the targeted application. Here it was concluded that between all of them, a square shape design with small dimensions is the most robust and will help the global structure to return easily to its initial value.

Moreover, in this part, the mechanical and electrical behaviour of a matrix of 25 resistances was studied. This structure was submitted to different fatigue tests and the results obtained with it present similar values to a square resistance design with the same dimensions. A matrix presents important advantages over the simple structures designs such as its larger integration density in a small area, or the possibility to reduce the fabrication cost and the connections required in this kind of design. These different points make it a good candidate to be used to measure weak and dynamic deformation in a small area.

As a perspective for future work on the topic of this thesis, several points should be explored further, such as:

- Improvement in the characterization system. Due to some limitations in our acquisition system, we could not submit the structures to more rigorous characterization tests, moreover, it is necessary to create an adaptive circuit to characterize the matrix or another kind of technology.
- As it was commented during the manuscript, piezoresistive sensors, as in comparison to other technology, require a less complex data acquisition system, and that moreover, they are less sensitive to electromagnetic noise however it does not mean that the sensitivity obtains with them is better than with other structures. For that reason it could be interesting investigate the dynamic behaviour of new structures such as thin-film transistors (TFT) or capacitances.
- Investigation of the matrix and the different shapes in another kind of substrates. It could be a good option to see their mechanical behaviour in a stretchable substrate or transfer the structure to one biocompatible with the skin to use the devices to monitoring real physiological signals.

Moreover the ability of this technology to detect complex waveforms deformation and reproduce it, opens a large possibility of applications where it can be used such as the blood pressure measurement, reproduces the vibration of the vocal cords, e-skin technology or touch screen are some of them.

Thèse de l'Université de Rennes 1

Microcapteurs de déformation sur substrat souple pour des applications en santé

Deformation microsensors on flexible substrate for health applications

Présentée par **Fatima GARCIA CASTRO**

Résumé

Les nouvelles exigences de la société ont stimulé le marché de l'électronique, en particulier celui de l'électronique flexible. Cette technologie change les usages car elle offre la possibilité de fabriquer des dispositifs capables de s'adapter à n'importe quelle surface, pouvant être pliés, déformés ou étirés. Ces technologies trouvent des applications directes dans différents secteurs tels que l'automobile, les biocapteurs, la santé, les appareils mobiles ou la technologie portable et suscitent un intérêt croissant. Bien qu'ils aient fait l'objet de nombreuses recherches, les dispositifs flexibles ont de nombreuses applications potentielles et leurs performances sont encore à améliorer.

Ce travail de recherche porte sur la fabrication de microcapteurs de déformation sur substrat souple (Kapton). Les dispositifs sont élaborés et optimisés dans l'objectif de détecter de faibles déformations en temps réel. Ils peuvent trouver des applications en santé en particulier via l'acquisition de faibles signaux électrophysiologiques pouvant être détectés par une déformation, par exemple à la surface de la peau (mesure de pouls, contractions musculaires, déformations sous contraintes ...). Ce sujet s'appuie sur les compétences développées au département Microélectronique et Microcapteurs de l'IETR en fabrication de capteurs mais a nécessité un véritable développement technologique novateur, en particulier pour adapter la technologie utilisée à l'utilisation de substrats souples de très faible épaisseur, incluant des études de contraintes mécaniques et de stress dans les matériaux. C'est donc un travail complet comprenant du design de capteur, de l'optimisation technologique, du test et une

caractérisation exhaustive des capteurs, en particulier avec le développement d'un banc de test spécifique pour les mesures reproductibles de déformation en temps réel.

Le premier chapitre présente un aperçu général de l'état de l'art des capteurs de pression avec les mécanismes de transduction les plus populaires, en particulier la piézorésistivité. Les technologies actuelles de fabrication pour l'électronique flexible sont présentées, ainsi que les différents matériaux compatibles avec la fabrication d'électronique flexible, du substrat aux électrodes.

Ce travail a nécessité la mise au point d'un procédé de fabrication compatible avec les propriétés chimiques et thermiques des substrats, tout en permettant une fabrication économique sur de grandes surfaces. La diminution de l'épaisseur du substrat qui doit permettre une meilleure conformabilité du capteur, induit des contraintes supplémentaires, liées en partie aux propriétés mécaniques des matériaux utilisés. Le principal matériau utilisé pour la détection, via l'effet piézorésistif, est le silicium microcristallin ($\mu\text{c-Si}$), dont les procédés de dépôts, utilisant deux techniques différentes (PECVD et ICP-CVD), sont compatibles avec ce type de substrat. La température maximale utilisée lors du procédé de fabrication a été limitée à 180°C . Une partie du travail a consisté à étudier différentes possibilités technologiques, à la fois sur les caractéristiques des matériaux et sur les procédés, permettant la mise au point d'un procédé de fabrication reproductible, suffisamment robuste, tout en diminuant les contraintes pouvant détériorer les propriétés des capteurs. Les stress engendrés par les matériaux, provoquant des défauts dans les couches, ont été réduits par différentes techniques. La figure ci-dessous montre l'évolution du stress sur un Kapton de $25\ \mu\text{m}$ d'épaisseur.



Figure 1 : Réduction du stress d'un film Kapton / $\mu\text{C-Si}$ par modification technologique (traitement initial du substrat, dépôt localisé de matériau).

Différentes association de matériaux ont également été testées. Une approche théorique, développée en parallèle, en prenant en compte en particulier des propriétés mécaniques des différentes couches, permettent d'expliquer et de commenter les résultats obtenus.

Après avoir étudié ces paramètres technologiques ainsi que les différentes approches utilisées tout au long du processus de fabrication développé au cours de cette thèse, l'objectif a été d'étudier les propriétés piézorésistives du silicium microcristallin via la mesure de sa sensibilité aux différentes déformations mécaniques.

Dans un premier temps, la méthode utilisée s'est basée sur le principe des mesures de lignes de transmission (TLM). Dans cette section, les paramètres extraits avec cette méthode sont théoriquement expliqués avec une attention particulière sur la résistivité spécifique du contact. Ce paramètre est devenu très important en raison de la forte réduction de la taille des dispositifs, pour lesquels la valeur des résistances parasites doit être très faible.

Le dépôt de $\mu\text{-Si}$ a été effectué en utilisant deux techniques différentes : PECVD (dépôt chimique en phase vapeur par plasma) et ICPCVD (dépôt chimique en phase vapeur par plasma induit par couplage inductif). Pour les deux techniques, les résultats obtenus sont divisés en deux parties. La première consiste à étudier les paramètres classiques de la structure TLM tels que la résistivité spécifique des contacts (ρ_c), la résistance par carré (R_{SH}) ou une cartographie d'uniformité de la résistivité. La deuxième partie présente la sensibilité du silicium microcristallin comme capteur de déformation, lorsque ce matériau est soumis à différents rayons de courbure. Les structures TLM ont été utilisées pour calculer la sensibilité (GF) des jauges de contrainte. Ce facteur de jauge GF, exprimé à l'équation 1, est déterminé à partir de mesures de variation de la résistance électrique du silicium en fonction d'une déformation induite par différents cylindres de différents rayons de courbure.

$$GF = \frac{\frac{\Delta R}{R}}{\frac{\Delta L}{L}} = \frac{\frac{\Delta R}{R}}{\varepsilon} \quad (1)$$

Il a été déterminé pour les couches de silicium microcristallin obtenues avec les différentes techniques ainsi que pour différents paramètres de dépôt.

Les résultats les plus remarquables obtenus avec les deux techniques sont extraits ci-dessous.

A) Capteurs fabriqués selon la technique PECVD

Les conditions utilisées pour déposer du silicium microcristallin sont identiques à celles utilisés lors de la thèse de K. Kandoussi. Par contre, l'effet de la réduction de l'épaisseur du substrat (Kapton de 50 ou 25 μm d'épaisseur) ainsi que l'effet d'une couche supplémentaire de nitrure permettant de compenser le stress global des couches ont été étudiés.

Les valeurs du facteur de jauge obtenus pour l'ensemble de ces structures sont similaires, $GF = -25$, ce qui a permis de montrer que la sensibilité du $\mu\text{c-Si}$ est indépendante de la structure du dispositif.

La Figure 2 montre un exemple d'obtention du facteur de jauge GF .

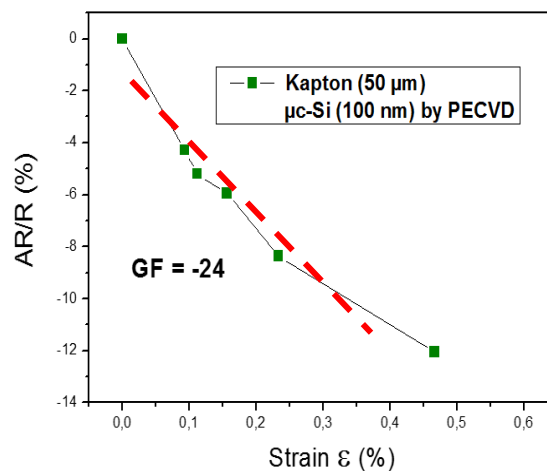


Figure 2. Variation de la résistance en fonction de la déformation et extraction du facteur de jauge correspondant.

B) Capteurs fabriqués selon la technique ICP-CVD

Cette technique étant nouvelle au laboratoire, il a fallu étudier différents paramètres de dépôts, telle que les puissances de plasma ou le niveau de dopage, pour voir leur effet et vérifier leur influence sur la sensibilité du matériau.

Il convient de noter que la sensibilité des capteurs mécaniques obtenus par ICP-CVD est toujours supérieure à celle du PECVD, ($GF > -30$).

Au cours de l'étude des différentes conditions, il a été observé qu'en général, la sensibilité n'est pas affectée par la nature du gaz dopant utilisé lorsqu'il s'agit d'arsine ou de phosphine. Cependant, une augmentation du GF a été observée lorsque la concentration du gaz dopant est réduite.

La dernière partie de cette étude a permis d'étudier l'effet des puissances de plasma utilisées dans le réacteur (RF et LF), que ce soit en mode continu ou de manière pulsée. Il a été observé que les puissances RF avec impulsions n'ont aucun effet, sauf pour un flux élevé d'arsine.

Dans le cas de l'application d'impulsions sur la puissance LF, une amélioration de la sensibilité a été observée, et peut s'expliquer par une plus haute valeur de la fraction cristalline, qui été calculée via des mesures effectuées par spectroscopie Raman.

Pour terminer chapitre, nous avons étudié les propriétés des matériaux piézorésistifs et optimisé la structure du capteur. Il a été décidé d'utiliser la technique ICP-CVD pour fabriquer des capteurs pour la mesure dynamique du chapitre 4. Pour cela, les conditions standard ont été choisies car elles présentent un bon compromis entre la valeur de la sensibilité, $GF = -33$ et la haute cristallinité et conductivité. Celles-ci sont indiquées dans le tableau suivant.

Température	Puissance	Pression	Gaz	
T=180 °C	600 W	4 mTor	Ar = 25 sccm	SiH ₄ = 2 sccm
			H ₂ = 25 sccm	PH ₃ = 20 sccm

Tableau 1. Paramètres utilisés pour le dépôt de $\mu\text{-Si}$ par ICP-CVD.

Le chapitre 4 présente l'étude du comportement mécanique du $\mu\text{-Si}$ lorsqu'il est soumis à une déformation dynamique. Nous décrivons ici les étapes suivies pour créer notre propre système de caractérisation, avec différents prototypes pour la simulation de la veine, représentés en partie à la Figure 3.

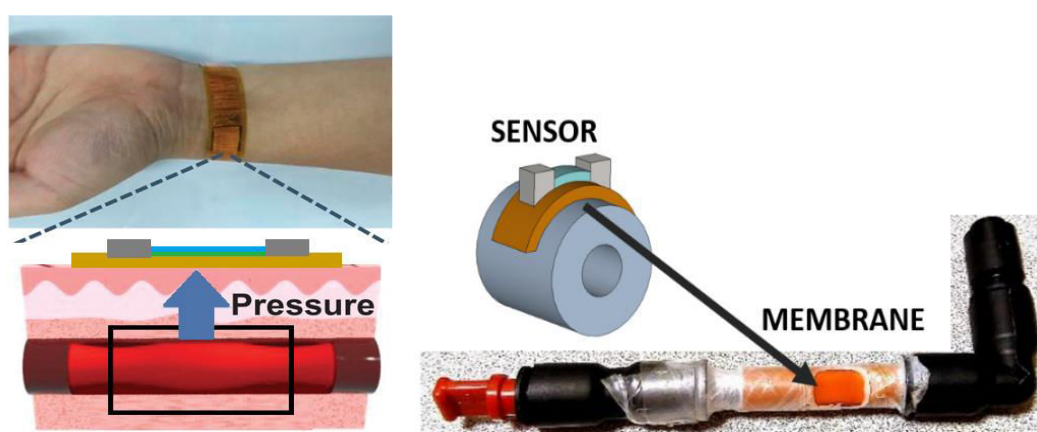


Figure 3. Prototype de simulation de la pression artérielle

L'effet de la conception et de la géométrie sur la performance des capteurs est étudié. Il a été conclu que la conception la plus robuste correspond à la forme carrée de petites dimensions illustrée à la Figure 4. Toutes les conceptions ont été soumises à différents tests tels que des

cycles continus de déformation ainsi que des tests de fatigue et de mémoire. La Figure 5 montre un exemple d'essai de fatigue d'un capteur soumis à une déformation régulière sous forme d'impulsion.

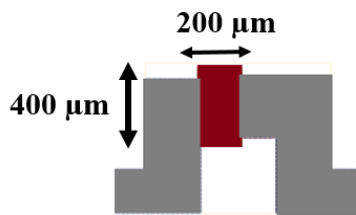


Figure 4. Capteur de forme carrée

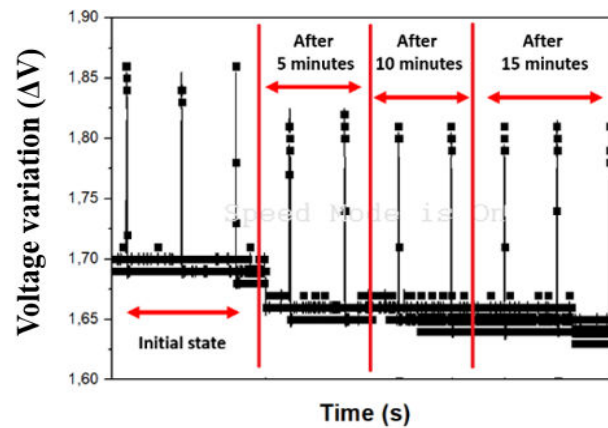


Figure 5. Test de fatigue des capteurs.

Une autre conception intéressante a été la réalisation d'une matrice de 25 capteurs de déformation. Les avantages de cette structure sont nombreux, comme la mesure de la répartition de la pression sur une surface de $1 \times 1 \text{ cm}^2$, une meilleure tolérance pour placer le capteur à l'endroit de la déformation, une plus grande fiabilité par la détermination d'une réponse moyenne des stimuli. En outre, cette structure est capable de réagir à un signal complexe tel que l'ECG ou à des stimuli simples, Figure 6, ayant une amplitude de tension similaire. Les réponses obtenues ont montré une bonne sensibilité, une reproductibilité intéressante et une faible dégradation

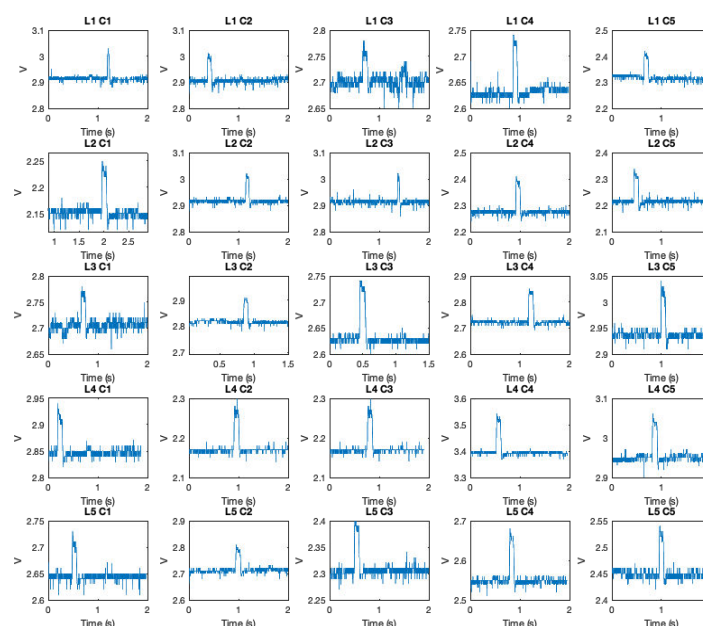


Figure 6. Réaction des 25 capteurs de la matrice à un stimulus

En conclusion générale de cette thèse, différents procédés ont été mis au point sur du Kapton® de 25 μm d'épaisseur et des capteurs ont été développés en utilisant différents matériaux avec différents paramètres et différentes techniques de dépôt. De plus, pour la première fois dans le laboratoire, un système de caractérisation spécifique pour la mesure en dynamique a été créé, impliquant un contrôleur de pression, une membrane déformable et un circuit électronique à connecteur adaptatif. Il a permis d'effectuer des mesures en temps réel à différentes fréquences, pour différentes formes d'onde et valeur de pressions et d'étudier la sensibilité, la fiabilité, le cycle de vie et l'effet mémoire des capteurs.

Enfin, les perspectives sont présentées, et concernent l'amélioration du système de caractérisation et la réalisation de tests de caractérisation plus complets. Le comportement dynamique de nouvelles structures telles que les transistors à couches minces (TFT) ou les capacités pourra également être étudié, ainsi que de nouvelles structures, actuellement réalisées au laboratoire sur différents substrats tels que les substrats extensibles ou hydrosolubles ou biocompatibles pour lesquels le transfert sur une peau pourra être étudié.